FUNCTIONAL CHARACTERIZATION OF GRAPHENE-BASED THIN-FILM MICROELECTRODES ON RAT SENSORIMOTOR CORTEX

by

Fikret Taygun Duvan

B.S., in Mechatronics Engineering, Bahçeşehir University, 2011

M.S., in Biomedical Engineering, University of New South Wales, 2015

Submitted to the Institute of Biomedical Engineering

in partial fulfillment of the requirements

for the degree of

Master of Science

in

Biomedical Engineering

Boğaziçi University

2020

ACKNOWLEDGEMENTS

I would like to acknowledge my appreciation to all who have contributed to this thesis. Foremost, I would like to express my sincere gratitude to my advisor Prof. Burak Güçlü for sharing his knowledge and guidance at all times of my research and during writing of this thesis.

I would also like to thank Prof. Jose Antonio Garrido and Steven Walston for their inputs about the methods and Prof. Ahmet Ademoğlu for his valuable comments.

I would like to thank the members of our lab namely, Sevgi Öztürk, Bige Vardar and Deniz Kılınç for their help during the experiments.

Last but not least, I would like to express my gratitude to my family and close friends for their continuous motivational support.

This work was supported by TÜBİTAK grant no: 117F481 under European Union's FLAG-ERA JTC 2107 project GRAFIN and H2020 Graphene Flagship Core 2.

ACADEMIC ETHICS AND INTEGRITY STATEMENT

I, Fikret Taygun Duvan, hereby certify that I am aware of the Academic Ethics and Integrity Policy issued by the Council of Higher Education (YÖK) and I fully acknowledge all the consequences due to its violation by plagiarism or any other way.

Name :

Signature:

Date:

ABSTRACT

FUNCTIONAL CHARACTERIZATION OF GRAPHENE-BASED THIN-FILM MICROELECTRODES ON RAT SENSORIMOTOR CORTEX

Neuroprostheses based on cortical implants are promising to provide partial sensorimotor function in severe neurological conditions such as spinal cord injuries and amyotrophic lateral sclerosis. One of the key components of these systems is the microelectrode array, which is used for recording brain activity to control a robotic limb and/or for stimulation to induce somatosensory feedback. Graphene is a good candidate as electrode material due to its intrinsic features such as high electrical conductivity and charge injection capacity, high mechanical strength, flexibility and biocompatibility. Evoked local field potentials were recorded epidurally at the hindpaw representation of SI in anesthetized Wistar albino rats. The vibrotactile stimuli were bursts of sinusoidal (5-, 40-, and 250-Hz) displacements (duration: 0.5-s, amplitude range: 19 - 270 μm) applied on the glabrous skin. Performance comparisons were made between matching research grade graphene and commercial Pt-Ir surface electrodes on the same subjects (active site diameter: 25-μm). Robust evoked potentials could be observed shortly after the onset of contralateral stimuli in both electrodes. Pt-Ir electrodes exhibited slightly higher SNR while the lowest impedances were recorded from the channels of the graphene array. Variance of the impedance values were smaller for the channels of the Pt-Ir electrodes. The performance of the graphene electrode channels was observed to be heterogeneous due to ongoing development efforts. This thesis includes one of the first functional tests of graphene electrodes during processing of the natural sensory stimuli in the brain.

Keywords: Primary somatosensory cortex, Cortical recording, Electrical stimulation of the brain, Surface electrodes, Local field potentials

ÖZET

GRAFEN BAZLI İNCE-FİLM MİKROELEKTRODLARIN SIÇAN DUYU-MOTOR KORTEKSİ ÜZERİNDE FONKSİYONEL KARAKTERİZASYONU

Kortikal implantlara dayanan nöroprotezler, omurilik yaralanmaları ve amyotrofik lateral skleroz gibi ciddi nörolojik koşullarda kısmi sensorimotor geri kazanımı fonksiyon sağlayabilmektedir. Bu sistemlerin temel bileşenlerinden biri, bir robotik uzvu kontrol etmek için beyin aktivitesini kaydetmek ve/veya akım enjekte edimi ile somatosensör geri bildirim sağlamak için kullanılan mikroelektrot dizileridir. Grafen, yüksek elektrik iletkenliği ve şarj enjeksiyon kapasitesi, yüksek mekanik mukavemet, esneklik ve biyo-uyumluluk gibi içsel özellikleri nedeniyle elektrot malzemesi olarak iyi bir adaydır. Uyarılmış lokal alan potansiyelleri, anestezi altındaki Wistar albino sıçanlarda birincil somatosensör kortkesin arka uzuv temsilinden epidural olarak kaydedildi. Vibrotaktil uyaran, bir motor tarafından arka uzuv tüysüz derisinee uygulanan sinüzoidal (5-, 40- ve 250-Hz) yer değiştirmeler olarak seçildi (süre: 0.5-s, genlik aralığı: 19- 270 mm). Performans karşılaştırmaları eşleşen grafen ve Pt-Ir yüzey elektrotları arasında gerç ekleştirildi. Her iki elektrotta da kontralateral uyaranların başlamasından kısa bir süre sonra uyarılmış potansiyeller gözlemlendi. Pt-Ir elektrotlar için SNR değerlerinin biraz daha yüksek olduğu görüldü. En düşük empedans değerlerinin ise grafen elektrot kanallarında bulunduğu ancak kanallar arası empedans sapmasının diğer elektroda göre daha yüksek olduğu ortaya konuldu. Grafen elektrot kanallarının performansının, devam eden geliştirme çabaları nedeniyle heterojen olduğu gözlemlendi. Bu tez, doğal duyusal uyaranlara bağlı sinyallerin beyin tarafından işlenmesi sırasında grafen elektrotların ilk fonksiyonel testlerinden birini içerir.

Anahtar Sözcükler: Birincil somatosensör korteks, Kortikal kayıt, Beynin elektriksel stimulasyonu, Yüzey elektrotları

TABLE OF CONTENTS

LIST OF FIGURES

LIST OF TABLES

LIST OF SYMBOLS

$R_{xy}(t)$	Cross-correlation between signals x(t) and y(t)
$A_{peak-to-peak}$	Peak-to-peak amplitude
U_{STD}	Standard deviation
W^f	Wavelet coefficients
$C_{xy}(w)$	Coherence between trace x and y

LIST OF ABBREVIATIONS

BMI	Brain machine interface
CNS	Central nervous system
ANS	Autonomic nervous system
DRG	Dosal root ganglion
SI	Primary somatosensory cortex
MI	Primary motor cortex
SA1	Slowly adapting type 1
SA2	Slowly adapting type 2
RA1	Rapidly adapting type 1
RA2	Rapidly adapting type 2
EEG	Electroencephalography
ECoG	Electrocorticography
LFP	Local field potential
LMP	Local motor potential
EPSP	Excitatory post-synaptic potential
IPSP	Inhibitory post-synaptic potential
ICMS	Intracortical microstimulation
FES	Functional electrical stimulation
SNR	Signal-to-noise ratio
CV	Cyclic Voltammetry
EIS	Electrochemical impedance spectroscopy
CVD	Chemical vapor deposition
AFM	Atomic force microscopy
CNT	Carbon nano-tube
SEP	Somatosensory-evoked potential
LMM	Linear mixed effects model
EMI	Electromagnetic Interference

1. INTRODUCTION

1.1 Motivation and Objectives

Last half century has seen a significant increase in the studies related to the field of neuroengineering. Devices like brain machine interfaces (BMIs), neuroprosthetics and brain stimulators have emerged, all owing to findings of the initial studies aimed at discovering the underlying mechanisms of the nervous system, more specifically the brain. We are still far from having a complete understanding of how this system works but adaptation of the knowledge gathered from the research efforts have resulted in the invention of notable technologies.

At the heart of these technologies, a common component that facilitates communication between electrical circuitry and functioning biological tissue exists. These interfaces that send signals to or collect signals from neuromuscular systems are termed electrodes which are manufactured in various shapes and sizes depending on their intended use. Recordings of the brain signals are an essential component for most of the previously mentioned systems. In addition to recording activity of the brain, electrodes are also used for electrical stimulation. Deep brain stimulators are used for treatment of Parkinson's disease, tremor and depression. Electrical stimulation of the brain is also important for neuroprosthetic applications which makes providing sensory feedback to the user possible. For example, mechanoreceptors of the glabrous skin are mimicked by electrical current injections to the related brain nuclei in order for inducing the sensation of touch.

EEG, ECoG, LFP, single/multi-unit spikes are the generally used methods for collecting signals of the brain which employ scalp, epidural or intracortical electrode designs respectively. LFPs can be recorded either by using intracortical or epidural electrodes which reflect the summation of the synaptic and action potentials of the surrounding neurons under the electrode area. LFPs are employed in different BMI

and neuroprosthetic applications as an input for the mentioned systems. The scale of specificity for recorded activity increases toward the single/multi-unit spikes which come with the cost of invasiveness. Level of invasiveness of the employed method is also very important since electrodes can be rendered useless due to tissue reaction. This is especially important for chronically implanted devices which directly effects their longevity.

Different materials have been used for manufacturing electrodes. Platinum-iridium, titanium nitride, iridium oxide, poly(3,4-ethylenedioxythiophene) polystyrene-sulfonate and carbon nanotubes can be named as a few which exhibit good impedance and charge injection properties for being used as electrode material. Even though the production methods for graphene have not been completely settled for electrode applications, its derivatives were previously studied as an electrode material. Electrochemical characterization of the material revealed its higher charge injection capacity and low impedance characteristics especially in the low frequency range. Nonetheless, the literature regarding graphene's functional performance in neuroscience applications need to be expanded.

Main objective of this study is to assess the performance of graphene based thin-film microelectrodes in comparison to commercially available platinum-iridium microelectrodes. Somatosensory evoked LFPs were recorded from the hindpaw representation of the rat SI cortex and metrics such as voltage RMS, coherence within channels of each electrode and SNR were chosen for extracting comparison data from the recordings. However, only one graphene electrode was used so the results are provisional. The thesis is novel such that surface LFPs were recorded in response to natural vibrotactile stimulation. Therefore, graphene electrodes were functionally tested during sensory processing in the brain.

1.2 Outline

The thesis is presented as follows: In chapter 2, background information about somatosensory system, recording signals from brain, electrical stimulation of the brain, electrodes used in neuroprosthetics, properties of graphene and graphene electrodes are given. Chapter 3 presents the experimental procedures. In chapter 4 results regarding the performance comparisons are given and their interpretations are included in chapter 5.

2. BACKGROUND

2.1 Somatosensory System & Sensation of Touch

In general, sensory information is defined as neural activity arising from stimulation of receptor cells of our body which are sensitive to different types of stimuli. Received sensory input is directed to the responsible central nervous system (CNS) by both serial parallel neural connections. The information becomes more complex as it propagates towards the CNS due to the addition and summation of the neural signal arising from various connections along the route. Recursive circuits originating from higher brain structures that modify the excitability of nerve cells are also involved in the mentioned signal processing effects. Therefore, a percept, the interpretation of the input signals by brain, is formed due to both the internal and environmental influences. Specific receptors of each sensory modality execute a function termed signal transduction where different types of energy are transformed into electrical signals (action potentials), the unified language of the nervous system. Receptors are specialized in transducing specific forms of energy. This property, termed receptor specificity, arises due to the morphological differences of the receptor cells and their selective sensitivity to a certain type of stimulus.

The somatosensory system mediates all the fundamental bodily interactions of a living organism within its own and to its surroundings. In the literature the system is investigated under three distinct parts: proprioception, exteroception and interoception. Proprioception can be defined as an individual's awareness of oneself owing to the posture and movement information sent from the receptors in muscles, joint capsules and the skin. Exteroception is our sense of interaction with the external space and physical forces that acts on us. Sense of touch, thermal sensations and nociception are mechanisms that create a framework for our understanding of the world around us. Interoception is defined as the sense of function of the systems of the body (cardiovascular, respiratory, digestive and renal systems) which are not consciously felt.

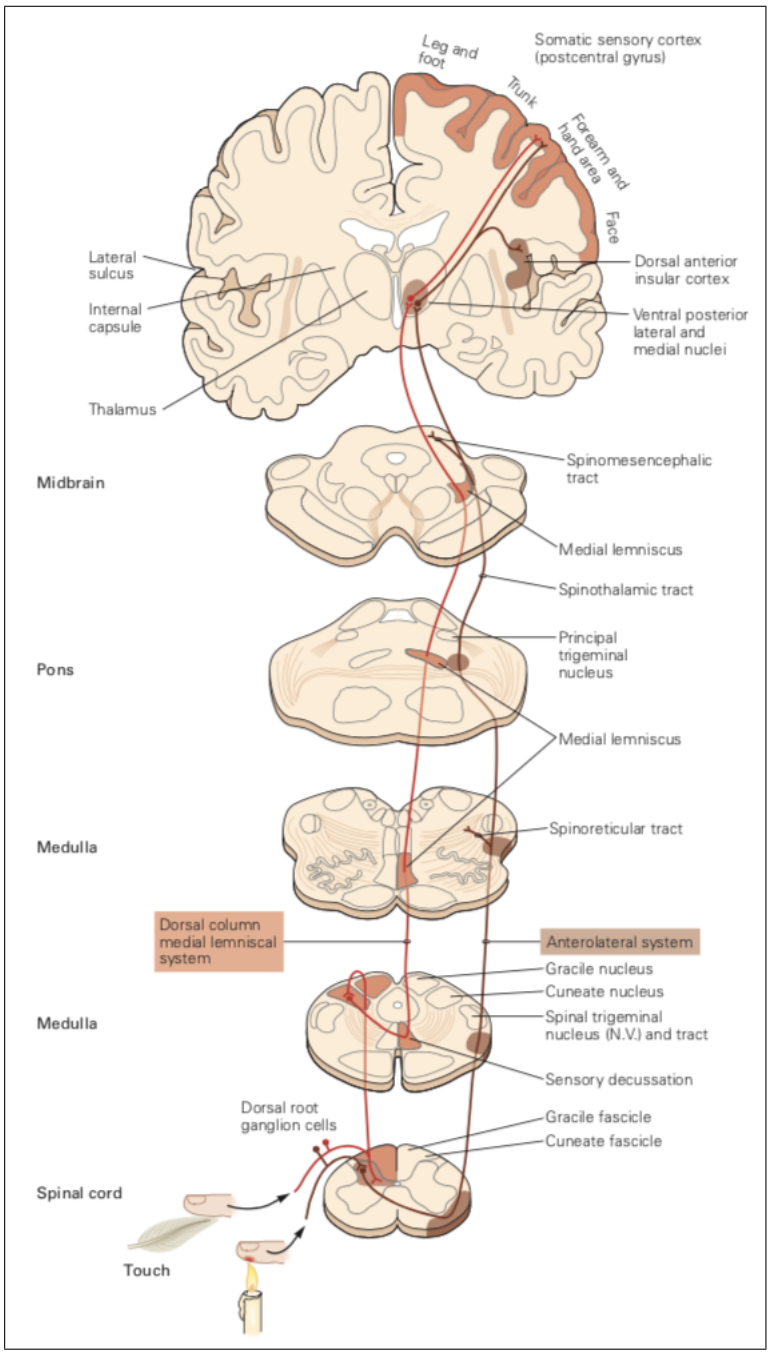

Figure 2.1 Afferent signalling pathway of the somatosensory system is depicted. The primary afferent fibres carry information from several types of cells, including muscle spindles, golgi tendon organs, and joint and cutaneous receptors. Fibres from these cells project to the spinal cord, where they branch to form local and ascending projections onto neurons in the dorsal horn and brainstem, respectively. The incoming somatosensory information undergoes further synaptic processing in the thalamus before arriving in sensory cortex. Somatosensory submodalities from each dermatome are bundled together as they enter the dorsal root ganglia. Separation of these fibres happen when they approach the spinal cord at the exit point of dorsal root ganglia with respect to their diameters and continues through the dorsal column nuclei until they reach the cerebral cortex. Reproduced from [1].

These major organ systems are regulated by the autonomic nervous system (ANS) using the information conveyed by the chemoreceptors that are responsible from monitoring the blood gases and pH levels of the respective organs.

The dorsal root ganglion (DRG) neurons are present at the heart of the somatosensory system that are responsible from conveying information to the CNS from the periphery. The soma of a DRG neuron resides near the dorsal root of the spinal cord and projects one end of its branching axons to the peripheral terminals while the other end meets the CNS (see Figure2.1). The peripheral terminals (receptors) have different morphological characteristics and respond to distinct types of stimuli depending on their location in the body which allow for selectivity between the earlier mentioned types of somatosensation (proprioception, exteroception and interoception). In other words, DRG neurons transduce and encode different types of information (e.g., touch, temperature, pain, visceral states) into electrical signals and relay it to the CNS. During developmental stages the DRG axons are grouped into bundles depending where they innervate on the body thus forming the peripheral nerves. The area of skin and deeper tissue that is innervated by a specific peripheral nerve is called the dermatome. These peripheral nerves eventually project to the primary somatosensory cortex (SI) where cortical representation of each body part reside in a somatotopic arrangement.

Each receptor type of the somatosensory system is innervated by a DRG neuron with differing physical properties such as the axon diameter and myelination which allows for creation of different conduction speeds within the same system. For example, fast conduction speeds are required for sensory feedback in motor control, but nociception requires both slow and fast conducting components. The greatest velocities are observed for the muscle afferent fibres that signify duration of muscle, contraction speed, and energy. The fibres of the peripheral sensory-motor system are functionally grouped into 30 types where 22 of these are afferents carrying sensory information towards the CNS and the remaining 8 are efferent fibres conveying motor commands to the periphery.

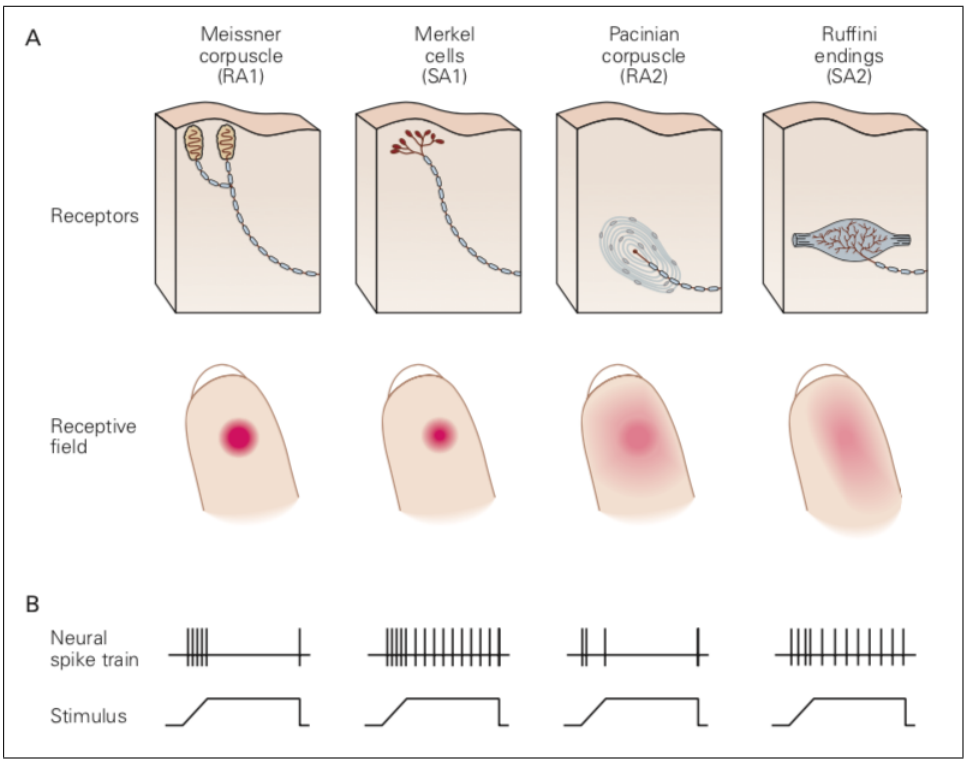

Figure 2.2 Mechanoreceptors of the glabrous skin are shown. Reproduced from [1]. (A) In the top row, positions of the cutaneous receptors within the dermal structure are given. Bottom row illustrate the size of their receptive fields. (B) Spiking behaviour of the receptors in response to a ramp and hold stimulus are shown.

Mechanoreceptors transduce the energy that was transferred to the skin by mechanical perturbations into electrical energy by means of the ion channels that are activated in response to the deflections of the skin. When a channel is activated in response to a suprathreshold stimuli, influx of ions in the extracellular space causes depolarization at the neuron terminal. The generated electrical signal by the receptor cell is named the receptor potential. Eight different types of mechanoreceptors exist in the skin which are responsible from the sensation of touch. In the glabrous skin touch is mediated by 4 of these receptors which are: Meissner corpuscles, Merkel cells, Pacinian corpuscles and Ruffini endings (see Figure 2.2).

Merkel cells are innervated by slowly adapting type 1 (SA1) fibres whose axons are branched into bare nerve plates that are situated on the epidermal-dermal junction. SA1 fibres have small receptive fields therefore their response is highly localized, and they exhibit sustained firing activity while the stimulus is present. SA1s are pre-

dominantly responsive to static skin indentations and low frequency vibrations below 8-Hz [2] and their firing rates are dependent on the velocity and amplitude of the indentation. During object-skin interactions SA1 fibres exhibit selective sensitivity to edges, corners and curved surfaces more than flat surfaces. Merkel cells' sensitivity at frequencies below 4-Hz is found to be better compared to Meissner corpuscles [3].

Ruffini endings which are innervated by slowly adapting type 2 (SA2) fibres and are more sensitive to stretching of the skin. Granted that these cells are situated deeper in the dermis their receptive fields are much larger compared to that of Merkel cells (see Figure 2.2.A). These fibres are responsible from encoding the direction of movement that occurs over the skin as well as providing information about finger positions inferred by the stretching of the skin.

The rapidly adapting type 1 (RA1) fibres innervate Meissner corpuscles which detect pressure related changes on the skin. They are situated inside the dermal layer adjacent to the epidermis in a structure named papillae and have focused receptive fields. In a Meissner corpuscle, nerve endings are arranged in a spring-like structure that are surrounded by a capsule of connective tissue. Deformation of the capsule stimulates the nerve endings which generates an action potential. These receptors fire action potentials only when the stimulus is introduced to or withdrawn from the skin hence marking the start and termination of contact with an object. They fire a few spikes at the onset and offset of a sustained stimulus, and they may entrain with a vibratory stimulus.

Pacinian corpuscles which are innervated by rapidly adapting type 2 (RA2) fibres, exhibit a layered structure similar to that of Schwann cells. Due to this specific arrangement the low frequency vibrations are filtered which makes the corpuscle sensitive to high-frequency vibrations. They are situated in the deeper parts of the dermis similar to the Ruffini endings and have large receptive fields. Pacinian corpuscles are more attuned to high frequency vibrations (100-Hz to 300-Hz) [2, 4] and sinusoidal inputs are shown to generate continuous firing. Owing to their location and high-frequency sensitive behaviour, Pacinian corpuscles signal distant events transmitted

through objects, probes, and hand-held tools.

2.1.1 Rat Primary Somatosensory Cortex

Rats are known to be nocturnal animals who are able to navigate even in complete darkness using the information about its surroundings as perceived by the mystacial vibrissae (whiskers). Displacement of the membrane surrounding these specialized fibres activates the mechanoreceptors in the skin which send signals to the SI via the trigeminal network. As a result of its large dependence on whiskers for object recognition and navigation, the rat SI cortex is dominated by the area receiving input from the mystacial vibrissae. A 1-mm wide region of overlap between the motor cortex and SI which contains the hindpaw and forepaw representations exists. It was shown that, both eliciting limb movements through electrical stimulation and recording somatosensory evoked activity is possible on the mentioned cortical location [5].

Rat SI is investigated under four functionally different parts which are: Par1 (barrel area), FL (forelimb area), HL (hindlimb area) and DZ (dysgranular zone). Par1 accommodates the barrels which represent each vibrissae in rows that copy the arrangement of the vibrissae on the mystacial pads. Brain slice studies revealed that these barrels are formed by collection of granule cells and are separated by perigranular cortex (septa) forming functional columns across different layers of the cortex. Connection between neurons of neighbouring barrels displayed very little connectivity therefore each barrel is treated as an individual network. Spatial cue generation was hypothesized to be realized by the neurons of the perigranular cortex due to their wide interconnectivity [6].

Barrel field of the SI cortex has been extensively studied owing to its importance and magnitude within the rat somatosensory system. Anatomical organization of the mystacial representations were investigated by [7, 8, 9]. Similarly, functional investigations on cortical circuits that carry out sensory processing and efforts for mapping their intracortical and subcortical connections were realized [10, 11, 12]. On the other hand,

studies like [13, 14] delved into behavioural aspects of the system in which rats' dependence on whiskers for navigation was shown in a maze task by clipping the whiskers. Distribution of tactile learning in the barrel cortex was investigated where task trained whiskers or naive whiskers were clipped and prosthetics were attached to their stubs [15]. It was shown that if the prosthetic was attached to the stub of the trained whisker animal was able to use the attachment right away. Also, the transfer of learning from one whisker to the other was shown dependent on the vibrissae topology which was shown by neural recordings from the barrel cortex.

Psychophysics of whisker touch were explored in [16] by performing single-unit recordings on the barrel cortex during texture discrimination. Interestingly, the analysis revealed neither the firing rates nor the temporal discharge patterns were significantly different when compared for rough versus smooth surfaces which was attributed to the possibility of coding of these different features might have been done by populations of neurons therefore observing difference in single-unit data was not possible. Correlation between neural response function of cortical neurons and behaviour of the rats were reported in sensory detection and discrimination tasks by [17]. The authors employed series of sinusoidal whisker vibrations delivered through a plastic micropipette by varying the stimulus intensity (product of frequency and amplitude). Additionally, many other studies [18, 19, 20, 21] employed whisker stimulation for investigating various phenomena.

On the contrary, literature regarding the limb representations of rat SI cortex which receives input from the glabrous skin are sparse. Receptive field of the forelimb neurons were examined by stimulating the dorsal and ventral sides on the subjects' forepaw using a metal probe that was actuated a piezoelectrical circuit [22]. In a follow-up study [23], authors examined the cortical representations of contralateral versus ipsilateral stimulation of the limbs. It was reported that a large cortical overlap among paw representations exist where only 23% of the responsive neurons (47 of 204) responded exclusively to one paw, whereas 52% (107 of 204) responded to two paws, 19% (39 of 204) responded to three paws, and 5% (11 of 204) responded to all four paws. They mentioned that the magnitude of ipsilateral response for both cases (hindpaw

and forepaw stimulation) was found to be smaller compared to that of contralateral response and the latency for ipsilateral response was significantly higher. Furthermore, ipsilateral latency variability was larger which was attributed to multiple pathways that the somatosensory input could be using to reach the ipsilateral cortex: below the level of thalamus, thalamocortical level, cortical level through corpus callosum, from secondary somatosensory cortex or directly opposite primary somatosensory cortex. Finally, it was deduced that extent of cortical overlap between hindpaw and forepaw representations reaches the maximum extent in awake conditions.

In a recent study [24] frequency dependent effects of vibrotactile hindpaw stimulation on the responses of SI cortical nuerons were investigated. The excitation and inhibition dynamics in the cortex were examined by NMDA receptor inhibition with ketamine and by microinjections of bicuculine, a $GABA_A$ antagonist, and AMPA, in order for modelling the mechanoreceptive inputs from the rat glabrous skin.

2.2 Recording Electrical Activity of the Brain

The electrical signaling mechanism of the brain was first shown by Hans Berger in 1929 [25] where he used electroencephalography (EEG) recordings and successfully described the alpha and beta waves of the brain -distinguished by wave frequencies- that are induced by eyes closed and opened states in awake human subjects. In addition to EEG, electrocorticography (ECoG) and recording from individual and multiple neurons were widely studied. Figure 2.3.a illustrates the difference between the EEG, ECoG, local field, single- and multi-unit activity methods which arise due to their respective recording locations. Spatial information content of the signal increases as the modality becomes more invasive at the expense of inducing greater tissue reaction in the parenchyma. Figure 2.3.b shows the physical range of the recorded signals with the respective modalities where the signal content experiences a change from a very local to global scale.

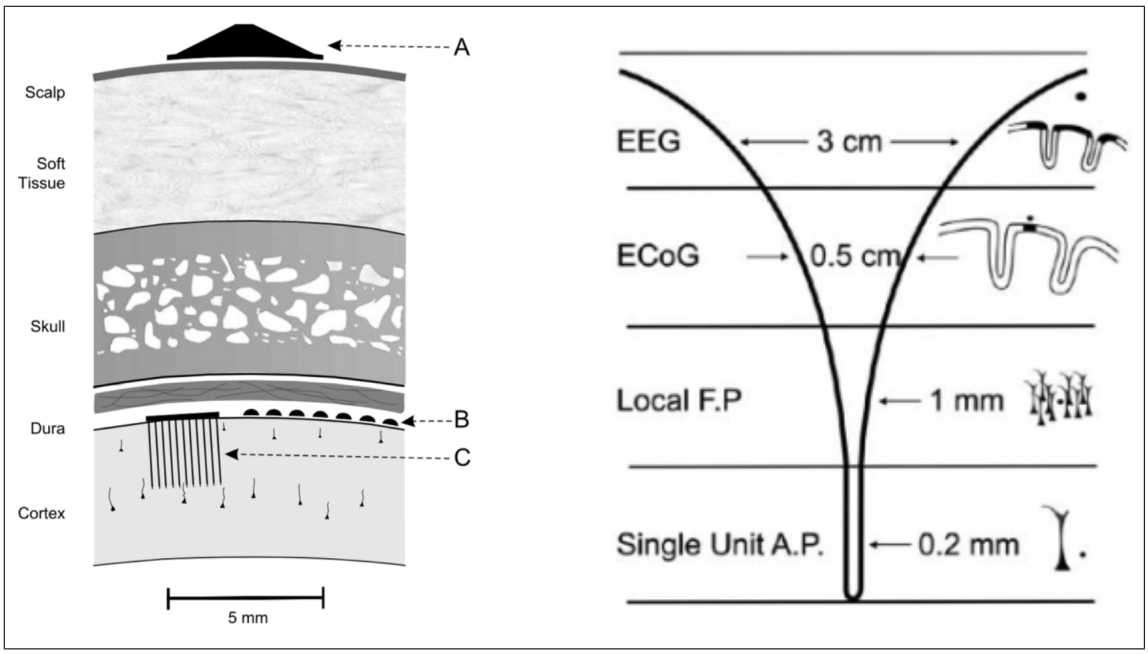

Figure 2.3 Different modalities for measuring electrical activity of the brain is depicted. (a) Shows the different target locations for EEG (A), ECoG (B) and single/mutli-unit (C) recordings. Replicated from [26] (b) Illustrates the locus of recorded activity for each recording modality. Reproduced from [27].

Large scale brain signals (for example EEG, ECoG) are commonly divided into the following subcategories with respect to frequency bands: delta (<4 Hz), theta (4- to 8-Hz), alpha (8- to 12-Hz), beta (12- to 30-Hz), gamma (30- to 80-Hz) and high gamma (80- to 150-Hz). The nomenclature is not very definite since the band limits can have little variation from study to study. Certain associations between behavioural states and frequency intervals has been studied in the literature. The gamma band power has shown to increase during a variety of cognitive tasks, whereas alpha rhythm correlation to sensory disengagement has been discussed [28].

2.2.1 EEG

EEG serves as the most frequently used tool in monitoring brain activity both for clinical and research purposes. The predominant advantage of EEG is that its recording procedure is completely non-invasive, where electrodes are placed directly over the scalp, allowing for easier operation. EEG measured from the scalp captures

the activity of a large population of neurons that are synchronously activated. Due to the orientation of the pyramidal cells -which comprise 70-90% of all neurons in the cortex [29]- the dipoles are generated perpendicular to the scalp. Therefore, potentials from the gyral tissue are more prominently observed in the EEG. Spiking neurons are modelled as current dipoles due to the charge dynamics created by the input received at the post-synaptic terminals which creates a current flow near the neuron where one end acts as a source and the other as a sink.

Apart from its clinical use as a diagnosis tool for conditions like epilepsy, sleeping disorders, EEG has found application in BMIs. Controlling a BMI with EEG is realized by identifying different activity patterns from the extracted signal by employing either regression or classification algorithms. Different components of EEG such as the signal amplitude, power spectral densities, time-frequency features and autoregressive parameters were employed as features for extraction. Temporal dynamics of the EEG signal, by recording the P300 wave which is a distinct event-related potential observed during decision making, is exploited using the oddball paradigm [30]. The method is employed with different stimulation modes by utilizing auditory or visual cues for control of BMIs. The P300 speller is a widely studied device which helps locked in patients communicate with the outside world [31, 32, 33, 34, 35].

Another approach for BMI control with EEG takes advantage of the frequency properties of the recorded signal. In an EEG-based discrimination study, Pfurtscheller and colleagues [36] asked subjects to imagine as if they were moving their right or left hand while their EEG data was being collected. The EEG signal was used to predict the subjects' preference with the help of a neural network classifier that was created during the training sessions for each of the subjects separately. Three subjects were involved in the experiments and for each subject different frequency bands which varied between 9- to 14-Hz and 18- to 26-Hz provided the best discrimination performance. In another study [37], an EEG-based controller for use with a prosthetic hand was developed. Subjects were trained for controlling the amplitude of the 18- to 40-Hz (beta-band) component of the EEG and the interpreted signal was used for controlling the grasping motion on a prosthetic hand.

The advantage of easier operation of EEG comes with the loss of signal content both in the time and frequency domain. The structures between the targeted neurons and the electrode induces capacitive effects which attenuates the high frequency components of the signal and the diminishing amplitude with the distance. Typical human EEG signal amplitude is about 10- to 100- μV [38] and the frequently used frequency bands for BMI operation are the alpha and beta frequency bands although the frequency content of an individual neuron spiking is between 100-Hz to 10-kHz.

2.2.2 ECoG

Discovery of the ECoG method was realized by two neurologists Wilder Penfield and Herbert Jasper which originated from the need for detecting the epileptogenic zones in patients with severe epilepsy [39]. Instead of recording electrical potentials from the scalp, ECoGs are recorded directly by placing the electrodes over the cortex. Recording ECoG signals require surgical removal of a portion of the skull (craniotomy) for exposing the cortex. On the other hand, brain parenchyma is not harmed during the procedure which makes it a less invasive procedure compared to intracortical recording. ECoG yields finer spatial resolution and is less prone to filtering effects which helps preserving more of the frequency content of the signal compared to EEG.

Clinically, ECoGs are mainly used in epilepsy surgeries for identifying the epileptic activity zones for resection (pre-surgery) and confirming the success of operation by assessing the existence of any remaining epileptiform activity (during surgery). Possibility of using ECoGs in BMI applications were explored by collecting data from patients who are implanted with the ECoG electrodes for determining the epileptic activity zones [40, 41, 42]. In their study [41] authors investigated the possibility of controlling a computer cursor in a single dimension by using sensorimotor cortex ECoGs from human subjects. They reported decreased mu and beta and increased gamma (40- to 180-Hz) band activity and the activation was independent of the imagined or actuated action (e.g. saying the word "move" and imagining saying the word "move"). Furthermore, recorded data from patients when they were moving the cursor

with a joystick revealed high correlations between the movement direction and gamma band activity. Finally, it was deduced that ECoGs allow a faster learning curve in the subject and are more effective.

2.2.3 Local Field Potentials

The synchronized neural activity arising from a population of surrounding neurons are termed as local field potentials (LFPs). Although the literature contains different descriptions for the frequency range of the LPFs, it can be generalized as the low-frequency activity (<500-Hz) of the cortex. LFPs represent the slow neural events generated by the current and sink dynamics of the previously mentioned dipole mechanism and can be recorded by either intracortical or subdural electrodes. They are less sensitive to the physical variation of the recording site; for example, cell death or movement of the electrodes as a consequence of being the summed activity of multiple sources. LFP contribution for cells that exhibit open field geometry, such as pyramidal cells, are greater than that of the cells with closed field arrangement. In the former case the dendrites are distributed in parallel to each other which creates an ideal geometry for formation of strong dipoles whereas in the latter radially distributed dendrites cause cancellation effects. Recent studies showed that generation of the current dipoles are not only dependent on the excitatory post-synaptic potentials (EPSPs) but also factors such as inhibitory post-synaptic potentials (IPSPs), subthreshold membrane oscillations and spike afterpotentials generated by Ca+ activated K currents are responsible mechanisms [43, 44, 45]. It was suggested that synchrony of firing between individual neurons has a crucial effect on the magnitude and spread of the field potentials. Although the theoretical basis of how the field potentials are generated is well-known, pinpointing their topological source is a challenging task due to the highly irregular neuron geometry and their distribution within the brain.

Many studies showed that LFPs exhibit differential power densities with respect to frequency. In a memory-saccade study on macaque monkeys (n=2) where LFP and spike data were collected from different populations of neurons, authors reported

elevated power in gamma band (25- to 90-Hz) and correlated spiking activity [46]. LFP power spectrum from the recordings of monkey primary visual cortex were extracted by [47]. The study concluded that power increase was observed for frequencies above 80-Hz and correlation between increased power and spike rates were observed. A visual attention study on macaque monkeys reported increased gamma (35- to 90-Hz) power only when the subject is attending the visual stimulus [48]. Belitski and colleagues [49] recorded LFPs and spike trains from the visual cortex of anesthetized rhesus monkeys (n=4) in response to a color movie. Authors stated that two frequency bands (1- to 8-Hz) and (60- to 100-Hz) within LFPs carry the most information related to stimulus. Single-unit and LFP activity were recorded from the somatosensory cortex of awake macaque monkeys (n=2) in response to vibrotactile stimulation targeting the digits with three different stimulation frequencies (50-, 100- and 200-Hz) [50]. The study showed that firing rate and high-gamma (≈60- to 200-Hz) power is strongly correlated.

Information content of the LFPs were studied by [51]. It was hypothesized that neurons encode information not only through their spike counts but also the spike times relative to the phase of ongoing network fluctuations contain information. Primary visual cortex of the anaesthetized macaques was targeted for recording local field potentials (LFP) and Multiunit spike recordings (MUA) while they were shown a colour movie. Using Hilbert Transform the phase of the LFP fluctuations were examined and for the 1- to 4-Hz frequency band it was shown that the probability of observing a spike during the preferred phase ($3\pi/2$ rad) was twice the probability of observing a spike during the anti-preferred phase ($\pi/2$ rad). Figure 2.4.a illustrates the 1- to 250-Hz oscillations that are present in the recordings in which Figure 2.4.b represents a narrower window of 1- to 4-Hz (delta band) with colour coding denoting the phase of the wave. The resulting time course of the phases of delta oscillations in response to the repeated presentation (30 times) of the movie stimulus is given in Figure 2.4.c following the same colour coding scheme. The striking correspondence between spike times and the phases of delta band oscillations become immediately apparent when the data given in Figure 2.4.d and .e are examined. The green star and the blue circle given in Figure 2.4.f denotes two peaks in which the spike rates are equal but have different phase values. Discriminating these two points from each other to understand

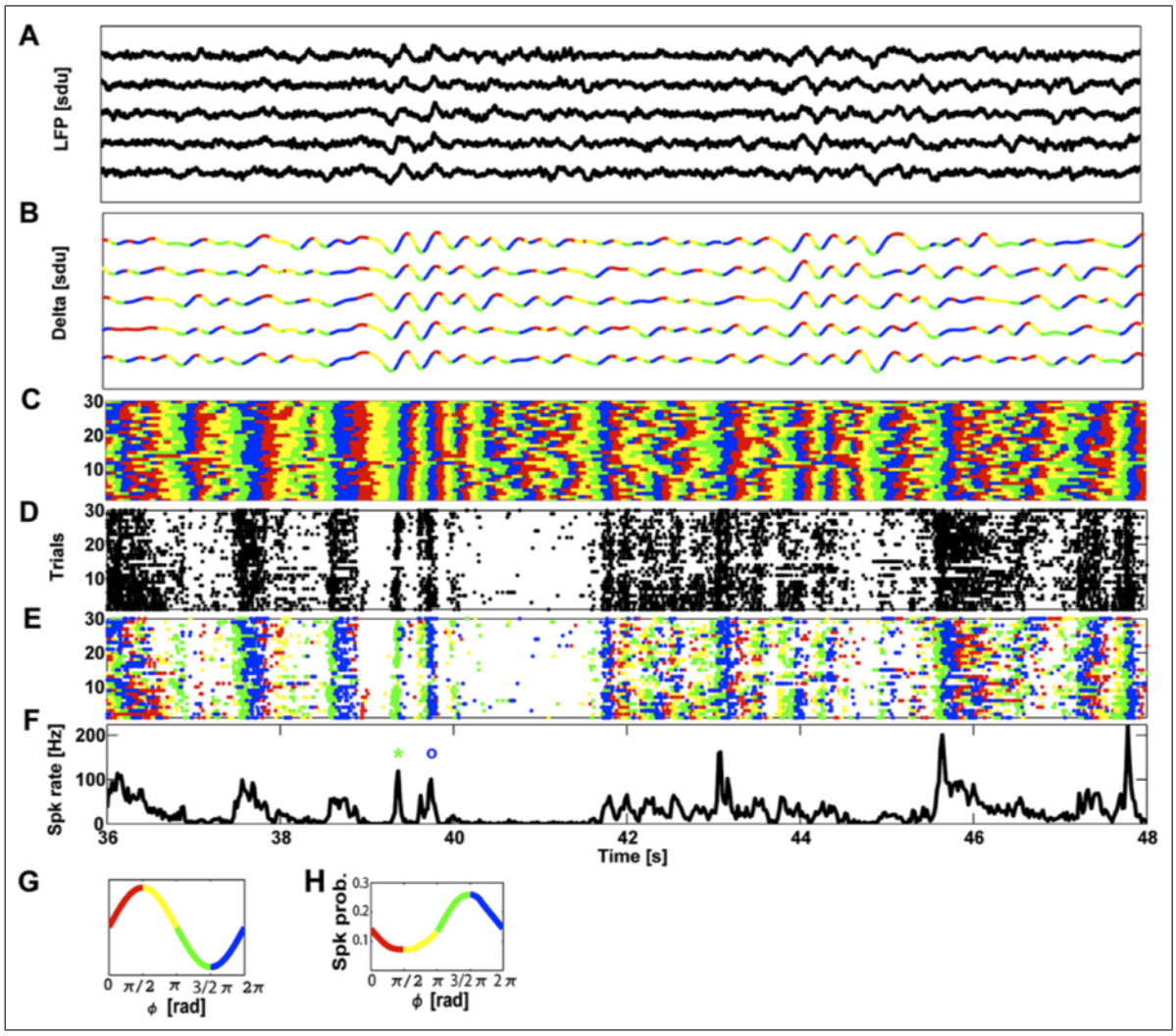

Figure 2.4 Comparison between the time course of the LFP phases and spike times. Reproduced from [51]. (A) LFP recordings showing five repeated presentations of 12-second-long movie stimulus. (B) Band passed voltage traces between 1Hz - 4Hz (delta band), the colour coding represents the phase of the oscillations as given in G. (C) The phase of the band passed voltage traces during 30 repetitions of the movie stimulus. D) Raster plot for the spike times during the same procedure. (E) Colour coded version of the raster plot given in D according to the phase values that were calculated for the delta band. (F) Average spike rate derived from the raster plot in 4-ms-long bins. (G) Colour coding of the phases where a sinusoidal wave is divided into four quadrants. (H) Calculated spike probabilities with respect to the phase of the signal.

if the same or different visual feature elicited the spike rates were only possible due to the extra information carried by the LFP phase. In fact, using information theory the authors have found out that the spike rate alone carried 6.23±0.66 bits of information while the spike times relative to the LFP phase for the 1- to 4-Hz LFPs, the information carried was 9.6±0.94 bits (54% increase) which decreased monotonically with increasing frequency bands which turned out to be equal to that of spike rate above 24-Hz.

As well as spike recordings, LFPs were also employed for decoding motor activity [52, 53, 54, 55]. In their study [52], authors studied LFPs divided into different frequency bands during center-out arm movements from two rhesus monkeys. Direction-dependent increase in LFP amplitudes in frequency domain were reported for three frequency ranges ($\leq$4-Hz, 6- to 13-Hz, and 63- to 200-Hz), before and during movement execution. In contrast $\approx$30-Hz band, decreased amplitude was observed during the task. This led the authors to comment that analysis should be conducted in at least two functionally different regimes ($\approx$30-Hz and $>$60-Hz) for control applications. Two adult rhesus monkeys were trained on a centre-out motor task and LFPs were recorded from the primary motor cortex (MI) by [53]. Initially, subjects performed the task in manual mode where they were able to manipulate the cursor with their hand. Later the task was completed only by an algorithm which used the previous recorded data for movement. Beta band LFP power experienced a sharp drop after movement onset which lasted during movement. Therefore, it is named as a good predictor of stationary period that can be used by BMI applications. In a more recent BMI study [55], authors employed local motor potentials (LMPs) extracted from the LFPs which were recorded from the M1 of two rhesus macaques to control a cursor in x and y directions. It was shown that LMP signal proved a feasible alternative as control signal. Performance of spike-only, LMP-only and spike+LMP (hybrid) decoders were examined under offline and online (closed-loop control) conditions for BMI control. LMP-only decoder proved significantly worse in success rates and metrics such as normalized time-to-target, dial-in time and path length was larger compared that of other methods. Spike-only and hybrid decoding methods displayed comparable performance which was taken over by the other depending on the subject. Further analysis revealed that LMP actually decoded the velocity vector more accurately during hand reaches (offline trials); however, due to the temporal lag in LMP, closed-loop performance was hampered. Hybrid control paradigm triumphed over the other control methods when spike-related information extracted from the channels were lost. This was condition was induced by the authors in order to simulate the temporal effects of chronical implantation of intra-cortical electrodes, where signal loss due to tissue reaction is commonly observed.

2.3 Electrical Stimulation for Artificial Sensation

Electrical stimulation of the nervous system is commonly used for alleviating problems like chronic pain [56], depression [57], Parkinson's [58] etc. The method, is also used for providing auditory [59], visual [60] or somatosensory [61] feedback in neuroprosthetic applications. Tactile feedback is a vital component for limb prostheses for achieving improved motor control. Techniques such as peripheral nerve stimulation and direct stimulation of the brain are termed are used for providing artificial somatosensory feedback.

In one of the early studies of the field [62], possibility of inducing touch sensation was investigated by electrical stimulation of the median nerve in human subjects. It was reported that SA1 units produce sensation of light pressure within a small area located in the receptive field of the unit whereas the activation of RA units seemed to elicit sensations of varying qualities: touch, vibration, and tickle. In their study [63], authors employed a sensory discrimination task where pairs of mechanical indentations with differing frequencies were delivered to the glabrous skin of monkeys. Investigators replaced the second mechanical stimuli of the discrimination task with stimulation pulses that mimic its mechanical counterpart which were delivered to the 3b area of the SI cortex. It was shown that changing the second stimuli with a stimulus train did not change the task performance where animals were still able to discriminate between the higher or lower frequency stimuli. In their follow-up study [64], authors investigated if monkeys could form a memory trace from the electrically delivered stimulus in place of the mechanical, by examining their performance in discriminating between two artificial stimulus. The results showed that discrimination performance was identical in artificial vs real stimulation which made the investigators suggest that activation of their target area in SI cortex is sufficient to initiate all consecutive neural processes associated with flutter discrimination.

A conditioning chamber that delivers vibrotactile stimulus to the glabrous skin of freely behaving rats was constructed by [65], for studying the mechanisms related to the somatosensory system in awake animals. It was reported that constructed sys-

tem allowed succesfull behavioural training of the subjects'. Response accuracies were shown to be lower than that of existing studies that employed whisker stimulation. In a follow-up study [66], authors used the chamber for constructing psychometric response functions from subjects by employing by stimulating the glabrous skin with varying amplitudes and frequencies. The response functions were used to estimate parameters for inducing artificial sensation by intracortical microstimulation (ICMS) of the SI cortex which could be used as a feedback mechanism in neuroprosthetic applications. It was reported that hit rates during the execution of the behavioural task were not significantly different when compared for vibrotactile or ICMS stimulation paradigms. The latest work from the same group [67] employed the previously constructed response functions for providing feedback by ICMS to a conceptual boot neuroprosthesis designed for rats. A psychophysical yes/no detection task was chosen where the vibrotactile mechanical stimuli was delivered to the boots that mechanically isolated the hindlimbs either with ICMS-ON or ICMS-OFF conditions. The subject performance revealed that ICMS-ON condition, which provide artificial somatosensory feedback, allowed significantly better detection. In the study by [68], authors employed ICMS for providing somatosensory feedback to a primate subject that was trained to use a closed loop virtual prosthetic limb system. The system was controlled either by motion tracking of subject's right limb or recorded neural data where touching the object in the virtual environment was signalled by electrical stimulation of the SI. Creation of percepts that can direct the motor control behaviour was successfully achieved which hinted the possibility of a real-time close-loop system enabling simultaneous stimulation and recording on the brain for neuroprosthetics.

2.4 Electrodes for Neural Prostheses

In general, neuroprostheses can be defined as devices that deliver electrical charge to, or record electrical potentials from relevant biological tissues for the purpose of restoring or replacing a lost function. The targeted function can be a motor, sensory or cognitive modality. To be more specific neuroprosthetics are used for either stimulating/inhibiting the neural activity or predicting motor intention by interpreting

the neural activity. A subset of neural prostheses are functional electrical stimulation (FES) devices which help alleviating symptoms for chronic conditions by only providing electrical stimulation without recording. In a broader sense, a neuroprosthetic device records neural activity for predicting the user intention, generates the desired action with an effector and transmits feedback to the user. Therefore, these devices are termed active devices which interact with the user and its environment in real-time.

Electrodes are the component of such devices that forms an interface between the hardware and tissue. More specifically, the electrode-electrolyte interface allows the communication where electrical charge carried by the electrodes from the metal electrode is transduced into electrical charge carried by the ions in the surrounding electrolyte (or vice versa depending on the direction of the current). There are two distinct mechanisms that transduction can occur which are the faradaic and non-faradaic (capacitive) charge transfer mechanisms. Faradaic transfer happens through transfer of electrodes between the electrode material and electrolyte through reduction and oxidation reactions (redox reactions) whereas capacitive transfer involves only the redistribution of charges around the interface which is similar to charge build up at the plates of a capacitor. A faradaic reaction with reaction rate under control of fast kinetics otherwise known as reversible faradaic reactions, allow large currents to occur with small potential deviations from the equilibrium potential of the interface which results in large transfer of net charge. When designing electrical stimulation systems, it is important to avoid initiating irreversible faradaic by keeping the injected charge amount low enough so that unwanted chemical products are not produced.

Brain activity can be recorded from different locations, over the scalp, above or under the dura mater and within the cortex. Non-invasive electrodes located on the scalp or close to the dura provide global activity of the surrounding tissue, however, intracranial electrodes are able to record electrical signals with better spatial and time resolution that make sorting individual neurons possible. Historically, intracranial microwire electrodes were one of the earliest designs [69] that have the advantage of being simple to produce and durable. Commercially available stainless steel and tungsten microwires are still used today. Since they are brain penetrating electrodes, it is hard to

control their bending and the induced foreign body reaction at the implantation site, gradually worsening their signal-to-noise ratios (SNRs). Thin-film microelectrodes were made possible with the advent of photolithography technique. Microwire electrode design allow one active site per shank, however, thin-film arrays can have multiple sites along each probe shank. Also, the distance between each site can be precisely defined and kept during implantation unlike microwires. Silicon, metal, ceramic and polymer-based electrodes were studied in the literature.

Table 2.1
Properties of the materials that are used as electrodes gathered from the literature. Reproduced from [70].

Type	Materials	Electrode Size [μm^2]	Charge Storage Capacity [mC/cm^2]	Charge Injection Limit [mC/cm^2]	Impedance [$k\Omega$]
Metal-based	Pt-Ir	4500	8	0.13	90
	Porous TiN	2830	5	0.7	55
	Ir-Ox	4500	0.2		
		177	29	1	113
	Gold	155	0.4		1500
	Pt-grass	1,256		0.3	100
PEDOT-based	PEDOT:PSS	4,500	123	2.9	6
	PEDOT-CNT	2,830	6	1.25	15
Other carbon materials	Porous diamond	314	10	3	171
	CNTs	50,000		1.6	2
Graphene-based	SLG	2500	0.7		3,000
	Doped-SLG	2500	1.9		600
	rGO-foam	625,000		3.1	0.5
		120,000	62		1

The properties of electrode materials are commonly tested by employing electrochemical methods. Cyclic voltammetry (CV) technique shows occurrence of oxidation reactions where the voltage is slowly increased or decreased while measuring the current. The CV graph is plotted by current with respect to voltage where start of

oxidation of the electrode material is marked by a sharp increase in the curve. Water window is the range which electrode can operate without undergoing hydrolysis and is an indicator of charge delivery capacity. Electrochemical impedance spectroscopy (EIS) is the method of measuring the electrode impedance at multiple frequencies using small amplitude voltage-controlled or current-controlled signals. It is typically performed by scanning the range of frequencies between 0.1-Hz to 10-kHz. Table 2.1 shows the properties of commonly used electrode materials.

2.5 Properties of Graphene and Graphene Electrodes

As being one of the most studied two-dimensional materials graphene has potential for being used in electronic devices, flexible and novel circuit elements, quantum spin manipulation, photonics, energy storage and conversion, composites and many more. Tumor ablation, targeted drug delivery, gene transfection, production of biosensors & bioelectronics, joint prostheses, are some of the possible application areas for graphene related technologies in the biomedical engineering discipline. Although there are certain limitations regarding production techniques graphene has raised a lot of attention from the scientific community, due to its outstanding electrical, mechanical and chemical properties.

2.5.1 Production of Graphene

Attempts on studying graphene as a material can be traced back to the early 20th century. Discovery of the mechanical exfoliation of pyrolytic graphite the "scotch-tape method" [71] which made production of small amounts of the material possible, encouraged researchers to study this unique material more in depth. New techniques such as chemical vapor deposition (CVD) [72, 73] and reduction of graphite oxide (GO) [74, 75, 76] has been developed allowing production of graphene in larger amounts. The current state-of-art in graphene production follows two different approaches; the top-down and bottom-up strategies. Dry exfoliation techniques which employ split-

ting the source material into 2D-layers of graphene using mechanical, electrostatic or electromagnetic forces in different mediums and liquid-phase-exfoliation fall under the top-down procedures. Growth of graphene on metals and silicon carbide (SiC), CVD, molecular beam and atomic epitaxy, chemical synthesis are among the bottom-up approaches for producing graphene [77]. Each approach has its own benefits and caveats, for example, the best charge carrier mobility (up to 140k-cm^{2}V^{-1}) is acquired with exfoliation [78] however, it is only possible to produce the material with a surface area that is in the micron scale. Table 2.2 shows different charge carrier mobilities as obtained by employing different production techniques. CVD is currently the most popular technique employed in production of graphene because it allows production of larger amounts while providing plausible crystal quality [79].

Table 2.2
Charge carrier mobility of graphene produced by different manufacturing methods. Reproduced from [80].

Method	Crystallite size (μm)	Sample size (mm)	Charge carrier mobility (at ambient temperature)
Mechanical exfoliation	>1,000	>1	>2x10^5 and >10^6(at low temperature)
Chemical exfoliation	≤0.1	Infinite as a layer of overlapping flakes	100(for a layer of overlapping flakes)
Chemical exfoliation via graphene oxide	≈100	Infinite as a layer of overlapping flakes	1 (for a layer of overlapping flakes)
CVD	1,000	≈1,000	10,000
SiC	50	100	10,000

Exfoliation procedures can be broken into following steps which starts with pre-treatment for expanding the distance between layers is followed by exfoliation, stabilization of graphene layers and separation of graphene nanosheets. The van der Waals forces within graphite are broken down allowing the extraction of graphene sheets that form graphite. Solid or liquid phases of graphite are used for the process by employing procedures such as sonication shear mixing or ball-milling. Sonication technique uses ultrasonic waves for breaking the bonds while shear mixing [81](employs centrifugation of graphite powder with addition of a solvent using a mixer device that

has a tightly spaced (≈100-μm) rotor-stator gap.

Generally, the CVD method can be summarized as decomposition of a carbon source (solid, liquid or gas) onto a metallic surface until it forms a single layer carbon membrane in the reaction chamber. The method has different subtypes such as thermal, plasma enhanced, cold wall, hot wall, reactive and many other. Growing graphene by CVD on dielectric substrates would ideally be the best approach which is essential for production of flexible electronics however the current technology is not there yet. Nonetheless, by taking advantage of the thermal CVD method Bae and colleagues [82] developed a procedure for enabling roll-to-roll production of graphene on dielectric substrates. The team employed a 30-inch copper foil for growing graphene by CVD then etched the copper layer and finally released graphene onto the target substrate which hinted the possibility for continuous production of graphene based electronic devices. Another evidence for future availability of graphene based consumer goods came from Lin et al. [83] in which an integrated circuit was manufactured using graphene for building a broadband radio-frequency mixer that exhibited outstanding thermal stability.

2.5.2 Material Properties

The material consists of a single layer sp2 bonded carbon atoms which are formed in a hexagonal lattice structure. Graphene exhibits very high electrical and thermal conductivity, has exceptionally high mechanical strength and flexibility, is transparent, has a large surface area, has effectively zero mass and behaves as an impermeable membrane. Lee et al. [84] has used a custom setup for studying the mechanical properties of the material with a 5-by-5-mm array of holes on which a monolayer of graphene is suspended for indentation under atomic force microscopy (AFM). The breaking strength of the material was reported to be 42 N/m and the value of the second order elastic stiffness was found to be 340±50-N/m corresponding to a Young's Modulus of 1±0.1-TPa making monolayer graphene the "strongest material ever measured".

Single layer graphene is identified by the position and shape of its two main peaks; G (1580-cm^{-1}) and 2D (2690-cm^{-1}) in the Raman spectrum [85]. If the layers of the material increased a splitting of the 2D peak and shifting of G peak were observed. Therefore, using Raman Spectroscopy number of layers of graphene can be determined by using the intensity ratios of the defined peaks. Additional D (1350-cm^{-1}), D' (1620-cm^{-1}) and D+G (2940-cm^{-1}) peaks were detected in the spectrum if the material sample is not pristine. These peaks occur due to the defects in the atomic structure of the material and allows characterization of disorder in the produced sample. Raman spectrum for the CVD graphene film grown on Cu substrate is given in Figure 2.5.a.

Partoens & Peeters [86] has shown that the electronic properties of graphene are greatly dependent on the number of atomic layers that the material contains and exhibits the properties of graphite when 10 layers are reached. They have distinguished the single- and double-layer graphene to be zero-gap semiconductors -which is an important property for using the material in a FET configuration- however it has also been reported that between 3-10 layers electric fields get very complicated. The charge carrier mobility of the material is reported to be exhibiting very weak dependence on the surrounding temperature [87] which could possibly possess an important benefit for electrical circuit design. Monolayer graphene has been defined as the most perfect 2D electronic material possible in nature due to its lattice geometry for electron hopping [88] and carrier density of suspended graphene on substrate has shown to achieve 2x105 cm^2/VS [89]. In addition to its remarkable mechanical and electrical properties graphene is a remarkable alternative for bioelectronic applications considering it has proven to be chemically stable [90] and biocompatible [91].

Nayak and colleagues [92] reported that presence of CVD grown graphene in the medium during growth of stem cells did not affect their shape or growth which led them to declare that graphene can safely be used. Furthermore, it was concluded that graphene coating accelerated the differentiation of human mesenchymal stem cells (hMSC) in the presence of an osteogenic medium. In another study [93], authors tested biocompatibility of CVD graphene on primary adult rat cardiac cells. In comparison to glass substrate graphene showed significantly higher cell density 24-h after cell plan-

tation. Additionally, contraction dynamics of the employed cardiomyocytes were not altered. Human neural stem cell (hNSC) differentiation into neurons on regular glass versus CVD graphene coated glass surfaces were investigated by [94]. Graphene allowed faster cell adhesion and promoted differentiation toward neurons than glial cells. Study concluded that graphene allowed enhanced differentiation of hNSCs'.

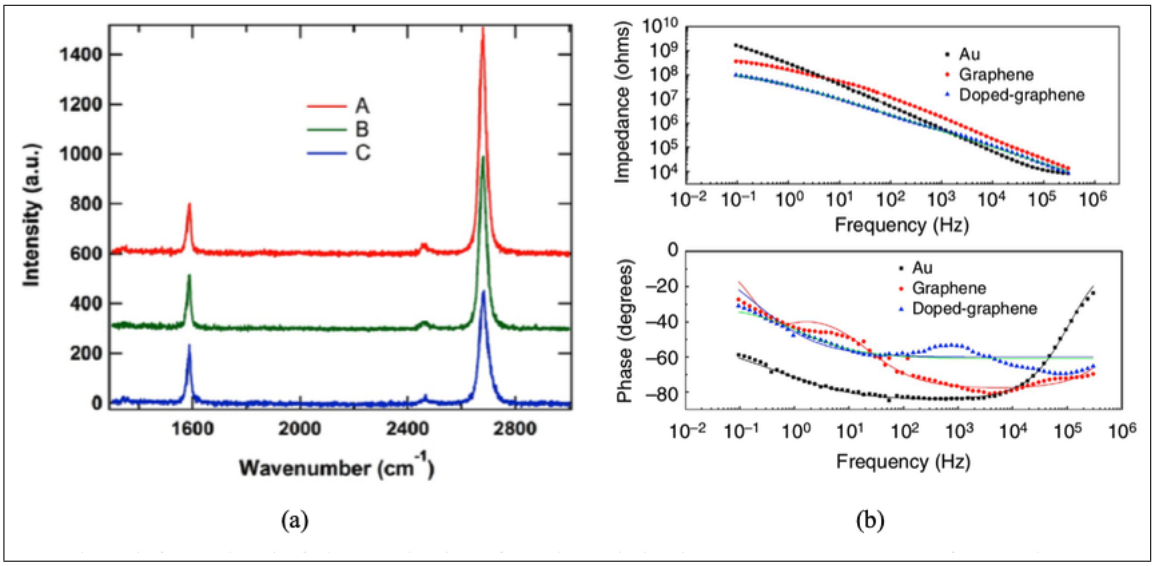

Figure 2.5 Atomic and electrochemical characterization of graphene derivatives. (a) Raman spectrum from various spots of a CVD graphene film grown on a Cu substrate and transferred to SiO2/Si. G (1580-cm^{-1}) and 2D (2690-cm^{-1}) peaks are shown which are characteristic to graphene. Disorder peaks were not prominent which implied that the material had low-disorder in its atomic structure. Reproduced from [85]. (b) Electrochemical impedance spectroscopy comparison among CVD graphene (doped and undoped -with nitric acid-) and standard gold electrodes. Reproduced from [95].

2.5.3 Biomedical Applications

Research efforts investigating the possibility of employing graphene in biomedical applications started appearing about four years after Novoselov and colleagues published their work on scotch-tape method [71]. In their study [96], authors employed nanographene oxide (NGO) and branched polyethylene glycol (PEG) to obtain a biocompatible conjugate which was then used for attaching cancer cell killing SN38 molecules while creating NGO-PEG-SN38 complex. This process allowed SN38 which is a water insoluble molecule to be dissolved in water while maintaining the molecule's potency in fighting cancer cells. Another study [97] that used the same molecular conjugate NGO-PEG succeeded in both selectively imaging and killing the cancer cells by

adding agents such as Doxorubicin and Rituxan to the complex. In a photothermal ablation study [98] authors have shown that near-infrared excited graphene nanoparticles can be successfully employed for killing cancer cells. Additionally, the study compared the performance of carbon nano-tubes (CNTs) to that of graphene nanoparticles for the given task. Even though both are structurally very similar (sp2 bonded materials) the performance of the graphene nanoparticles was superior due to their smaller size and better dispersivity inside target cells.

Apart from drug delivery and ablation studies graphene has found some other applications in medical practices. Fan and colleagues [99] fabricated graphene-chitosan composite films and measured their mechanical properties by nanoindentation method. The elastic modulus of chitosan was increased about $\approx$200% and the composite was shown to be biocompatible making it a potential candidate for tissue scaffolds. Mohanty and Berry [100] have studied the possibility of interfacing graphene derivatives with biological systems for creating novel hybrid biodevices. They have shown that chemically modified graphene can attach to bacterial cells, tether and hybridize DNA molecules on their surface and can bind with polyelectrolytes which hints the possibility for invention of next-generation tools such as bioelectronic devices and nano-scale bioprocess analysis tools.

2.5.4 Graphene Electrodes

Owing to its high surface area, excellent electron mobility, biocompatibility and flexible structure, graphene is proving to be a reliable material for neural interface systems. Electrochemical characterization studies indicated that graphene and graphene composite materials have superiority in terms of certain important measures that determine electrode performance over currently used materials. Zhou and colleagues [101] shared charge-transfer resistances (R_{ct}) of graphite glass carbon (G/GC) glass carbon (GC) and reduced graphene oxide modified glassy carbon (rGO/GC) electrodes as 407.6-Ω, 200.7-Ω and 160.8-Ω respectively.

The authors of [102] investigated properties of graphene foam electrodes which were directly grown on polyimide substrate by laser pyrolysis. A portion of the electrode samples were doped with nitric acid (HNO_3) for performance comparison. CV measurements yielded a water window of (-0.8V to 0.8V) for Au, (-0.8V to 1V) for undoped graphene and (-1.3V to 0.7V) for HNO_3 doped graphene electrodes hinting that graphene exhibits better charge storage capacity. The impedance values at 1-kHz were given as 27.3-kΩ, 637-Ω and 519-Ω for Au (250-μm x 250-μm), graphene (300-μm x 300-μm) and HNO_3 doped graphene (300-μm x 300-μm)electrodes respectively. EIS results after and before 1 million stimulation cycles did not show drastic impedance changes for the electrodes. The doping increased charge injection capacity (CIC) of graphene from 2-mC/cm^2 to 3.1-mC/cm^2

Kuzum and others [95] compared 50-μm x 50-μm Au and HNO_3 doped graphene electrodes for recording bicuculline induced spiking activity. Root mean square noise was measured as 30.99$\pm$1.15-mV and 165.64$\pm$17.87-mV for doped graphene and Au electrodes, and the SNR values were reported as 40.8 and 7.7 respectively. Interestingly it was shown that although there is a big difference in impedance values at 1-kHz for 500-μm x 500-μm Au (17.2-kΩ), and 50-μm x 50-μm doped graphene (541-kΩ), the two electrodes showed comparable RMS noise. Power density spectra comparison between Au and graphene electrodes has illustrated a significant 60-Hz interference noise reduction -approximately 100 times- for the doped graphene electrode which lead the authors to suggest that doped graphene is especially advantageous for studying LFPs. EIS analysis (see Figure 2.5.b) has also shown a similar benefit of employing doped graphene electrodes in which the impedance characteristics is more favourable for graphene below 500-Hz. The study also cleverly made use of the transparency property of graphene by conducting simultaneous calcium imaging.

In the porous graphene study [102], somatosensory-evoked potentials (SEPs) were recorded in the form of LFPs, from the barrel cortex by electrical stimulation of the rat mystacial pads. Power spectral density analysis has shown peaks centred around 0.8-Hz (delta), 40-Hz (gamma), and 90-Hz (high-gamma). Additionally, stimulation of the motor cortex representation of the ankle and knee flexors was investigated. Muscle

movement has been reported between 0.75- to 1.25-mA, limited by the Shannon criteria where 1.25-mA corresponds to k=1.85.

Since graphene acts as zero-gap semiconductor and transistor design allows for intrinsic signal amplification, graphene-based transistor configurations were investigated for recording neural activity. Karni et al. [103] recorded activity from embryonic chicken cardiomyocytes using nanowire graphene field effect transistors. In [104, 105, 106] solution gating in the transistor design for exposing the neurons directly to the gate site was realized. Blaschke and colleagues [106] recorded bicuculline-induced and visually evoked LFP activity from the cortex of anaesthetized rats using both a 16-channel graphene SG-FET (transistor active area of W = 20-μm, L = 15-μm and a 32-channel Pt MEA device (mix of thirteen d = 50-μm, and eight d = 10-μm contacts) simultaneously. The SNR calculated from the recordings of bicuculline-induced activity was found to be 62$\pm$5.8 for the graphene array 26$\pm$5.5 for 8 small Pt and 53$\pm$11 for 13 large Pt electrodes whereas for the spontaneous activity recordings the calculated values for SNR was 9.85$\pm$0.67, 6.02$\pm$0.68 and 8.33$\pm$1.05 respectively. Despite its smaller contacts, the g-SGFET exhibited highest mean SNR while providing a spatial resolution comparable to that of the small Pt electrodes. The time frequency analysis of the spontaneous LFP recordings reveal higher power components below 10-Hz whereas biccuculine induced activity a more spread activation is observed still focusing around 10-Hz. The experiments were followed by a brief immuno-histology study which examined the microglial activation and inflammatory processes by quantifying the changes in microglia based on solidity and circularity indices. The changes in indices were not significantly compared to the surgically naive subjects at any of the time points on the other hand, sham operated animals (sacrificed 4 days after surgery) on the other hand has shown significant change in the solidity and circularity indices due to surgical trauma.

Charge transfer properties of graphene microelectrode arrays were characterized together with realizing simultaneous calcium imaging on transgenic GCaMP6f mice [107]. The study provided EIS and CV results as well as spatiotemporal propagation dynamics of electrical stimuli and compared anode and cathode leading stimulation

dynamics. Average impedances at 1-kHz were given as 286.4±92.6-kΩ, 248.7±125.0-kΩ, and 215.7±120.4-kΩ for the good channels of graphene electrodes with diameters; 100-, 150- and 200-μm respectively and the phase plots for 1- to 10-kHz indicated a capacitive charge transfer mechanism which is advantageous for electrical stimulation. Impedance characterization before and after stimulation revealed that for the 150-μm contacts stimulation amplitudes over 120-μA (78.3-μC/cm^2) caused failure of the contacts in average. The peak-neuronal response was marked within 200- to 400-ms window post-stimulus by the fluorescence intensity. Lastly, the study concluded that cathode leading elicited stronger neural response and was more efficient at delivering charge to the brain.

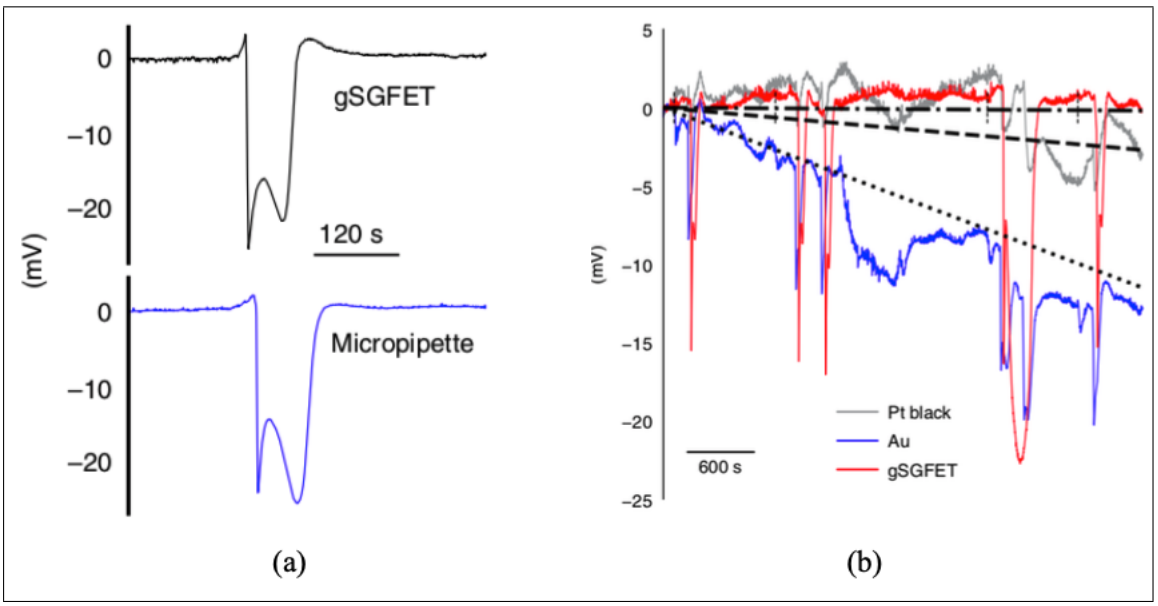

Figure 2.6 Comparison of g-SGFET performance for recording infraslow brain activity. (a) depicts the similar shape and time-course of the recorded CSD event in response to KCL administration by g-SGFET and Ag/AgCl wired glass micropipette. (b) shows the superiority of employing g-SGFET over Au and Pt-black microelectrode arrays for recording CSD activity. Reproduced from [108].

In a very recent study [108] infraslow brain activity (signals below 0.1-Hz) were recorded with g-SGFETs for investigating the cortical spreading depression (CSD) dynamics which is a slow propagating wave of near-complete depolarization that was reported to play an important role in clinical setting for inferring information about the pathophysiological condition of the brain. Potassium chloride (KCL) induced CSD activity was recorded for investigating the g-SGFET performance in comparison to glass micropipette, Au and Pt-black microelectrodes. Figure 2.6.a depicts the similar-

ity of the recorded CSD signals with Ag/AgCl wired glass micropipette and g-SGFET recordings. Simultaneous recordings using the g-SGFETs, Au and Pt-black microelectrodes revealed that g-SGFETs recorded significantly higher amplitudes for CSD events (-13.3±1.8-mV) in comparison with Au (-4.7±1.6-mV) and Pt-black (-3.0±0.7-mV) microelectrodes. Furthermore, Au and Pt-black microelectrodes exhibited very large baseline drifts in the recorded signals as given in Figure 2.6.b.

3. METHODOLOGY

3.1 Subjects

Twelve Wistar Albino rats (8 females and 4 males) were used in experiments. Figure 3.1 depicts the age and weight distributions of the subjects with a mean age of 10.94±4.40-months and a mean weight of 309.32±101.59-gr. The experiments were approved by Boğaziçi University Institutional Ethics Committee for the Local Use of Animals in Experiments.

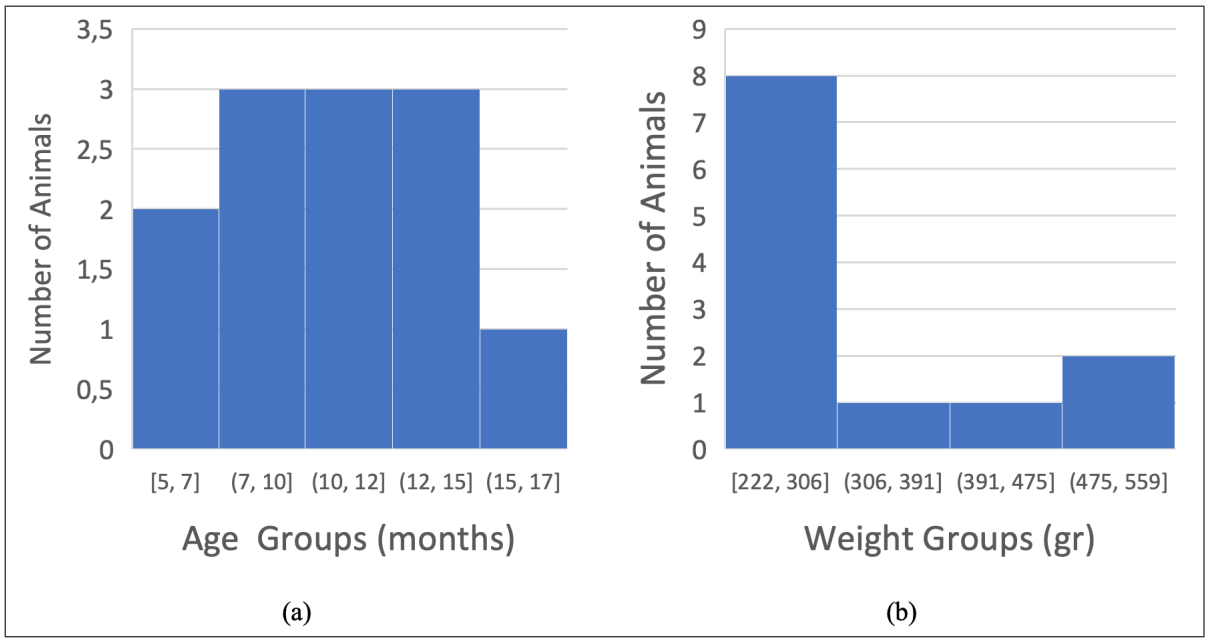

Figure 3.1 Age (a) and weight (b) distributions of the subjects.

3.2 Apparatus

The experiment setup is given in Figure 3.2. MATLAB Version R2008a (Math Works) software was selected for collecting and processing the data. A custom MATLAB script was used for generating the stimulus waveforms and recording the voltage

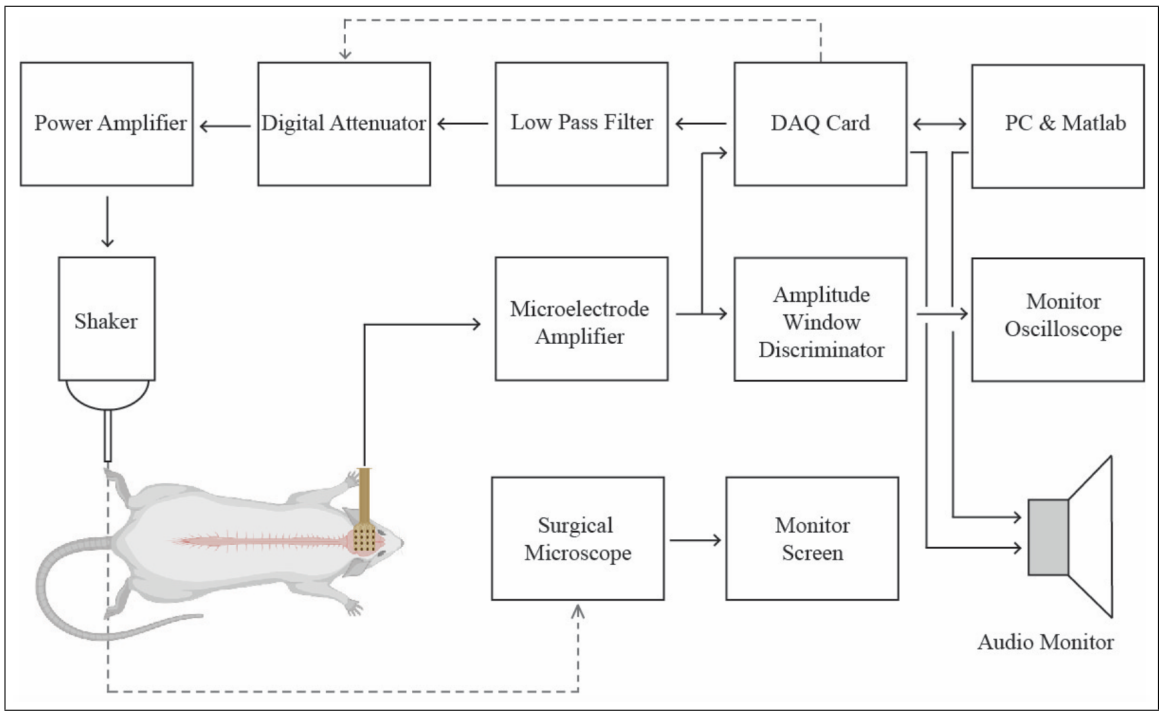

Figure 3.2 Block diagram of the experiment setup.

readings from the electrodes in time-series format. Experiment parameters such as stimulation frequency, attenuation, number of trials per attenuation level, timing and duration of the stimulus delivery and total trial duration were controlled by the MATLAB code. Stimulus waveforms were generated on MATLAB and were converted into analog signals by the USB-6251 DAQ card (National Instruments). The analog signal was sent to a custom-made 1-kHz low-pass filter for improving the SNR. A digital attenuator (model V2.0C; ISR Instrument) controlled by MATLAB was employed for attenuating the signal. The stimulation amplitudes for each frequency were adjusted by attenuation of the signal in dB scale (see section 3.3.4). Output from the attenuator was sent to a custom-built power amplifier for driving the shaker (V101; Ling Dynamic System) which was mounted on a boom arm that had three degrees of freedom. A micro-drive stage which was fitted between the shaker and the boom arm allowed fine-tuning the amount of static indentation applied by the shaker -movement in z-axis- on the target skin area. The shaker was equipped with a plastic contactor (diameter: 1.9-mm) for stimulating the skin. Von Frey hairs were employed for mapping receptive field of the studied area. The shaker was periodically calibrated via a fiber optic

displacement sensor (Fotonic Sensor; MTI Instruments) for ensuring its precision.

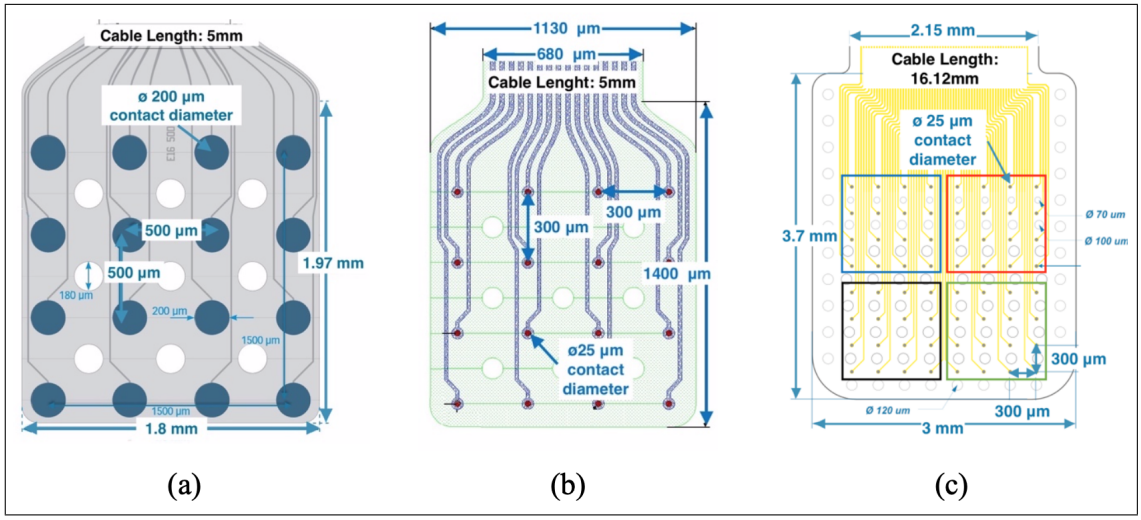

Figure 3.3 Schematics of the electrode arrays that were employed during the experiments. Active side of the electrode contacts are facing into the screen. Cable/trace length indicates the distance between the PCB and top end of the electrodes. (a) NN-arrays, only employed during stimulation trials (b) NN25-arrays, (c) GR-arrays used in recording experiments. The colored boxes indicate the divided four groups of the electrode for allowing compatibility of graphene with the recording set-up. Additionally, this allowed one-to-one comparisons between the NN25- and GR- arrays due to the active recording areas being identical.

Two distinct epidural thin-film electrodes were employed for recording surface potentials from the cortex (see Figure 3.3):

- The E16-300-5-25 array (NeuroNexus Technologies):16-ch micro-ECoG array with platinum-iridium contacts fixed on polyimide substrate (width: 1.4-mm, length: 1.13-mm, contact diameter: 25-μm). This type of electrodes will be referred to as the "NN25-arrays" from this point on. Three different arrays (NN25#1, NN25#2 and NN25#3) were employed during recordings.

- The graphene electrode (Advanced Electronic Materials and Devices Group, ICN2): 64-ch micro-ECoG array with CVD graphene contacts fixed on polyimide substrate (width: 3.7-mm, length: 3-mm, contact diameter: 25-μm). This electrode will be referred to as the "GR-arrays" from this point on; since, the electrode was divided into 4 groups of 16 channels (treated as 4 distinct arrays). A single graphene electrode and three of its channel groups (GR#1-green GR#1-black and GR#1-blue) were actively used throughout the experiments.

One graphene electrode was acquired from the Advanced Electronic Materials and Devices Group which is a research group operates under the Catalan Institute of Nanoscience and Nanotechnology (ICN2) lead by Prof. Jose Antonio Garrido. The array is still under development and unlike NN25-arrays has not yet been commercialized. Voltage signal from the electrodes were sent through a wide-band headstage (Plexon) and amplified by PBX Preamplifier (Plexon) in the LFP band (1-pole low-cut at 0.7-Hz and 1-pole high-cut at 300Hz) with 1000x gain. A window discriminator (WPI-121) was employed for distinguishing the signal peaks and traces were observed on a monitor oscilloscope (Hitachi) together with the auditory monitoring of the signal using standard PC-speakers. A parallel circuit carried the output signal into the USB-6251 DAQ card which digitized the analog voltage signal and transferred to MATLAB for storage. Impedance characteristics of the electrodes were periodically measured by Omega-Tip-Z (World Precision Instruments) which operates at 500-Hz sampling frequency.

A stereotaxic frame with micro-drives in three perpendicular axes (Kopf) and standard surgical tools were used during the surgery. A heating pad with a rectal thermometer for continuous measurement (Physitemp) maintained the body temperature. Craniotomy window was opened via cutting holes on the skull via a motor driven surgical drill (Foredom SR) that is attachable to the Kopf frame. A surgical microscope (Leica) was employed throughout the experiment for monitoring the brain and the steps of the operation in finer detail. The whole experiment setup was placed on a floating table which was enclosed by a Faraday cage.

3.3 Procedure

3.3.1 Animal Handling

The subject of the experiment was weighted for calculating the required volume of each anesthetic agent in a full dose of the anesthetic cocktail. The cocktail was prepared with a fixed amount of xylazine (10-mg/kg), however the ketamine amount

was readjusted between (60 - 100 mg/kg) by taking animals' gender and weight features into account. In the beginning of an experiment a full dose was administered to every animal intraperitoneally (IP). Throughout the experiment animals' pedal and palpebral reflexes were periodically monitored and 1/3 shots were administered as required. After the induction of anesthesia skull area was shaved with a standard hair trimmer and the animal was placed on the heating pad together with the insertion of the rectal thermometer. Following placement on the stereotaxic frame, injections of furosemide to prevent edema, atropin for decreasing saliva production and mannitol for lowering increased intracranial pressure were administered. At the end of an experiment animal was either euthanized by thiopental injection (200-mg/kg) or sent to perfusion for being used in another study.

3.3.2 Surgery

Surgical procedures started as soon as the animals' body temperature stabilized around 37°C and surgical anaesthesia was achieved with no reflexes. Incisions of 3 - 3.5 centimeters, were applied on the scalp by approximately following the mid-line of the skull in the axial plane. The connective tissue over both hemispheres were removed for allowing easier operation on the area of interest. Micro-bleeding due to dissection of capillaries were suppressed using medical sponges that accelerates coagulation. The anatomical landmarks on the skull were located and marked with a pen after cleaning the area with saline solution. For correct stereotactic coordinates, the flatness of the skull was ensured by checking the z-coordinates. The craniotomy window -preferentially on the left hemisphere- was opened via drilling holes around a pre-defined rectangular area and carefully lifting the separated skull piece making sure that the dura was left intact. Throughout the experiments different sized craniotomy windows (see Figure 3.4.a) were used due to different sizes of the employed electrodes.

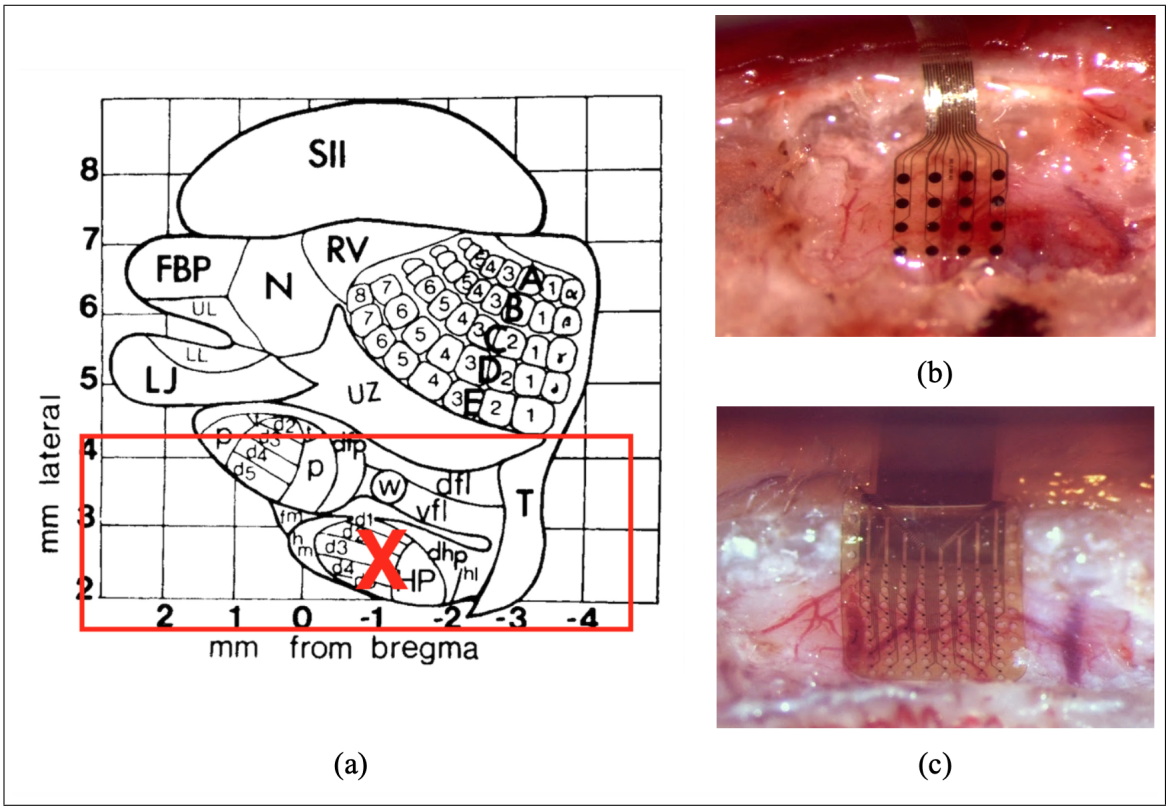

Figure 3.4 Illustration of the craniotomy window and placement of different electrode geometries. (a) Drawing of the target cortical structure. The red rectangle demonstrates the approximate size of the craniotomy window which varied among experiments while the red cross shows the target area for placing the electrodes. Modified from [8] (b) NN-array placement on the targeted cortical structure. (c) GR-array placement with a larger craniotomy window. The array was rotated along the z-axis when recording the from the distal groups of channels (blue and red groups) for making sure that channel distribution over cortex is standardized among electrodes.

3.3.3 Electrode Placement

Following craniotomy completion, the cortex was cleaned with saline solution and excess fluid was dried before the placement of the selected array. NN25-electrodes and the GR-electrode had different sizes, channel counts, different dimension for the polymide substrate and different terminations. Therefore several steps were followed to standardize the placement of the electrodes (see figure 3.4.c):

- A breakout PCB (see Figure 3.5) was used for the 64-Ch GR-electrode. It consisted of 4 omnetics type connectors for 4 blocks of 16 channels.NN25-electrodes did not require an adapter PCB.

- The stereotaxic coordinates were zeroed by aligning the rightmost bottom channel of the employed array over the bregma. For NN25-arrays the alignment was always done against "Ch-9"; however, due to the required rotation for using the blue or red block of the GR-array, the alignment was done for different channels.

- Due to the flexible structure of the electrodes and different trace lengths in NN25 vs. GR-arrays, targeting identical coordinates was not perfect. However, the electrode placement started with the same orientation (perpendicular over the bregma) and similar distance was travelled in z-coordinates for placement as precise as possible.

- For placement the stereotaxic map by [8] was used. The hind paw representation was referenced to AP:0-mm, ML:2-mm on the SI cortex. We did not study the anatomical variability among subjects.

Voltage traces from the channels of each array were observed in a consecutive order for verifying vibrotactile responses and channel with the highest LFP activity was noted during this process. The selected channel was then used for receptive field mapping as explained in the following section.

3.3.4 Vibrotactile Stimuli

It is necessary to underline that a natural vibrotactile stimulus targeting the mechanoreceptors in the glabrous skin of the hind paw was employed in the study. This is important for two reasons; firstly, the literature is sparse on this stimulation method and secondly, the targeted mechanoreceptors are also present in humans which could allow direct translation of the findings to be used in neuroprosthetic applications. The probe of the shaker was placed so that a static indentation of 0.5-mm was applied on the skin and the mechanical stimulus was superimposed on the indentation. Vibrotactile stimuli were delivered as bursts of sinusoidal displacements of frequencies (5-, 40- and 250-Hz) with a duration of 0.5-s and rise/fall times of 50-ms (see figure 3.6). The sinusoidal bursts increased and decreased as cosine-squared functions. Total trial

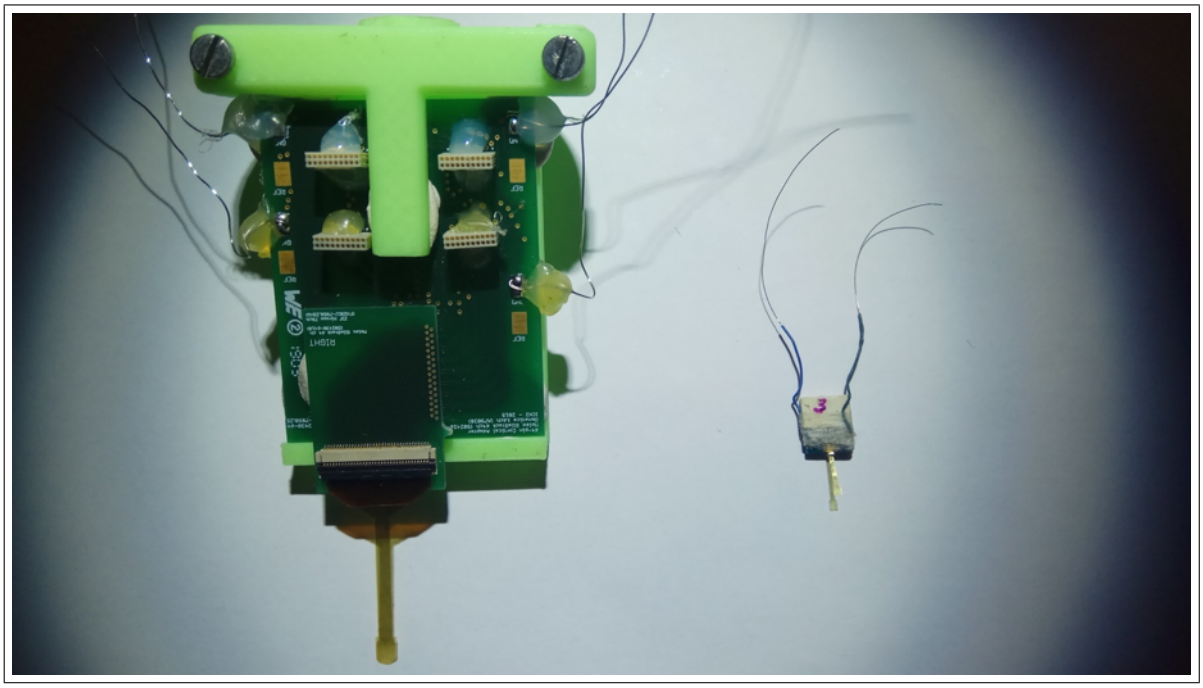

Figure 3.5 Pictures of the employed electrodes that were used in the experiments. On the left-side GR-electrode and its breakout PCB is shown. NN25-electrode which can be seen on the right-side is considerably more compact and less prone to electrical and magnetic interference due to its design.

duration was adjusted as 2-seconds with stimulus delivery at t=1s and inter-stimulus-interval of 3-seconds. As mentioned earlier the amplitude was changed by using the attenuator. Table 3.1 includes the corresponding amplitudes for attenuation levels employed by each stimulation frequency. It is important to note that, [109] reported that skin decoupling effects were observed while delivering sinusoidal vibrations with amplitudes over 250-μm. Therefore only data from attenuation levels between 35 - 15 dB which correspond to amplitudes below 250-μm were used in statistical analysis.

3.3.5 Recording Evoked Potentials

Once the channel that yielded the highest amplitude was designated, the hind paw was fixed with modelling clay -glabrous skin was facing up- and stimulated using a range of Von Frey hairs while monitoring the response on the oscilloscope. A receptive field map of the hind paw was generated and the location for placing the shaker probe

Table 3.1
Conversion table for attenuation levels with respect to the stimulation frequencies. The indicated voltages were required for driving the shaker at given frequencies for obtaining the corresponding travel distances of the shaker tip.

Attenuation Level	5-Hz @ 1V	40-Hz @ 1V	250-Hz @ 10V
35-dB	27-μm	28-μm	19-μm
30-dB	48-μm	49-μm	34-μm
25-dB	85-μm	87-μm	60-μm
20-dB	150-μm	154-μm	105-μm
15-dB	264-μm	271-μm	187-μm
10-dB	464-μm	478-μm	330-μm
5-dB	817-μm	843-μm	585-μm
0-dB	1437-μm	1488-μm	1035-μm

was established by selecting the point that yields the highest evoked response amplitude on that channel. Typically, this location was in the lower part of the hindpaw away from the digits for mechanical stability.

Somatosensory evoked responses from the hind paw representation of rats' SI cortex were collected in the LFP range (0.7 - 300 Hz). The order of the stimulation side (contralateral or ipsilateral) and the stimulation frequencies (5-, 40- and 250-Hz) were randomized in each experiment. The stimulator was lowered to the hind paw on to the pre-defined stimuli delivery location. Same location was used for both contralateral and ipsilateral stimulation conditions which was determined by mapping of the contralateral paw. Ten trials for each attenuation level starting from 35-dB to 0-dB with increments of 5-dB were recorded from 13 out of the available 16 channels per electrode. The 3 channels were excluded due to the available inputs in the recording set-up. After the recordings for both contralateral and ipsilateral stimulation was completed for one type of electrode, this electrode was removed and other type was placed. The same procedures were applied. In each experiment the electrodes were placed in a randomized order.

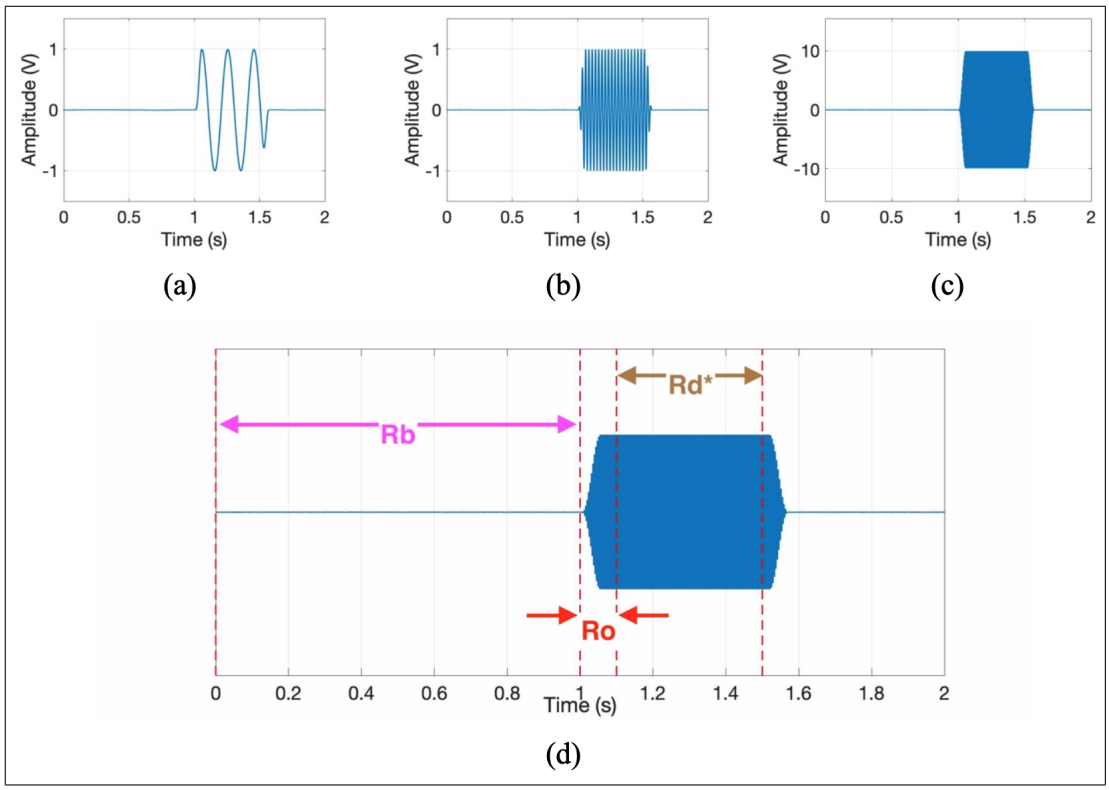

Figure 3.6 Mechanical stimulation waveforms and analysis time windows. (a) 5-Hz stimulus. (b) 40-Hz stimulus. (c) 250-Hz stimulus. Note the change in amplitude scale due to higher driving signal required for the shaker at 250-Hz stimulus to obtain similar levels of mechanical vibrations on the skin. (d) Time windows for analysis (Rb: Baseline, Ro: Onset period, Rd*: Remaining period of stimulus duration.

3.3.6 Cortical Stimulation Trials

Electrical stimulation of the cortex was attempted for investigating the viability of using surface electrodes for inducing muscle movement in anesthetized animals. Due to the safety limits another electrode type with large active sites was used (diameter: 200-μm, NeuroNexus). The upper limit for safe stimulation was calculated as 0.6-mA by the Shannon equation [110] with k = 1.85 as suggested by [111]. Seven different subjects were stimulated by using both monopolar and bipolar stimulation, by also varying different active sites on the electorde array in the range of 0.1 to 1.5-mA bipolar current pulses (0.1-s duration and 250-μs phase duration). Pulse trains of both anodic and cathodic nature were applied using a neurostimulator device (Axonic Neurostimulation Systems).

3.4 Data Analyses

Recorded data were filtered in MATLAB with a 2^{nd}-order zero-phase Butterworth bandpass filter (4 - 312.5 Hz). Each trial was plotted against time for visual inspection which allowed detection of any noise or artefact related disturbance in the signal. Trials deemed bad were excluded from further investigations. In order for visualizing the somatosensory evoked potentials the background EEG activity, which is not synchronized with the stimulus, was averaged out by computing the mean of all traces that belonged to a single attenuation level and plotted with respect to time (trial-averaged analysis). Time-frequency analysis were conducted by employing wavelet transformation (Eq.3.1).

$$W^f(s,d) = \int_{-\infty}^{+\infty} f(t)\frac{1}{\sqrt{s}}\psi(\frac{t-d}{s})dt \tag{3.1}$$

where a Morlet wavelet function ($\psi(z) = \pi^{-\frac{1}{4}}e^{-\frac{1}{2}z^2}e^{-iw_0z}$) was selected as the mother wavelet because of the transient nature of recorded signals.

While running the experiments it was observed that the GR-arrays channels were not very stable and started breaking down with usage which led to GR-arrays having a reduced number of data-points compared to that of NN25-arrays even within the matched group. In order for mitigating any bias condition that could have been created due to the stated reason, the data were further compartmentalized into "best-channel" and "all-channel" groups. When comparisons were being made for the former group, only data from the best-channels (highest LFP response) of each experiment were used, whereas in the latter, data from all channels were included.

3.4.1 Root-mean-square Measures

Three different time windows were defined for analyzing the change in root-mean-squared (RMS) voltage levels (see Figure 3.6.d)on every trial:

- Rb: Baseline window (t=0-1 seconds) enclosing the timepoints from the beginning of a trial until stimulus presentation;
- Ro: Onset window (t=1-1.1 seconds) enclosing the first 100-ms of the stimulus presentation;
- Rd*: Remaining window (t=1.1-1.5 seconds) enclosing remaining 400-ms of the stimulus delivery

RMS values were calculated in MATLAB by using Eq.3.2; where X is the window of interest, N is the total number of samples in a given window and Vn is the voltage value at that time point. Change in neural activity due to hind paw stimulation was investigated by subtracting Rb RMS from the Ro and Rd* RMS values by using two separate calculations ("Ro-Rb" and "Rd*-Rb"). RMS data calcualted as such, were grouped into best-channel and all-channel groups. As the name suggests best-channels data contains the channels with highest RMS values averaged across all amplitude and frequency levels within each experiment. Ro-Rb and Rd*-Rb were plotted as a function of stimulus amplitude at different stimulus frequencies.

$$V_{RMS_X} = \sqrt{\frac{1}{N}\sum_{n=1}^{N}|V_n|^2} \tag{3.2}$$

3.4.2 Coherence Measures

For coherence measures, two particular frequency bands were chosen for statistical analysis:

- Narrow-band: For each stimulation frequency the narrow-band was determined by [0.8fs to 1.25fs] where fs is the stimulus frequency. The investigated bands were 4 - 6.25 Hz, 32 - 50 Hz and 200 - 312.5 Hz for 5-, 40- and 250-Hz stimuli.
- Wide-band: Fixed for all stimulation frequencies and includes the whole spectrum [4 - 312.5 Hz].

Magnitude-squared coherence was calculated according to Eq.3.3 for LFP signals in each channel pair (x and y in Eq.3.3). Cross power spectral densities were computed by $S_{xy}(w) = \int_{-\infty}^{+\infty} R_{xy}(t)e^{jwt}dt$ where $R_{xy}(t)$ is the cross-correlation between channel x and y. Coherence measures were calculated for each window (Rb, Ro and Rd*). Coherences were plotted as a function of stimulus amplitude for different stimulus frequencies.

$$C_{xy}(w) = \frac{|S_{xy}(w)|^2}{S_{xx}(w)S_{yy}(w)} \tag{3.3}$$

3.4.3 Signal-to-noise Ratio

Electrode performances were compared by computing SNR individually for each channel. The calculation method was adopted from [106] where SNR for spontaneous LFP activity was calculated by dividing peak-to-peak amplitudes ($A_{peak-to-peak}$) to the standard deviation (U_{STD}) of the signal during the silent periods baseline. In our analysis ($A_{peak-to-peak}$) of the response within the Ro window was found and (U_{STD}) was computed from the Rb window (Eq.3.4). SNR values from all conditions were averaged (across amplitude and frequency for contralateral stimulation). Additionally, SNR values from operational channels were averaged to obtain the data for a given electrode type and subject. It is important to note that only trial averaged data with Ro RMS greater than Rb RMS were included for SNR analysis. Therefore, some conditions included in the statistical analysis for RMS and coherence measures were not used for the calculation of SNR due to low evoked activity.

$$SNR = \frac{A_{peak-to-peak}}{U_{STD}} \tag{3.4}$$

3.4.4 Statistical Analysis

SPSS Version 25 (IBM) was used for conducting the statistical analyses. Random intercept and random slope linear mixed effects models (LMMs) were implemented for statistically analyzing the RMS, coherence and SNR measures. For each measure two general model forms were established where LMM-1 analyzed the recorded data cumulatively by including electrode type as a fixed effect in the model and LMM-2 analyzed each electrode type separately with two models. Eq.3.5 describes the mathematical function of the used model in LMM-1 analysis, where betas are the regression coefficients E is the electrode type (fixed effect), S is the stimulation side (fixed effect), F is the stimulation frequency (fixed effect), λ is the stimulation amplitude (covariate), u_{i1} is the random intercept due to subjects i, u_{i2} is the random slope due to subject i and ξ_{ijklm} is the residual error.

$$y_{ijklm} = \beta_0 + \beta_1 E_j + \beta_2 S_k + \beta_3 F_l + \beta_4 \lambda_m + (interactions) + u_{i1} + u_{i2}\lambda_m + \xi_{ijklm} \tag{3.5}$$

The statistical analysis of coherence was done by investigating different frequency ranges (narrow-band and wide-band). Coherence values from the temporal windows (Rb, Ro, Rd*) were averaged within these bands for input to statistical analysis. In this case the time window was used as an additional fixed factor in Eq.3.5. Similar to above, coherence analysis was performed by including the electrode type as a fixed factor (LMM-3) and separately for each electrode type (LMM-4).

4. RESULTS

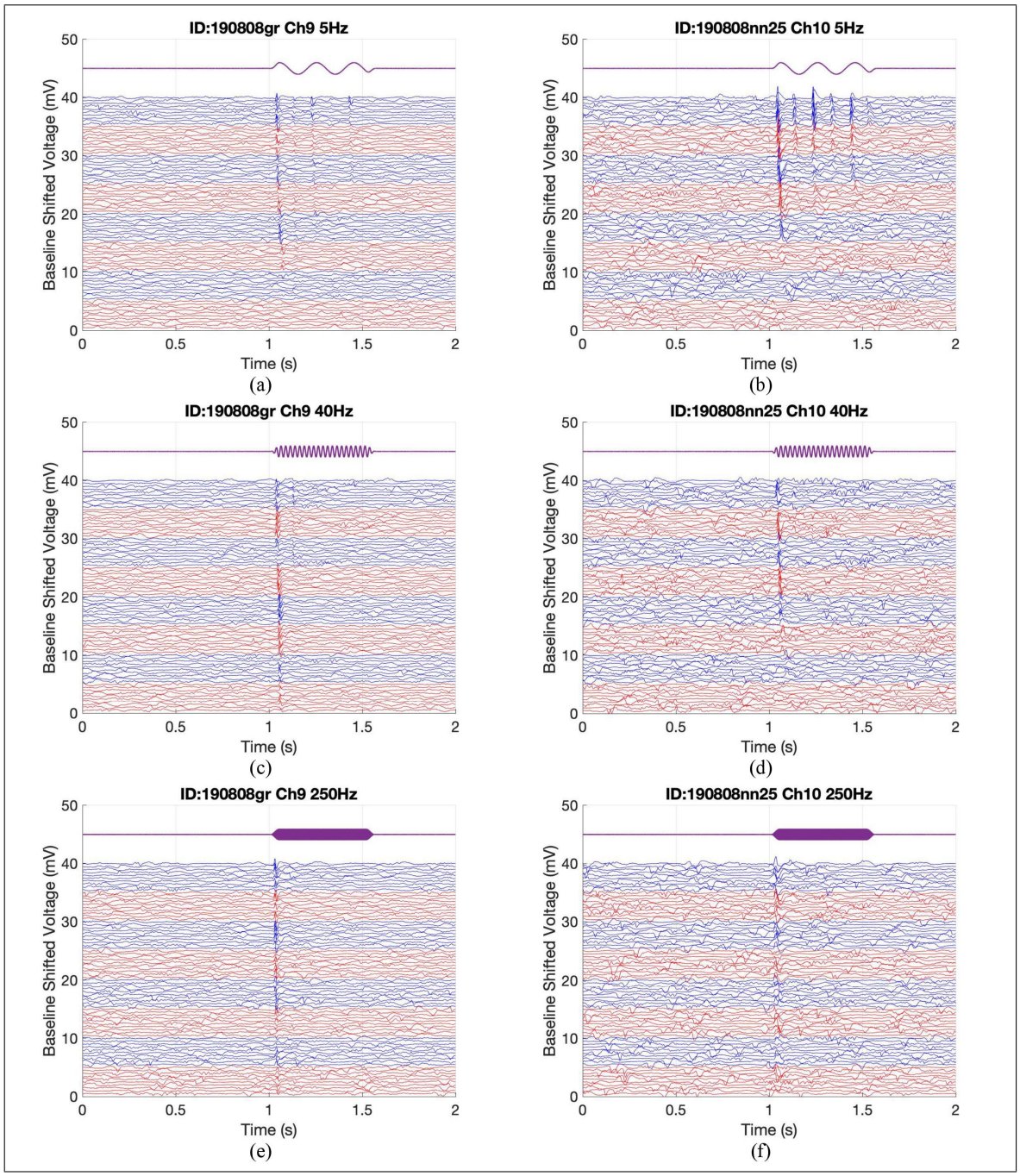

Figure 4.1 Trial-by-trial plots of surface LFPs from experiment 190808 (vibrotactile stimulation of the contralateral hindpaw. Each color group represents trials for a single attenuation level given on the right (19 - 270 μ). Traces recorded with gr#1-black from Ch-9 for (a) 5-Hz, (c) 40-Hz and (e) 250-Hz stimulation and corresponding recordings of the nn25#3 from Ch-10 (b,d,f) are shown. Ch-9 and ch-10 were matched since they exhibited the highest evoked response per electrode and correspond to the same position over cortex.

4.1 Qualitative Measures for the Recorded Traces

Collected data were initially investigated by visualization of the recorded traces which allowed studying their qualitative features. In each plot stimulation waveforms were given together with the recorded activity in order for showing the temporal synchronization between the onset of neural activity and stimulus delivery. However stimulation waveforms are plotted in arbitrary limits. As previously mentioned in the methods section data from trials between 15- to 0-dB were excluded from the statistical analysis because of mechanical decoupling; however, in the following section the full 35- to 0-dB range was chosen for plotting the trials to help the reader visualize the evoked response better.

4.1.1 Trial-by-trial Analysis

Ten trials for each attenuation level (35-0 dB) for 5-, 40- and 250-Hz frequencies were recorded, totaling 80 trials per frequency. Recorded trials were initially examined by plotting each trace with respect to time (see Figure 4.1). Evoked response onset time-lag due to stimulus delivery changed as a function of the stimulus amplitude in which the delay was shorter for higher amplitudes. Only 5-Hz stimulation exhibited frequency following response (i.e. entrainment) at high amplitudes. The threshold for evoked response decreased as the stimulus frequency increased. Variation in the background rhythms during an experiment were attributed to the anaesthetic state of the animal.

4.1.2 Trial-averaged Analysis

Trials that belonged to a certain stimulation frequency and amplitude were time averaged and LFPs from trials are plotted. Time averaging highlights the evoked response wwhich is time locked to the stimulus by averaging out background activity. Figure 4.2 shows average LFPs in response to contralateral and ipsilateral stimula-

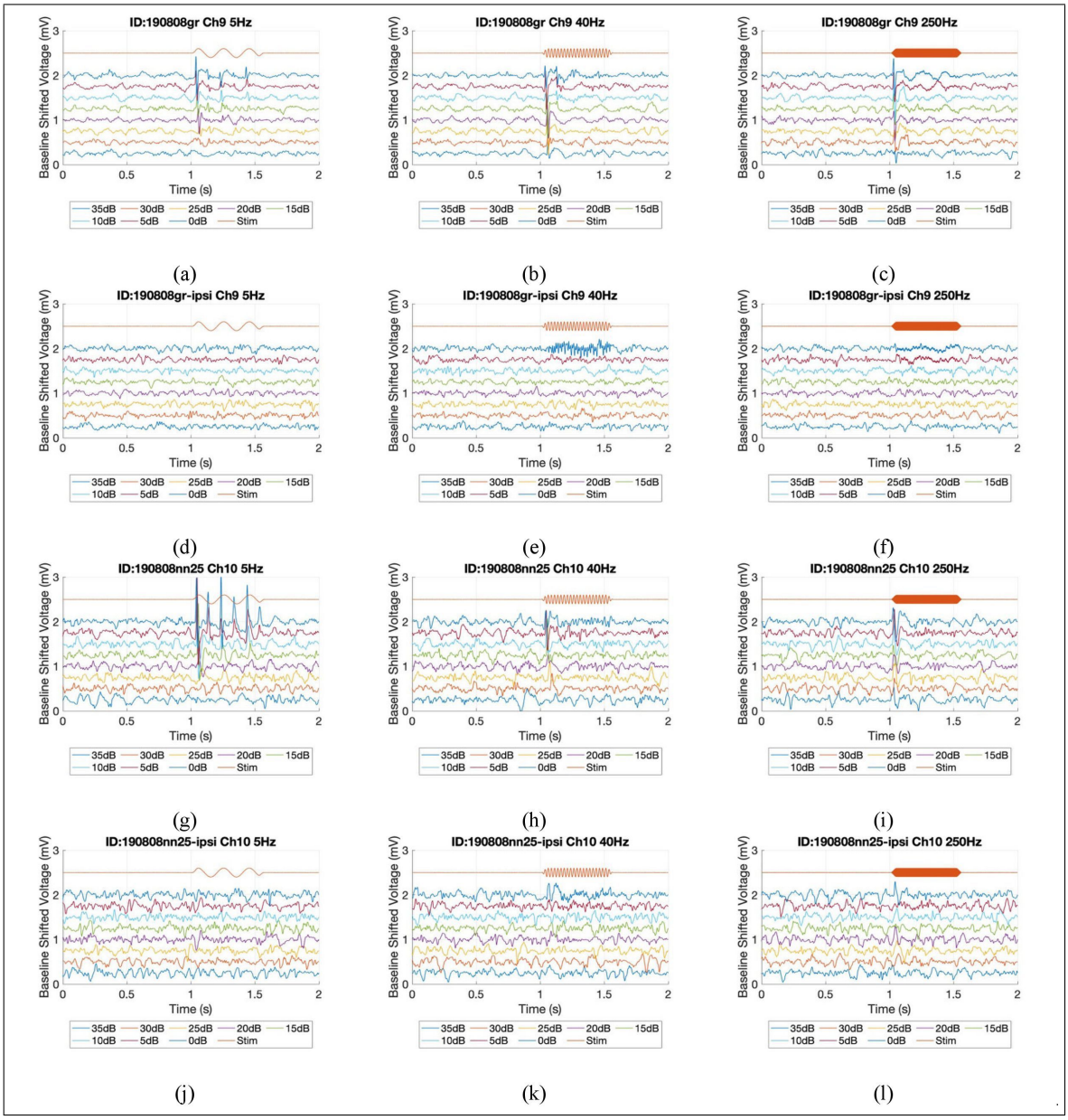

Figure 4.2 Time-averaged LFP plots from 190808. Vibrotactile stimulation of the contralateral hindpaw is shown in (a, b, c, g, h, i); stimulation of the ipsilateral hindpaw is given in (d, e, f, j, k, l) from GR- and NN25- arrays respectively. Especially for 40- and 250-Hz stimulation, noise components are visible in the higher stimulation amplitudes which also cause decoupling of the skin. Additionally, EMI from the shaker and electromechanical disturbances may cause such noise at very high driving amplitudes. Only data for 35 - 15 dB attenuation were included statistical analysis. It was shown by [109] that these vibrotactile displacements could be followed by the skin surface without distortion.

tion as recorded by the GR- and NN25-arrays. Previously mentioned relationship between the onset delay and stimulation amplitude is more evident in the trial averaged plots especially for 5- and 40-Hz stimulation. Higher evoked response amplitudes

were recorded with the NN25-arrays. As seen in Figure 4.2 ipsilateral stimulation did not usually cause evoked response, in some cases low level LFPs were observed inter-hemispheric information transfer. Observations similar to trial-by-trial analysis were made in trial-averaged data.

4.1.3 Wavelet Power Spectrum

Wavelet power spectrums were plotted (see Figure 4.3) by employing a Morlet wavelet for the transform formula. In general, power increase can be distinguished in two intersecting windows between 4 - 20 Hz and 20 - 150 Hz, where power densities were higher for the latter case. The results showing activation in gamma-band are consistent with the literature [48, 112, 46, 50, 113]. However, some of the cited work reported diminished power in the theta-band which do not agree with our results. Increased theta-band power was more prominent for 5-Hz stimulation. Higher power densities were observed for NN25-arrays.

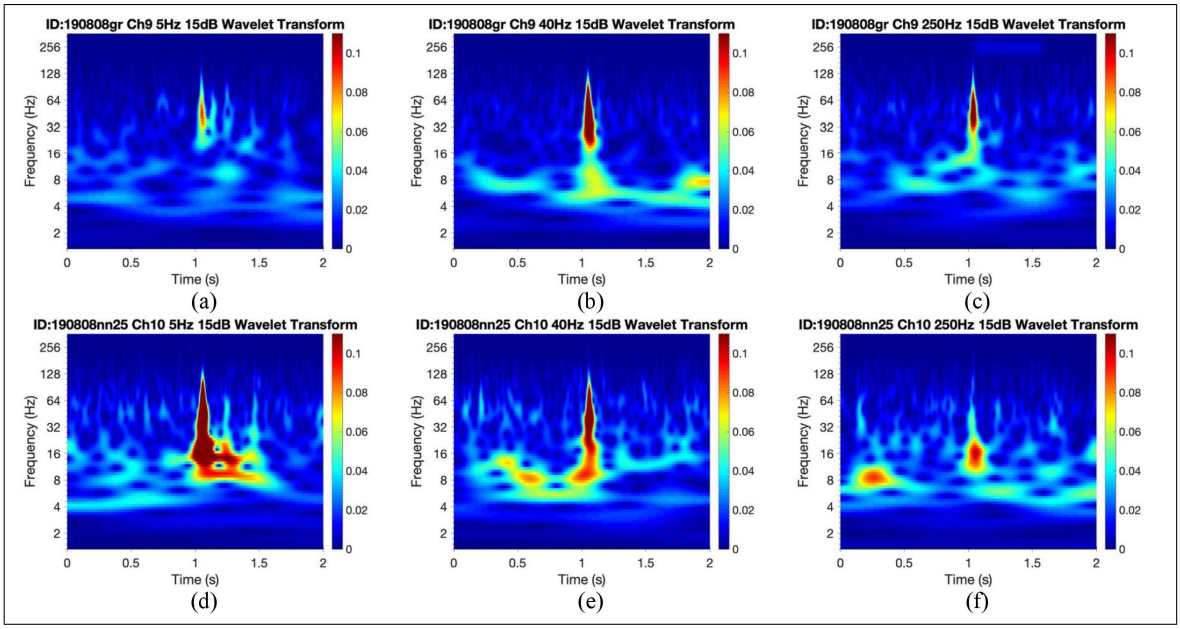

Figure 4.3 Wavelet power spectrum from 190808 are given for time-averaged 15-dB trials. Color code is for wavelet coefficient magnitude squared.

4.2 Root-mean-square Measures

Change in RMS levels due to cortical activation was investigated by subtracting the baseline activity from the activity in two different temporal windows that represents evoked activity. (Ro-Rb and Rd*-Rb). Electrode type (GR-electrode vs. NN25-electrode), stimulation frequency (5-, 40- and 250-Hz), stimulation side (contralateral vs ipsilateral) were selected as fixed factors and stimulus amplitude was deifned as the covariate in the statistical analysis. Dependent variables Ro-Rb and Rd*-Rb were examined on two different datasets (best-channels and all-channels) as explained in methods section.

RMS noise characteristics (extracted from Rb window) for the electrodes were calculated as 23.02±10.22-μV (GR all-channels), 37.29±15.56-μV (NN25 all-channels), 26.10±9.19-μV (GR best-channels) and 46.26±20.83-μV (NN25 all-channels). Where difference between averages for electrode types were significant for $p<0.001$ in both datasets.

4.2.1 Average Ro-Rb RMS

Average vibrotactile response differences between baseline and onset windows for the GR- and NN25-arrays were shown in Figure 4.4 with respect to the stimulus amplitude as measured by RMS voltage differences. For best-channels data, average Ro-Rb values were 15.51±26.30-μV (GR-contra), 0.98±11.74-μV (GR-ipsi), 47.01±52.85-μV (NN25-contra) and 8.82±48.14-μV (NN25-ipsi). For all-channels data RMS means decreased to 8.91±20.02-μV (GR-contra), -0.14V±8.72-μV (GR-ipsi), 26.28±32.16-μV (NN25-contra) and 4.77±27.25-μV (NN25-ipsi). An amplitude dependent increase in Ro-Rb was observed with both electrode types but for NN25-arrays the observed change was larger. Ipsilateral stimulation results from GR-arrays displayed a steady linear profile which did not correlate to the change in amplitude whereas for NN25-arrays correlation was preset. All-channels data illustrated matching amplitude dependent trends however the captured differences were smaller in comparison to the best-channels data.

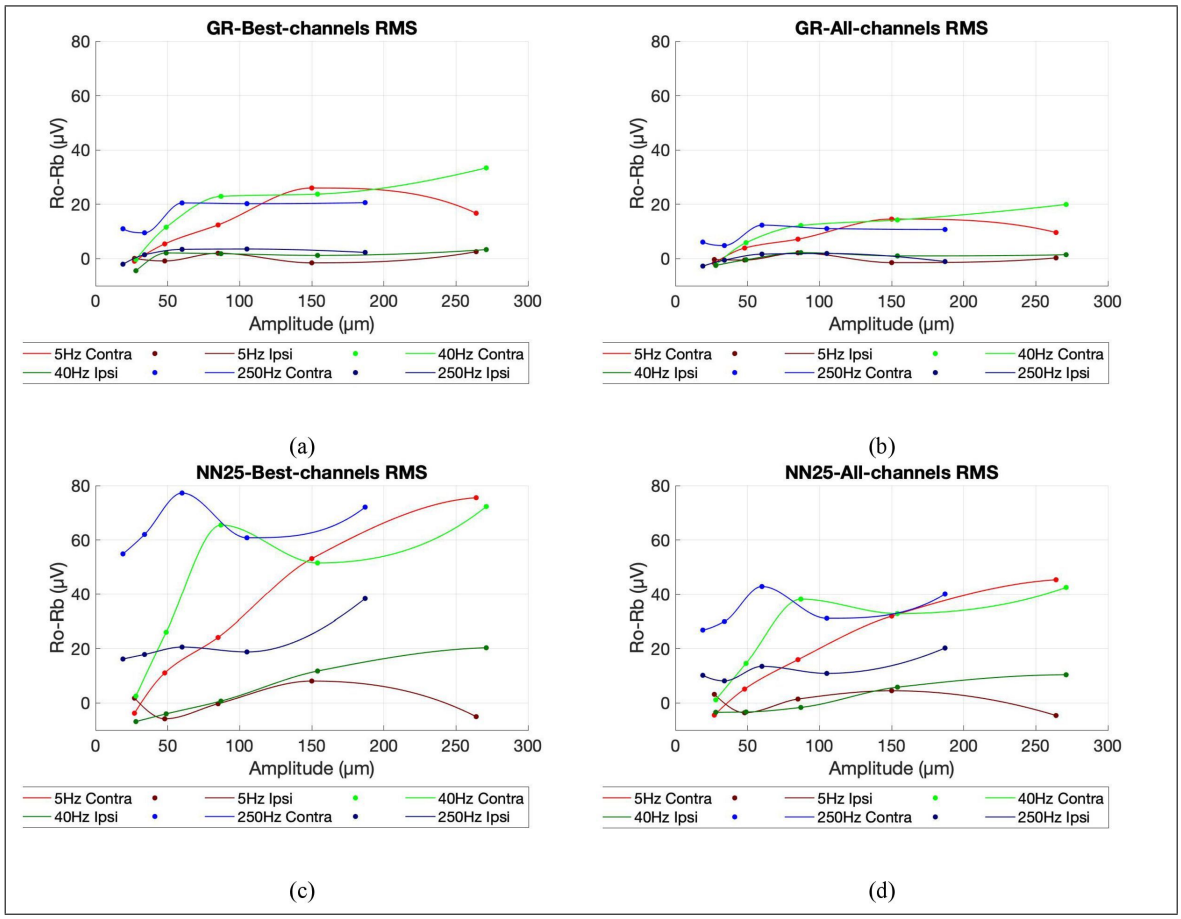

Figure 4.4 Average vibrotactile responses for Ro-Rb (LFP RMS measures) are given in the figure. Results are given for best-channels (a,c) and all-channels (b,d) data from the GR- and NN25-arrays respectively. Evoked response did not vary with the amplitude in ipsilateral graphene recordings, however for contralateral graphene and all cases of data from NN25-arrays, an amplitude dependent increase was observed.

Contralateral stimulation averages for GR and NN25-arrays were 8.91±20.02-μV and 26.28±32.16-μV.

LMM-1 analysis depicted that stimulation side (p=0.008), amplitude(p=0.021) and frequency (p=0.001) had significant main effects when investigated for all-channels and best-channels (p<0.001, p=0.022, p<0.001 respectively) datasets. The model estimates of averages with respect to stimulation frequencies were 28.01±4.19 (SEM), 15.15±4.12 (SEM), 9.98±4.11 (SEM) for 250-, 40-, 5-Hz best-channels and 14.85±2.47 (SEM), 8.41±2.42 (SEM), 5.91± 2.42 (SEM) for 250-, 40-, 5-Hz all-channels data. Post-hoc analysis revealed that 250-Hz produced a significantly higher average com-

pared to that of the remaining stimulation frequencies. Electrode type also had a main effect; this will be studied in more detail at a later section.

LMM-2 for best-channels data in which data from each electrode type were analyzed separately, revealed the following results. Stimulation side ($p=0.002$), frequency ($p<0.001$) and amplitude ($p=0.003$) had significant effects for the average RMS recorded from NN25-arrays whereas the stimulation side ($p=0.022$) was the only significant effect for the GR-arrays. Post-hoc tests for data from NN25-arrays uncovered that 250-Hz stimulation yielded significantly stronger evoked response compared to 40-Hz and 5-Hz trials. Interaction between stimulation side - amplitude ($p=0.005$) was a significant effect in GR-arrays. For NN25-arrays stimulation side - frequency ($p=0.011$) and side - amplitude ($p=0.028$) interactions were significant. All-channels data from LMM-2 did not show significance for any of the factors for GR-arrays whereas stimulation side ($p=0.025$), frequency ($p=0.001$) and amplitude ($p=0.019$) had significant main effects for NN25-arrays.

4.2.2 Average Rd*-Rb RMS

Activity profile for Rd*-Rb averages is given in Figure 4.5. Increase in RMS response as a function of stimulation amplitude was observed in a narrower voltage window compared to that of Ro-Rb. For best-channels data, average Rd*-Rb values were 2.16 ± 7.84-μV (GR-contra), 0.24 ± 6.91-μV (GR-ipsi), 7.00 ± 17.00-μV (NN25-contra) and 0.18 ± 11.75-μV (NN25-ipsi). Averaged data from GR-arrays across all amplitudes and stimulation conditions exhibited a flat trend whereas in NN25-arrays different patterns emerged. Contralateral 5-Hz stimulation produced larger responses in comparison to other frequencies for NN25-arrays, especially for the higher stimulation amplitudes.

LMM-1 analysis exhibited that stimulus amplitude was the only significant main effect on Rb-Rd* RMS both for best-channels ($p=0.018$) and all-channels ($p=0.006$) analysis. Electrode type and stimulation side interaction was found also significant for best-channels ($p<0.001$) and all-channels ($p<0.001$). Electrode type and amplitude

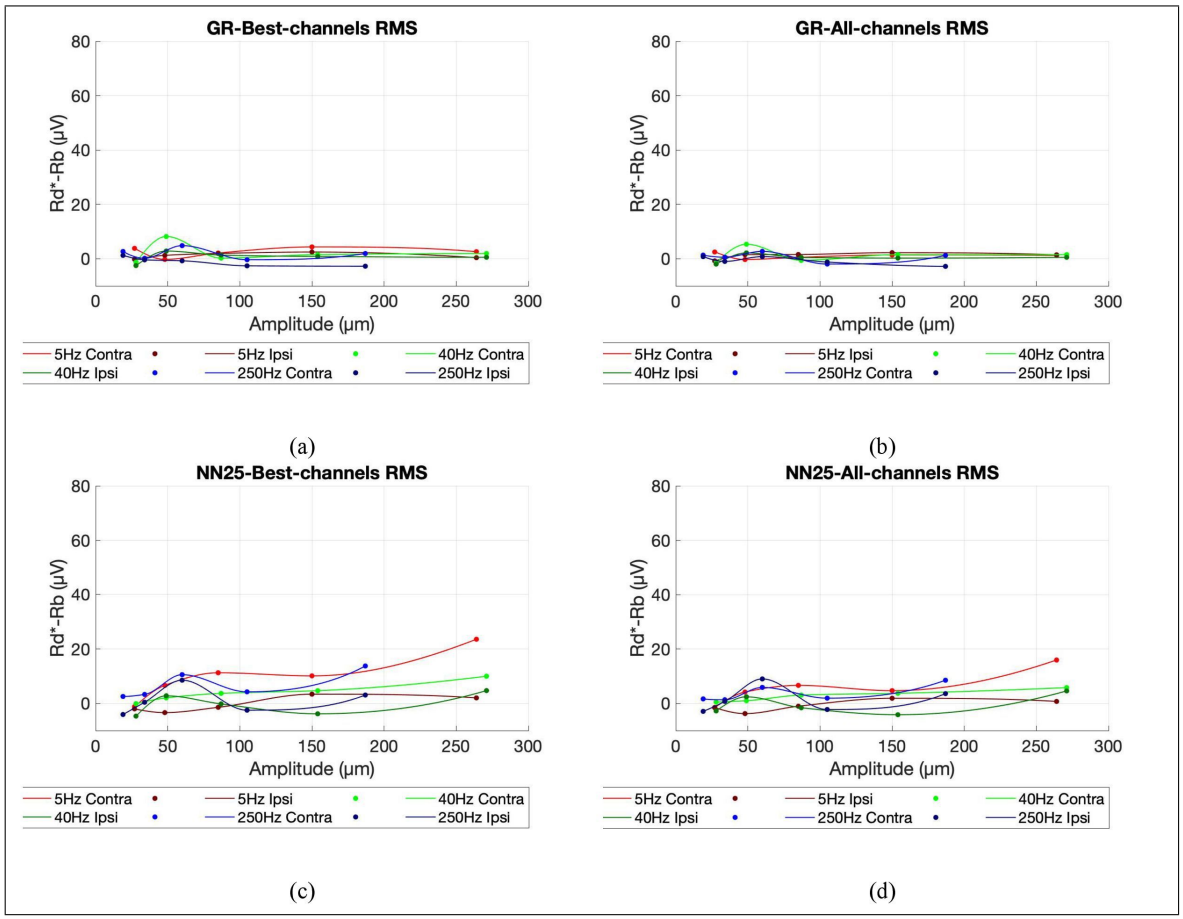

Figure 4.5 Average vibrotactile responses for Rd*-Rb (LFP RMS measures) are given in the figure. Results are given for best-channels (a,c) and all-channels (b,d) data from the GR- and NN25-arrays respectively. The Rd*-Rb window exhibited lower activation difference and especially for the graphene electrode the frequency or amplitude dependent response was observed to be flat.

interaction was significant only for best-channels data (p=0.045). LMM-2 analysis showed that stimulation amplitude was the only significant main effect for best-channels (p=0.02) and all-channels (p=0.001) data, selectively for the NN25-arrays. Interaction of stimulation side and amplitude for NN25-arrays were also a significant (p=0.044). However, analysis for GR-arrays did not display significance for any of the main effects or their interactions.

4.3 Spectral Coherence Measures

Neural signal synchrony between all channel pairs per electrode were investigated for the temporal windows of Rb, Ro and Rd*. Results from all investigated channel pairs were averaged for creating the coherence trends for the electrodes. Similar to the RMS analysis two different datasets were investigated which are the best-pairs and all-pairs datasets. Additionally, coherence behavior was analyzed within two different frequency ranges (narrow- and wide-band). The temporal windows were introduced as a fixed effect to the statistical model equation.

4.3.1 Narrow-band Coherence

The cross spectral synchrony among channels were investigated around the stimulation frequencies. This investigation helps showing if a frequency specific synchronization due to the stimulus existed in the signal. The frequency following response which was observed in the 5-Hz traces has proven that frequency information is indeed encoded in the cortex however for 40-Hz and 250-Hz stimulation such a response was not observed. Therefore, another possible encoding mechanism was examined by focusing on the signal synchrony around the stimulus frequency.

Best-pairs trends were clustered around $\approx$1 for both electrodes as shown in Figure 4.6. On the contrary plots for all-pairs data exhibit distinct patterns. Coherence mean per analysis window for contralateral trials were 0.84$\pm$0.05 (GR-Rb), 0.87$\pm$0.01 (GR-Ro), 0.84$\pm$0.03 (GR-Rd*), 0.88$\pm$0.03 (NN25-Rb), 0.82$\pm$0.01 (NN25-Ro) and 0.87$\pm$0.02 (NN25-Rd*). Ipsilateral coherence means were larger as given by 0.87$\pm$0.05 (GR-Rb), 0.9$\pm$0.01 (GR-Ro), 0.88$\pm$0.03 (GR-Rd*), 0.89$\pm$0.04 (NN25-Rb), 0.87$\pm$0.01 (NN25-Ro) and 0.87$\pm$0.02 (NN25-Rd*). In both electrodes, narrow-band coherence means decreased with respect to increasing stimulation frequency. Interestingly, for the GR-array 5-Hz stimulation coherences were distinctly higher for the Rb and Rd* windows as shown in Figure 4.6.g and .i. Amplitude dependence was not observed in the trends.

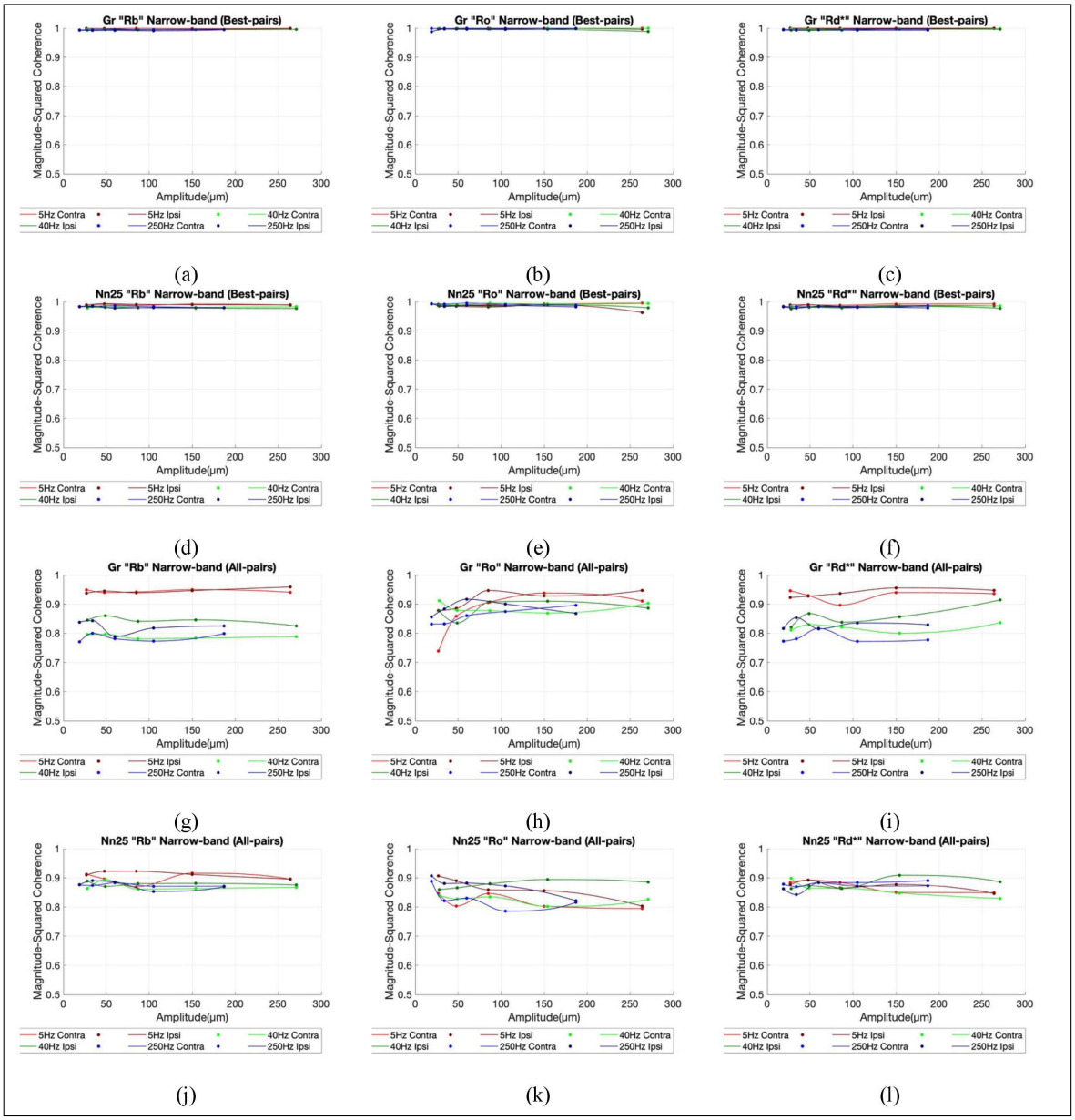

Figure 4.6 Narrow-band coherence trends from best-pairs data showed maximum possible synchrony for all analysis windows as given in (a, b, c) for GR-arrays and (d, e, f) for NN25-arrays. All-pairs coherences were lower for both arrays as shown in (g, h, i, j, k, l).

LMM-3 stimulation frequency (p=0.001) and temporal window (p<0.001) were the significant main effects for best-pairs data. Stimulation side and amplitude interaction was also found significant (p=0.021). According to all-pairs data only the stimulation frequency (p=0.001) was a significant main effect. For all-pairs the interactions between electrode type and stimulation amplitude (p=0.003) and stimulation side and temporal window (p=0.008) were significant. When analyzed seperately for different

electrode types by LMM-4 best-pairs for NN25-arrays showed that temporal window (p=0.001), stimulation frequency (p=0.018) were the significant main effects. Stimulation side and amplitude interaction was also significant (p=0.006) for NN25 best-pairs data. On the other hand, best-pairs data for GR-arrays exhibited significance for the main effects; temporal window (p=0.044), stimulation frequency (p<0.001), stimulation side (p=0.007). The only significant interaction was found between temporal window and frequency (p=0.026). All-pairs dataset analyzed by LMM-4 displayed that frequency (p=0.040) and stimulation side (p=0.031) were the significant main effects for NN25-arrays, and frequency (p=0.001) was the only significant main effect for GR-arrays.

4.3.2 Wide-band Coherence

Wide-band data shows the change in overall signal synchrony between the channels of the electrodes (see Figure 4.7). When inspected in the wide-band spectrum best-pairs data showed differential patterns in contrast to the narrow-band best-pairs results. Coherence means per temporal window for contralateral trials were 0.86±0.16 (GR-Rb), 0.91±0.10 (GR-Ro), 0.87±0.14 (GR-Rd*), 0.83±0.17 (NN25-Rb), 0.92±0.08 (NN25-Ro) and 0.85±0.15 (NN25-Rd*). Ipsilateral coherence means were very nearly identical as given by 0.87±0.15 (GR-Rb), 0.91±0.10 (GR-Ro), 0.88±0.14 (GR-Rd*), 0.83±0.17 (NN25-Rb), 0.88±0.12 (NN25-Ro) and 0.84±0.16 (NN25-Rd*). Rb coherence for all stimulation parameters were clustered around 0.87±0.16 for GR-arrays and 0.83±0.17 for NN25-arrays which were increased to 0.91±0.1 and 0.90±0.1 in Ro and decreased back to 0.88±0.14 and 0.85±0.16 in Rd*. Within the GR-arrays coherence trends for Ro and Rd* windows exhibited the highest activation in response to contralateral and ipsilateral 250-Hz stimulation.

All-pairs data exhibited lower coherence means. For contralateral trials coherence means per window were 0.55±0.26 (GR-Rb), 0.63±0.22 (GR-Ro), 0.56±0.24 (GR-Rd*), 0.71±0.25 (NN25-Rb), 0.77±0.14 (NN25-Ro) and 0.73±0.18 (NN25-Rd*). Ipsilateral coherence means were 0.60±0.25 (GR-Rb), 0.66±0.21 (GR-Ro), 0.61±0.25 (GR-

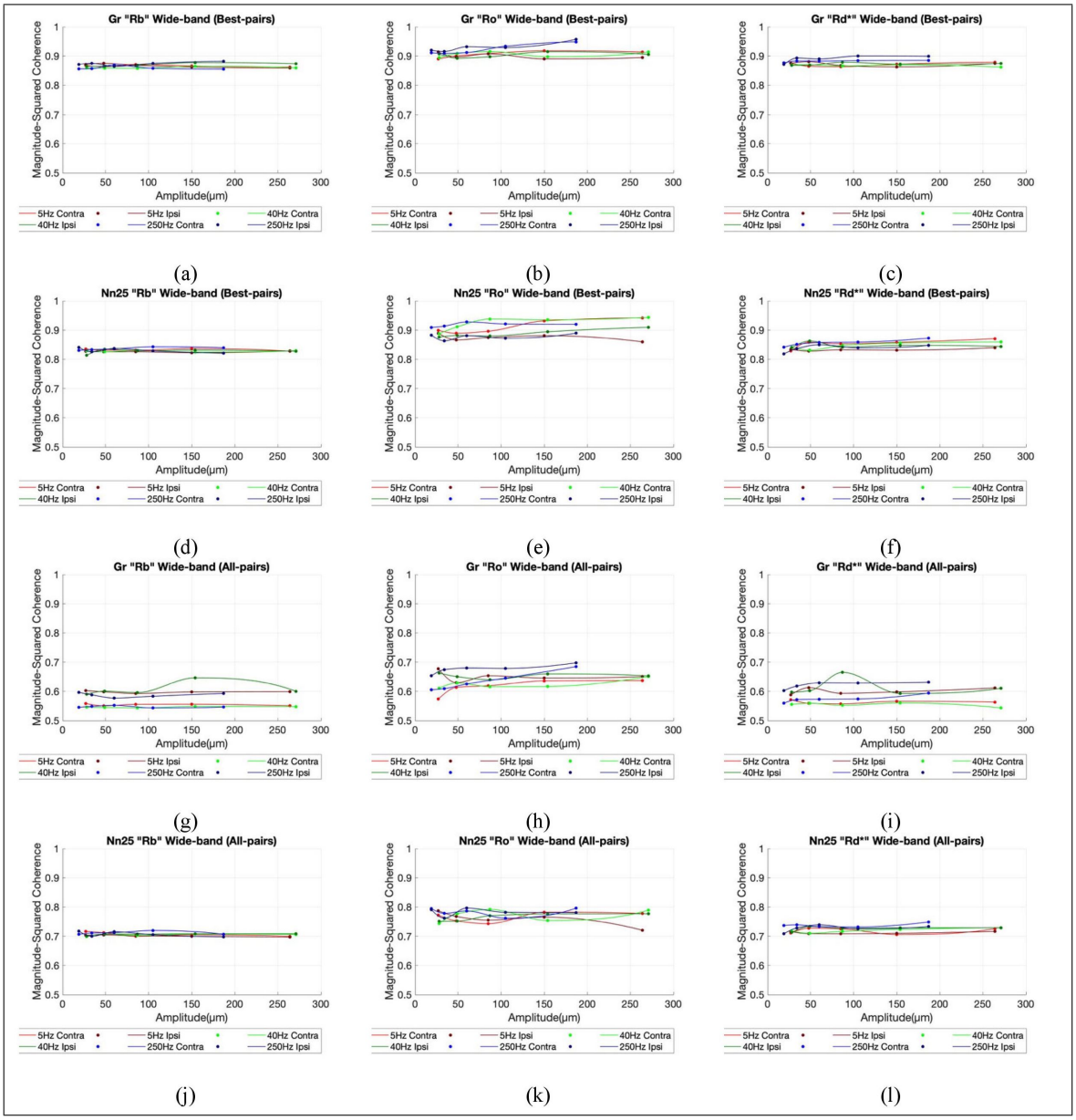

Figure 4.7 Wide-band coherence trends of best-pairs data for GR-arrays (a, b, c) and NN25-arrays (d, e, f) were depicted. Coherence means of best-pairs data for GR-arrays were higher in all conditions and 250-Hz stimulation produced the highest means. All-pairs trends are given for GR-arrays (g, h, i) and NN25-arrays (j, k, l); coherence means for NN25-arrays were higher.

Rd*), 0.71±0.2 (NN25-Rb), 0.77±0.15 (NN25-Ro) and 0.72±0.19 (NN25-Rd*). GR-array coherence means across all analysis windows for contralateral and ipsilateral trials were 0.58±0.24 and 0.62±0.24 respectively.

LMM-3 analysis for wide-band coherence revealed that temporal window ($p<0.001$) was a significant main effect for best-pairs dataset. For all-pairs dataset both temporal window ($p<0.001$) and stimulation side ($p=0.038$) were significant main effects. LMM-4 for best-pairs showed that both for GR-arrays and NN25-arrays coherence averages for temporal windows were significantly different ($p<0.001$). Post-hoc tests revealed that coherence averages for all three windows were significantly different from each other in both electrodes. Analysis from all-pairs dataset revealed that stimulation side ($p<0.001$) and temporal window ($p<0.001$) were significant main effects for GR-arrays. As previously mentioned, GR-arrays exhibited higher coherence averages for all-pairs dataset in the ipsilateral trials. NN25-arrays also displayed significance for coherences with respect to stimulation side ($p=0.034$) and temporal window ($p<0.001$). GR-arrays all-channels data exhibited significant interactions between temporal window and amplitude ($p=0.005$) and frequency and amplitude ($p=0.037$).

4.4 Electrical Stimulation of the Cortex

Electrical stimulation on the sensorimotor cortex (hindlimb representation) was performed in 7 different anaesthetized subjects by using the large diameter commercial Pt electrode (d:200-μm, NeuroNexus). Except for one experiment, electrical stimulation trials did not yield movement in the targeted muscle group. During experiment 181002 leg movement (muscle twitches) was observed in response to 0.8-mA bipolar stimulation train. In the remaining experiments stimulation between 0.5 - 1.5 mA resulted in twitches starting with the jaw and gradually moving to the head, upper trunk and abdomen areas as the current was increased. This was porbably due to current flowing over the tissue instead of activating motor circuits.

4.5 Functional Performance Comparisons for Electrodes

4.5.1 Qualitative Comparisons

In the previous sections, electrodes were individually examined with regards to measures that are commonly employed in neuroscience studies. Significant factors which effected the RMS and coherence values within spontaneous and evoked activity windows were determined. This section is aimed at providing performance comparisons between the GR- and NN25-arrays with respect to the previously shared measures as well as specifying trends and factors effecting the electrode SNR and SNR comparisons between electrodes. Additionally, impedance characteristics and SNR vs. impedance correlations were investigated.

Table 4.1
Estimated mean and standard error of each experimental condition found by the linear mixed effects model.

			Best-Channels		All-Channels	
Electrode	Type	Frequency	Mean	Std. Error	Mean	Std. Error
gr	Contra	250Hz	17.792	5.775	10.448	3.521
		40Hz	16.697	5.568	8.935	3.385
		5Hz	11.134	5.554	6.441	3.376
	Ipsi	250Hz	2.121	5.775	-.586	3.521
		40Hz	.523	5.568	-.031	3.385
		5Hz	.344	5.554	.143	3.376
nn25	Contra	250Hz	66.910	5.775	35.517	3.521
		40Hz	40.515	5.568	24.009	3.385
		5Hz	28.644	5.554	16.689	3.376
	Ipsi	250Hz	25.220	5.775	14.007	3.521
		40Hz	2.861	5.568	.736	3.385
		5Hz	-.198	5.554	.351	3.376

For the Ro-Rb RMS difference (LMM-1) from best-channels data, electrode type was a significant effect ($p=0.021$) where the estimated means form the model were calculated as 27.33 ± 3.95 (SEM) for NN25-arrays and 8.10 ± 3.95 (SEM). Interactions between electrode type - frequency ($p=0.001$) and type - amplitude ($p=0.005$) were also

found significant. Estimated means showed that NN25-arrays captured larger voltage differences especially for the contralateral stimulation group as given in Table 4.1. In all-channels data, electrode type was not a significant effect (p=0.056) however NN25-arrays still produced higher RMS means. Rd*-Rb difference yielded smaller means as expected for best- and all-channels data in both electrodes. Electrode type was not a significant effect in best-channels (p=0.123) or all-channels (p=0.115) for Rd*-Rb differences.

Coherence comparisons between electrodes were done separately with respect to best-pairs, all-pairs, narrow-band and wide-band categories. Best-pairs results from LMM-3 demonstrated that electrode type was a significant effect both for narrow- ($p<0.001$) and wide-band ($p<0.001$) groups where mean coherences for GR-array were given by 0.996 ± 0.001 (narrow-band) and 0.885 ± 0.133 (wide-band) which were larger in relation to NN25-arrays coherences 0.985 ± 0.003 (narrow-band) and 0.858 ± 0.142 (wide-band). Larger coherence trend exhibited by the GR-array was valid over all three analysis windows (Rb, Ro and Rd*), however electrode - window interaction was only significant for wide-band (p=0.022).

All-pairs data produced mixed results. Electrode type was a significant effect in narrow- ($p<0.001$) and wide-band ($p<0.001$). However, electrode type with the higher coherence changed depending on the analysis band. GR-arrays means were found to be 0.914 ± 0.109 (narrow-band) and 0.694 ± 0.139 (wide-band) whereas NN25-arrays means were 0.868 ± 0.081 (narrow-band) and 0.732 ± 0.075 (wide-band). This suggested that when all-pairs are investigated, NN25-arrays produced higher coherences in the wide-band spectrum however it has to be noted that 33,822 data-points for GR-arrays and 84,240 data-points for NN25-arrays were available in all-pairs coherence analysis. Overall, GR-arrays produced higher coherences.

Activation heatmaps of the cortex were created by averaging the RMS from Ro-Rb per channel. Inspections were done for every experiment individually and cumulatively by collapsing all collected data with respect to the cortical locus. The graphs were organized by taking the different channel arrangements of the electrode

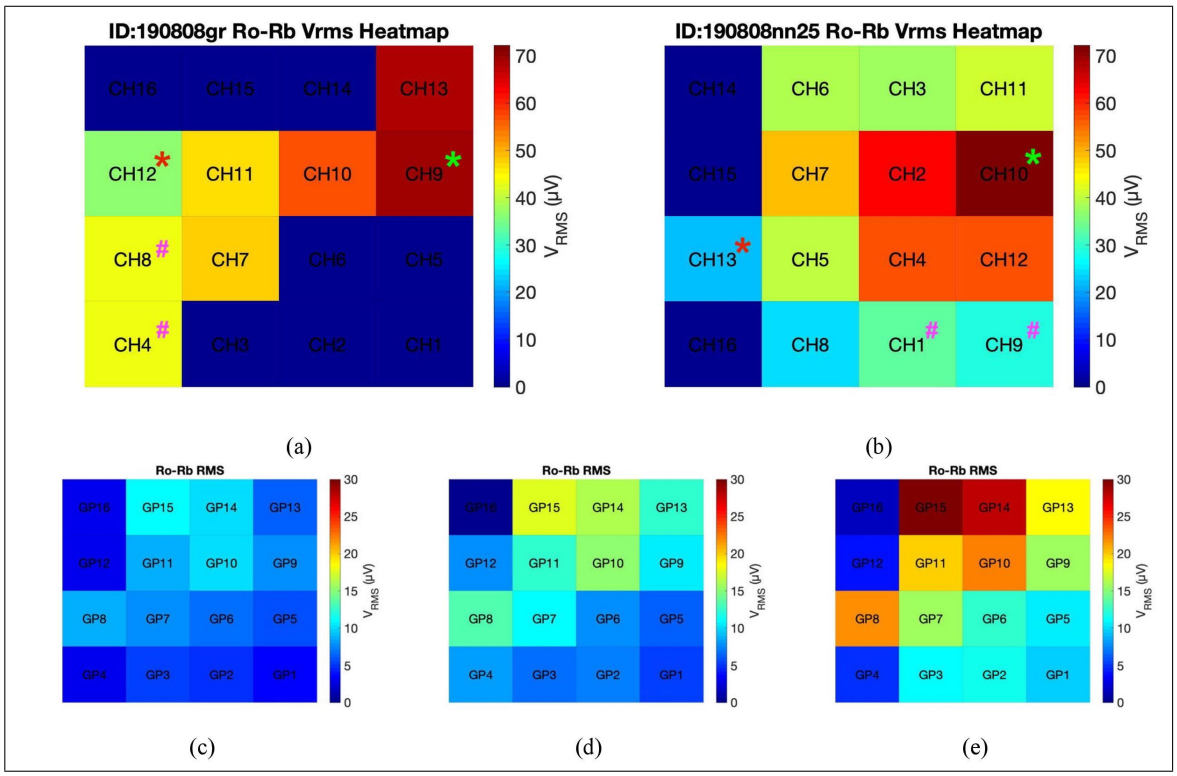

Figure 4.8 Ro-Rb RMS heatmaps from experiment 190808 were given for gr#1-black (a) and nn25#3 (b) arrays respectively. Channels with minimum RMS (red star) and maximum RMS (green star) and maximum wide-band coherence pairs (purple squares) are marked. Cortical activation heatmap computed by averaging all experiment results (all subjects, channels and both stimulation sides) for 5-Hz (c), 40-Hz (d) and 250-Hz (e) are shown.

arrays into account. In order for mitigating the variability caused by the different channels being in different locations between electrodes, a global position variable was defined, and the cumulative means were calculated according to the matched locations.

Coherence and RMS dynamics were investigated over the heatmaps as shown in Figure 4.8.and .b from experiment 190808. This revealed that channels which captured high RMS values did not necessarily belong to the pairs that exhibited high coherence. Aforementioned observation was valid for all experiments and electrode arrays. Figure 4.8.c, .d and .e illustrate the overall activation dynamics of the studied cortical area. Activation patterns were congruent in all stimulation frequencies however, evoked response amplitudes increased as the frequency was increased.

4.5.2 Impedance Measurements

Average impedance per array were given by 0.38±1-MΩ (gr#1-black), 0.80±1.44-MΩ (gr#1-green), 0.53±0.76-MΩ (gr#1-blue), 0.32±0.11-MΩ (nn25#1), 0.97±0.51-MΩ (nn25#2), 0.51±0.38-MΩ (nn25#3). Certain channels of the GR-arrays were categorized as bad channels by the manufacturer however, our impedance measurements did not always predict the bad channels. Recordability was a better measure for classifying the electrodes as bad or good however, even that did not always match the channels that were marked bad by the manufacturer.We categorized the channels as good, acceptable and bad depending on their recording performance during the experiments. Bad channels only showed large mains interference with no signal content, acceptable channels showed clear brain activity but also small electromagnetic interference (EMI) and good channels exhibited clear cortical activity without interference.

Gr#1-green could only be used once for recording and three impedance measurements were done. The channels of gr#1-green that were deemed bad by the manufacturer did not exactly match the channels observed as bad by our recording results and impedance measurements.

Gr#1-black revealed interesting patterns for channel performance during the 11 experiments it was employed for recording. Initially all of the channels belonging to gr#1-black were operational. However, during its second usage certain channels of the array were categorized as bad. In the following 5 experiments, those bad channels showed some brain activity together with EMI (thus categorized as acceptable), before completely turning bad again in the remaining 4 experiments. Therefore, it was concluded that channel degradation could be predicted by the increased EMI coupling in the channels. Except for the last experiment, impedance measurements from the black array did not predict the bad channels for recording. Furthermore, even in the last experiment, only 3 out of 5 bad channels exhibited very high impedances, and the rest had low impedances. Similar to the gr#1-green array, channels deemed bad by the manufacturer did not exactly match the bad channels for recording. Eventually, visual inspection of the array revealed mechanical failure of some tracks that run from

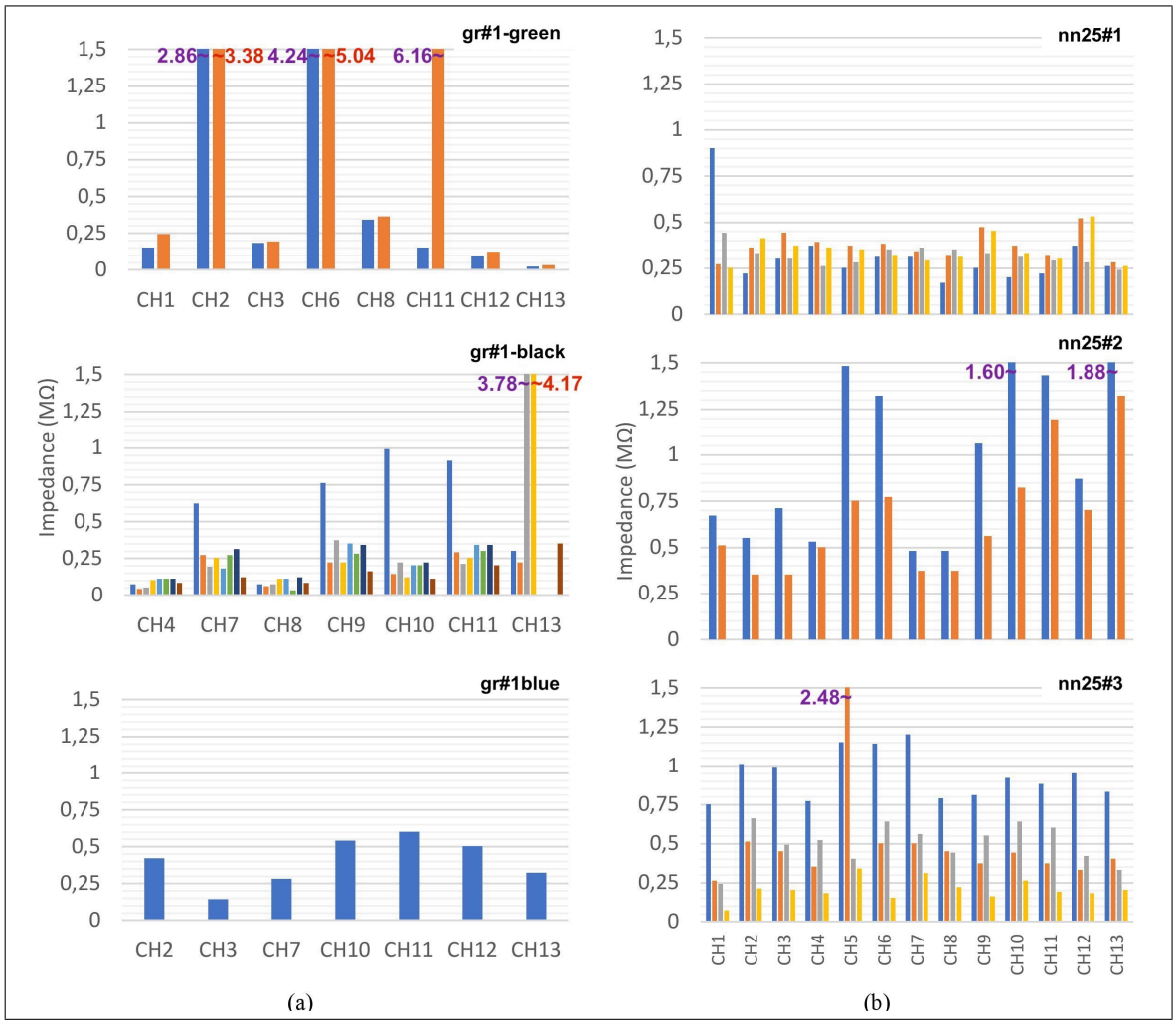

Figure 4.9 Impedance measurements for the GR- (a) and NN25-arrays (b). Each colored bar represents a separate measurement from indicated channels. Bad channels of the GR-arrays were not displayed.

the active electrode sites to the electrode PCB.

Interestingly, for the gr#1-blue array, bad channels marked by the manufacturer and the experimental results matched completely. However, impedance measurements still could not predict the channel status for recording. In other words, bad channels exhibited low impedances. Impedance measurements from channels that was available for recording are given in Figure 4.9. It is clear that the impedance values of the commercial NN25-arrays are more stable, and the research grade GR-arrays had large variance in the impedance values. The lowest impedance in GR-arrays was 0.02-MΩ

and 0.07-MΩ in NN25-arrays.

4.5.3 SNR Comparisons

SNR values of the two types of electrodes were examined by a method slightly modified from [106]. Only contralateral data which showed an evoked response were included in the analysis. Statistical analyses were performed on 745 averaged traces for GR-arrays and 1,447 averaged traces for NN25-arrays. SNR data were averaged across different channels for each electrode type and are given in Figure 4.10.a & b. for each subject.

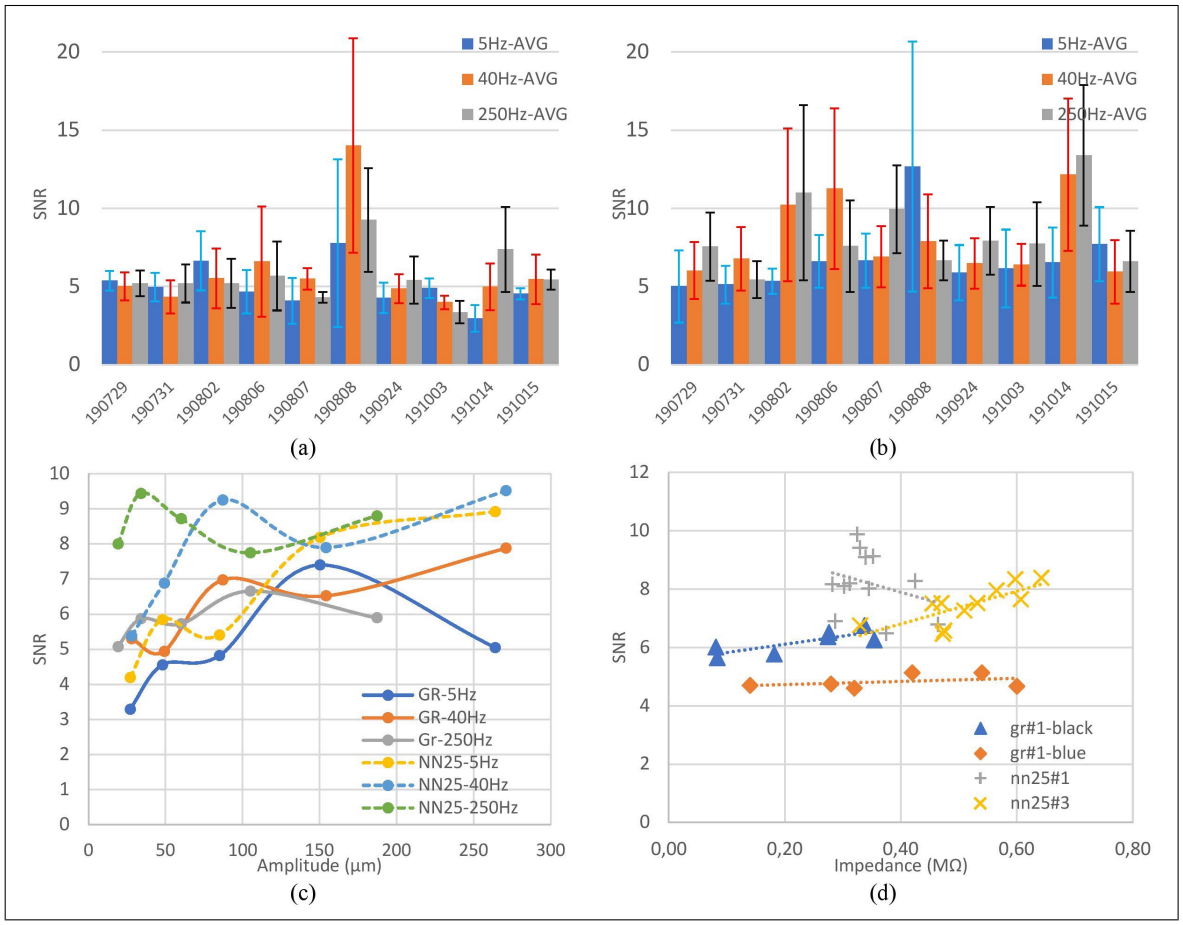

Figure 4.10 SNR levels across experiments with respect to the stimulation frequencies are given for GR- (a) and NN25-arrays (b). Amplitude dependence of SNR characteristics over different stimulation conditions are shown in (c). (d)SNR vs. impedance correlations averaged over subjects. Each data point represents an operational channel.

Average SNR values for all-channels GR- and NN25-arrays (pooled across amplitudes and frequencies) were calculated as 5.67±2.96 and 7.64±3.46 respectively. GR-array showed less variability across time in terms of SNR. Additionally, GR-arrays showed less variance within a given experiment. For different vibrotactile stimulation frequencies average SNR values were for 5.10±2.45 (5-Hz), 6.29±3.90 (40-Hz) and 5.61±2.19 (250-Hz) GR-arrays, and 6.63±3.40 (5-Hz), 7.83±3.67 (40-Hz) and 8.35±3.16 (250-Hz) for NN25-arrays. When examined for best-channels dataset SNR averages were 6.60±4.11 for GR-arrays and 9.78±5.04 for NN25-arrays. The difference between averages were found significant according to p=0.002.

Figure 4.10.c depicts SNR values as a function of vibrotactile stimulus amplitude at different stimulus frequencies for the two electrode types. LMM-1 for SNR where electrode type was included as a fixed effect in the model revealed that electrode type had a significant difference (p=0.021). LMM-2 revealed that stimulation frequency (p=0.004) and amplitude (p=0.015) had significant main effects on the NN25-arrays' SNR. Post hoc tests revealed 250-Hz stimulus yielded significantly higher SNR (p=0.02). For GR-arrays no such significant effects were observed.

Figure 4.10.d plots the SNR values against impedance values for different arrays. Each data point represents the average SNR and impedance for a different channel (averaged across experiments) per array. Only the channels which were operational throughout the experiments were given. Two outlier data-points with very high impedances (one for gr#1-black array and one for nn25#3 array) were omitted. According to Pearson's correlation SNR and impedance values for gr#1-black (p=0.030, r=0.803) and nn25#3 (p=0.006, r=0.7614) arrays were correlated.

5. DISCUSSION

Functional characterization of research grade graphene based thin-film microelectrodes were performed by recording somatosensory evoked LFPs from the cortical surface. Performance comparisons were made against commercially available Pt-Ir arrays. Active site dimensions were identical in both electrode types. Evoked activity from the hindlimb representation of the rat SI cortex were recorded by stimulation of the mechanoreceptors of the glabrous skin for the following reasons. Firstly, it was shown that mechanoreceptors of the human and rat skin are identical [2, 114] which creates a possibility of direct translation of the results from rat studies to human neuroprosthetics research. Secondly, evoked potential recordings from the representation of the limb areas in rat SI cortex are scarce, as studied by [65, 66, 24] in the form of spikes. LFP recordings in response to whisker stimulation (either electrical [102] or mechanical [106] or drug induced epileptic activity [95, 106] also exist in the literature additionally, decoding motor intensions from LFPs were shown to be possible [52, 53, 54]. Keeping in mind that we employed epidural electrodes which allow for a less-invasive surgical procedure that reduces the tissue reaction and LFPs represent the population activity unlike spikes, the study investigated the LFP range. Furthermore, authors of [95] suggested that HNO_3 doped graphene illustrated significant 60-Hz noise reduction which is advantageous for studying LFPs. Current LFP data from the hindpaw representation of the rat SI cortex are novel for the literature.

5.1 General Overview

During the experiments, 3 different commercially available Pt-Ir electrodes (NN25-arrays) and a single research grade graphene electrode which was divided into 4 groups (GR-arrays) were employed where each group was treated as a separate electrode array. Both electrode types were able to record brain activity in a reliable manner, however somatosensory evoked potentials were very low in some recordings. This phenomenon was dependent on the subject but not the electrode type. In other words,

if one electrode type recorded low/high evoked activity in a certain experiment the other electrode low/high activity in most cases. This was attributed to the state of the cortical networks due to anaesthesia.

Overall, plots from individual trials displayed higher RMS levels for the NN25-arrays and this was also reflected in the averaged traces where 10 trials of each amplitude level were averaged. Transient behaviour was depicted in the time-averaged data where either a negative or positive polarity leading response was followed by the opposite counterpart. In some experiments, evoked activity was elicited by ipsilateral stimulus presentation however this was observed in an infrequent manner.

5.2 Somatosensory Processing

Stimulus properties such as frequency and amplitude are shown to be encoded in the spiking activity of cortical neurons by different studies. Pinto et al. [115] described that spike rates of the cortical neurons depended on the velocity of the whisker stimulation but not the stimulation amplitude. Similar results were reported by another study [116], where rapidly adapting (RA) neurons were shown to be sensitive to variation in velocity. However, it was also shared that total response magnitudes of slowly adapting (SA) fibres showed amplitude dependent increase. In a review article [117], authors have speculated that LFPs poorly reflect the magnitude of the synaptic inputs. These results suggest that varying stimulus amplitude does not affect the spike rates in single neurons [24].

Current study quantified the existence of evoked activity by computing RMS differences from Ro-Rb and Rd*-Rb. Ro-Rb displays the RMS change within the first 100-ms of the stimulus onset whereas the latter shows the event related activation for the remaining 400-ms of stimulus presentation. LMM-1 analysis revealed that vibrotactile stimulus amplitude is a significant main effect for the Ro-Rb RMS both for best-channels ($p=0.022$) and all-channels data ($p=0.021$). Stimulus amplitude was also significant for Rd*-Rb RMS when analysed for best-channels ($p=0.006$) and all-

channels (p=0.018) data. In light of these results, we conclude that the stimulus amplitude is indeed encoded by a population of neurons in the form of LFPs which is consistent with the literature.

[118] reported that neuronal firing rate of a population of neurons vary as a product of frequency and amplitude, however they did not detect frequency following response (entrainment) for any of the employed stimulation frequencies (19-, 30-, 50-, 81-, 131-, 211- and 341-Hz). Phase-locking in the rat barrel cortex was investigated by focusing on the frequency range between 1- to 15-Hz with a mechanical stimulus delivered to the vibrissae [119]. It was reported that entrainment was strongest around 10-Hz stimulation and this behaviour was explained by the natural whisking frequency of rodents being close to 10-Hz. In their work [120], authors investigated the entrainment of the RA neurons of the monkey SI cortex and their afferents in response to a vibrotactile stimulus delivered to the hand for the given frequencies (6-, 12-, 25-, 50-, 100-, 150-, and 200-Hz). For the cortical neurons, entrainment was highest for 12-Hz stimulation whereas for the afferents 1-to-1 entrainment was reported for all frequencies. Entrainment data from different cortical structures are also available. Spike data from auditory cortex of squirrel monkey showed discernible entrainment up to 2.5-kHz [121]. In their study [122], authors studied phase-locking in the cat auditory cortex and shared that distinct units exhibit phase-locking for different frequency intervals.

Here we report that signal RMS was significantly altered by the stimulation frequency as shown by the results from LMM-1 analysis for Ro-Rb best-channels ($p<0.001$) and all-channels datasets (p=0.001). Post-hoc analysis exhibited that 250-Hz stimulation yielded significantly higher RMS averages compared to that of 5- and 40-Hz stimulation both for best-channels and all-channels data. These results advocate that stimulus frequency might be represented by the LFPs from a population of cortical neurons. Furthermore, existence of entrainment behaviour was observed selectively for 5-Hz stimulation which was depicted in the time-averaged and single-trial plots. In contrast to that of Ro-Rb, the LMM-1 results for Rd*-Rb showed highest averages in response to 5-Hz stimulation both for all-channels and best-channels data in recordings with both electrodes. Although the difference was not found significant, higher averages

for 5-Hz can be taken as a quantitative evidence for the existence of entrainment. It is important to note that partial entrainment (some cycles within the stimulus duration) was observed during investigation of certain trials with 40-Hz stimulation, however it was not a common for all trials or experiments.

Previous studies have reported different activation windows in the power spectrum for evoked cortical activity. LFP power bands of activation that were correlated to spiking behaviour were given as (25 - 90 Hz) [46], above 80-Hz [47], (35 - 90 Hz) [48], (1 - 8 Hz) and (60 - 100 Hz) [49], (≈60 - 200 Hz) [50]. Montemurro et al. [51] reported increased activity in (40 - 90 Hz) and decreased activity in (1 - 10 Hz) in the LFP signal that were correlated with increased neuronal firing rates. On another note, authors reported power peaks around 0.8-Hz , 40-Hz and 90-Hz frequencies for a graphene electrode study which recorded somatosensory evoked potentials from the cortex [102]. Our observations from the time-frequency analyses are congruent with the literature. Although statistical analysis were not applied on these data, commonly observed properties of the power spectrums were shared as follows. Entrainment effects were detected selectively for 5-Hz stimulation, as illustrated by a cyclic increase in spike like shapes in the power spectrum plots, synchronized to the vibrotactile stimulus delivery. Power components of activation were noted to be focused between 4- to 8-Hz, 8- to 16-Hz, 32- to 130-Hz bands for 5-Hz stimulation however in some cases discrimination between these bands became less definite. For 40- and 250-Hz vibrotactile stimulation activation was focused between 8- to 130-Hz in a single window. As a general comment we observed activation in the gamma and high-gamma bands which was synchronized to the vibrotactile-stimulus delivery therefore we deduced that this activation represents the sensory input received by the cortex.

Lastly, the observed polarity changes in the leading phase of the evoked response as depicted by time-averaged traces, could be due to the extracellular current dynamics. As previously mentioned LFP sources are widely modelled as current dipoles. Our technique recorded extracellular voltage fluctuations due to these currents and the negative or positive leading behaviour is determined by dominance of the source or sink components of local dipoles which is dictated by factors such as 3D arrangement

of the neurons, subcellular distribution of synaptic currents [117].

5.3 Functional Performance of the Electrodes

The main goal of this study was to compare the performance graphene and Pt-Ir electrodes by using techniques which are common in electrophysiology studies. Electrochemical characterization of the electrodes was not realized since it was out of scope of this study. While conducting performance comparisons, RMS, coherence, impedance and SNR metrics were employed.

In recordings from both electrodes RMS averages for Ro-Rb were higher compared to that of Rd*-Rb. LMM-1 analysis on best-channels data showed that, NN25-arrays were able to capture significantly higher Ro-Rb averages. All-channels data exhibited a similar tendency however the difference between averages was not significant. LMM-2 analysis of both all-channels and best-channels data from NN25-arrays, showed that stimulation side, frequency and amplitude were the significant effects on Ro-Rb averages. On the other hand, LMM-2 analysis on best-channels data from GR-arrays showed that stimulation amplitude was a significant main effect which was not the displayed by the all-channels dataset. Additionally, NN25 recordings from ipsilateral trials exhibited activation which was seldom seen in the case of GR-arrays. As a result, it was deduced that previously mentioned stimulation frequency dependent LFP response was better detected by the NN25-arrays where LMM-2 revealed that the distinction for 250-Hz stimulation was only significant for NN25-arrays however, averages for GR-arrays did not exhibit significant difference among averages.

For the LMM-1 analysis of the Rd*-Rb the only significant effect on the RMS averages was stimulation amplitude, as depicted by both best-channels and all-channels data. Electrode type and stimulation side interactions was also found significant in both datasets. The Rd*-Rb averages were not significantly different between employed electrodes both for best-channels and all-channels datasets. Further analysis by LMM-2 revealed that effects of stimulation amplitude was only significant for the NN25-arrays.

Coherence analysis were performed on three temporal windows (Rb, Ro and Rd*) for narrow-band and wide-band ranges. Narrow-band analysis investigated the coherence dynamics within the proximity of each stimulation frequency. This was realized by employing separate frequency ranges for each stimulation frequency for analysis. Narrow-band coherences for best-pairs dataset exhibited very high coherence ($\approx$1) for all conditions and electrodes therefore was not deemed as a good candidate for comparing electrode performance. LMM-3 analysis revealed that narrow-band average coherences for GR-arrays were significantly higher compared to that of NN25-arrays both for all-pairs and best-pairs datasets. Furthermore, narrow-band all-pairs trends for GR-arrays displayed an interesting behaviour. For Rb and Rd* windows 5-Hz contralateral and ipsilateral stimulation conditions exhibited higher coherences compared to other stimulation frequencies whereas in Ro window the separation decreased due to delivery of the stimulus. The separation for 5-Hz trends might have arisen due to the way narrow-band ranges for stimulation frequencies was determined (see section 3.4.2). If this was the reason for the mentioned behaviour NN25-arrays should have exhibited the same trends, however they did not. This could be happening due to graphene's intrinsic properties since the baseline signal, extracted from Rb, shows better coherence when investigated around 5-Hz.

Wide-band coherences showed that for best-pairs dataset averages of GR-arrays were significantly higher compared to that of NN25-arrays however, the situation was reversed in all-pairs data where NN25 coherences were significantly higher. Best-pairs trends showed a stimulation frequency dependent discrimination for Ro and Rd* windows in both electrodes which were not found significant by statistical analysis. Stimulation side was a significant effect for NN25-arrays best-pairs dataset. All-pairs trends for GR-arrays showed higher coherence for ipsilateral stimulation in all analysis windows and contralateral versus ipsilateral coherence averages were found significantly different.

Impedance characteristics of the electrodes displayed variable results. The smallest impedance values were recorded by the measurements from GR-arrays though, the variability between channels were much larger than that of NN25-arrays. [102] reported

that 61 channel out of the 64-channel doped graphene electrode array (active site area: 250-μm x 250-μm) they employed exhibited impedance values between 2 - 8 kΩ. They reported impedance values at 637-Ω for an undoped (300-μm x 300-μm) and 637-Ω for doped (300-μm x 300-μm) sample. [95] measured the impedance of a 50-μm x 50-μm doped graphene array by 541-kΩ. [107] reported an average of 286.4$\pm$92.6-kΩ for the good channels of a graphene electrode array (active site diameter: 100-μm).Our results from the GR-arrays; 0.38$\pm$1-MΩ (gr#1-black), 0.80$\pm$1.44-MΩ (gr#1-green), 0.53$\pm$0.76-MΩ are comparable with the previously shared results from the literature; however, it is important to note that we measured impedances at 500-Hz while the work from literature uses 1-kHz as a standard. For NN25-arrays variability between the channels of an array was smaller whereas, the variability between different arrays were still large. A decreasing trend for NN25 impedances were observed in successive experiments. Also, recordability from GR-arrays deteriorated in successive experiments which was not always detected by impedance measurements.

SNR performance comparisons showed that average SNR for NN25-arrays were significantly larger compared to GR-arrays. [106] reported the SNR of graphene SG-FETs (active area: W=20-μm, L=15-μm) during biccuculine induced activity and spontaneous LFP activity as 62$\pm$5.8 9.85$\pm$0.67 respectively. Furthermore, [95] reported for the mean SNR for a 50 x 50-μm^2 doped graphene electrode as 40.8 during bicuculline induced activity. Our results found an average SNR of 5.67$\pm$2.96 for GR-arrays. Interestingly GR-arrays displayed less SNR variance during the experiments. Electrode impedance and SNR values were correlated however, SNR increased with the impedance which is counterintuitive.

Brain signals recorded by NN25-arrays captured larger RMS values, whereas coherence among array channels were better in most cases for the GR-arrays. Individual channel impedances showed the smallest values were obtained from GR-arrays however variability among channels were very large. SNR averages for NN25-arrays were larger compared to GR-arrays. Overall, comparisons between electrodes concluded that NN25-arrays were better in certain performance metrics nonetheless, GR-arrays were also capable of detecting neural signals which makes them a plausible option for

being used in neuroscience studies.

5.4 Graphene-specific Observations

Primary concern of this work was investigating the functionality of graphene based thin-film electrodes for neural activity detection. It was important to underline that the aforementioned electrode was a research-grade product whereas the comparison electrodes (NN25-arrays) were commercially available products. For example, it is known that a special coating on the active sites of the NN25-arrays were used for enhancing electrode performance which did not exist in graphene. Since all GR-arrays were physically located on the same electrode, they had to be placed over the cortex for every single experiment even though only a single group/array within the electrode was actively used for recording. Therefore, GR-arrays were subjected to more mechanical deterioration compared to the NN25-arrays. Also, it should be noted that employing a single electrode in recordings could mask the possible differences between electrode samples due to the manufacturing process. Therefore, the results of this thesis is provisional regarding the performance of graphene electrodes.

Mechanical and geometric properties of the graphene electrode caused certain difficulties during experiments. Initially, the large electrode area of the 64-channel electrode required larger craniotomy windows which was especially problematic when operating on physically smaller animals. Thickness of the polyimide substrate on which the electrode tracks and active sites sit was not enough to provide a rigid backbone for the arrays which made it hard to place over the cortex. It was observed that the electrode gets dislocated easily after placement due to the smallest vibrations caused by various factors during the experiment. Even dipping the electrode in fluid for cleaning purposes was not possible without an aiding object as a result of electrode failing to overcome the surface tension. Together with the lack of rigidity, longer track lengths facilitated unnecessary bending of the electrode which made placement and stabilization over the cortex harder compared to NN25-arrays. This is also problematic for the planned chronic implantation trials.

The size of the electrode PCBs was drastically different between the compared electrode types (see Figure 3.5). This difference mainly arises from the need of an adapter PCB that divides the 64-channel electrode into 4 groups for matching the GR-array dimensions to that of the NN25-arrays and for suitable connection to the pre-amplifier. Furthermore, during experiments it was observed that GR-arrays were more susceptible to EMI which might be caused by the exposed connections of the PCB. Additionally, EMI was a predictor of channel degradation in the GR-arrays which was not reflected by the impedance measurements. Interestingly, the bad channels marked by the manufacturer did not always match the channels deemed bad in our observations. Visual inspection of the GR-arrays revealed some of the bad channels were actually mechanically failed where broken tracks were detected.

Last but not least, before being used, an activation procedure was performed as part of the manufacturer recommendations for GR-arrays. Biphasic current pulses were applied to the active sites which were immersed in PBS solution. Due to being a research grade product, requirement of additional usage procedures and the shared issues might have hindered the performance of the graphene electrodes that was presented by this work, ultimately underestimating the full potential of the material however this thesis was successful in demonstrating the practical use of this type of electrode for neuroscience and neuroengineering.

5.5 Implications for Cortical Neuroprosthesis

Cortical neuroprostheses are the only option for providing rehabilitation to patients suffering from conditions such as spinal cord injuries, severe neuro-/myo-pathies, brainstem strokes and neurodegenerative diseases where tapping into the peripheral nervous system is not an option for alleviating the problem. Brain-electrode interfaces are one of the most important components of these implanted devices which allows bi-directional communication between the brain and implants. Recording signals from the brain allow extracting user intention whereas stimulation allows providing artificial sensory feedback for better motor control. In addition to the studies that employed

ICMS for inducing artificial sensation, stimulation of the cortex by using less invasive surface electrodes were realized [123, 124, 125, 126].

As well as recording potentials form the brain surface for decoding motor intensions, graphene electrodes are potentially a good candidate for providing artificial somatosensory feedback and also possibly inducing muscle contractions. [102] reported that stimulation of the motor cortex successfully created muscle contractions in the rat hindlimb using graphene surface electrodes. As part of our study we tried stimulation of the motor area with Pt-Ir electrodes that have larger active site sizes which allowed injection of larger currents while staying in the safety limits imposed by Shannon criteria [110]. However, we did not observe contractions in the targeted limb area and did not try stimulation with graphene electrodes since their contact sizes were much smaller that decreased the allowed injection limits. Nevertheless, further characterization is needed since graphene as a material allow better charge injection as reported by many studies [101, 102, 70, 107]. We plan to use chronically implanted graphene electrodes for providing artificial sensation by electrical microstimulation which only requires low current amplitudes.

Graphene-based surface electrodes pose an advantage in manufacturing neuroprosthesis for long term use in human patients. Due to its electrochemical properties, flexible nature and biocompatibility, graphene electrodes are a better candidate for being used as neural interfaces rather than the currently employed metal-based electrodes. Another important factor contributing to the longevity of implanted electrodes are their level of invasiveness during implantation. The problem with intracortical designs are that in acute trials they function well however in long-term usage, foreign body reaction degrades the signal quality generally leading to electrode failure [127, 128, 129]. Even if the electrode material exhibits good stability and biocompatibility the inflammatory response causes encapsulation of the electrode contacts, after about 2 weeks-time post-implantation, depriving their link to the neural substrates [130]. Our work showed that recording somatosensory evoked LFPs were possible with graphene-based surface electrodes however we did not yet investigate the possibility of employing these electrodes for inducing artificial sensation as previously explained.

Lower impedance characteristics of graphene electrodes were reported especially in the low frequency range [95, 102, 107]. The mentioned advantage provided by graphene was exploited for recording infra-slow activity by [108]. Congruent with the previous studies our results depicted that graphene electrodes indeed displayed lower impedance characteristics. On the contrary, the lower impedance characteristics was not reflected on the amplitudes for the recorded brain activity. Commercial grade Pt-Ir based electrodes allowed detection of signals with larger amplitudes. Some possible reasons for the observed behaviour was explained by the issues related to production of graphene and differences related to termination and adapters in the circuitry employed by these devices.

5.6 Future Work

This study realized acute recordings from the rat SI cortex for performing functional characterization of graphene surface electrodes which was a step taken towards building a closed-loop neuroprosthetic system powered by graphene technology. Valuable information regarding the usability of these electrodes were acquired by comparing their performance to commercially available Pt-Ir electrodes; however, limitations of this study are addressed followingly.

Since the study followed an acute methodology, subjects were anaesthetized during the recordings which indeed effected the investigated brain processing. As discussed earlier, blockage of the NMDA receptors due ketamine anaesthesia likely enhanced the SEP amplitudes [24]. Therefore, expanding this work by recording potentials on awake subjects would be of importance. For this purpose, a study that employs chronical implantation of these electrodes is required which would also allow investigation of electrode stability and longevity once in contact with neural tissue for prolonged durations. Additionally, chronic implantation would allow us to investigate the stimulation performance of graphene electrodes for inducing artificial somatosensation.

Followingly, it has to be underlined that the employed electrodes had certain differences with regards to their overall geometry and usability. We suspect that these differences might have concealed the true potential of graphene electrodes. The Pt-Ir electrodes were well-miniaturized commercial products that have completed their R&D cycle. Although it might not be possible to match all the different factors that provide an advantage for the Pt-Ir electrodes, properties such as electrode area dimensions, connector cable length and most importantly the electrical circuitry can be matched between electrodes. It was observed that GR-arrays were more susceptible to EMI which could be as a consequence of its large PCB adapters. Furthermore, during the study only one graphene electrode was employed. Noticing that electrode characteristics as impedance were drastically different even among the channels of the same array, it is considered that more homogeneous production process will likely generate more viable results.

Here we focused on LFPs for a number of reasons however recording just LFPs might not be enough for reaching our end-goal, the closed-loop prosthetic system. Although motor activity is widely believed to be encoded by the spiking of single neurons, Churchland et al. demonstrated presence of oscillatory components in population activity for a simple reaching task [131]. Belitski et al. suggested that neural correlates of low-frequency LPFs and spikes are independent in the visual system [49]. Montemurro et al. reported that when spikes were analysed relative to the phase of the 1 - 4 Hz LPFs, the information content of the signal increased by 54% in the visual cortex [51]. Therefore, synchronously recording somatosensory evoked spikes and LFPs by modifying our recording setup could yield better results for being used in motor control.

REFERENCES

1. Kandel, E. R., J. H. Schwartz, T. M. Jessell, D. o. B. Jessell, M. B. Thomas, S. Siegelbaum, and A. J. Hudspeth, *Principles of Neural Science*, Vol. 4, McGraw-hill New York, 2000.

2. Leem, J. W., W. D. Willis, and J. M. Chung, "Cutaneous sensory receptors in the rat foot," *Journal of Neurophysiology*, Vol. 69, no. 5, pp. 1684–1699, 1993.

3. Johansson, R. S., U. LandstroÂ¨m, and R. LundstroÂ¨m, "Responses of mechanoreceptive afferent units in the glabrous skin of the human hand to sinusoidal skin displacements," *Brain Research*, Vol. 244, no. 1, pp. 17–25, 1982.

4. Johnson, K. O., "The roles and functions of cutaneous mechanoreceptors," *Current Opinion in Neurobiology*, Vol. 11, no. 4, pp. 455–461, 2001.

5. Sanderson, K. J., W. Welker, and G. M. Shambes, "Reevaluation of motor cortex and of sensorimotor overlap in cerebral cortex of albino rats," *Brain Research*, Vol. 292, no. 2, pp. 251–260, 1984.

6. Kim, U., and F. F. Ebner, "Barrels and septa: separate circuits in rat barrel field cortex," *Journal of Comparative Neurology*, Vol. 408, no. 4, pp. 489–505, 1999.

7. Welker, C., "Microelectrode delineation of fine grain somatotopic organization of SmI cerebral neocortex in albino rat," *Brain Research*, Vol. 26, no. 2, pp. 259–275, 1971.

8. Chapin, J. K., and C.-S. Lin, "Mapping the body representation in the SI cortex of anesthetized and awake rats," *Journal of Comparative Neurology*, Vol. 229, pp. 199–213, oct 1984.

9. Fabri, M., and H. Burton, "Ipsilateral cortical connections of primary somatic sensory cortex in rats," *Journal of Comparative Neurology*, Vol. 311, no. 3, pp. 405–424, 1991.

10. Alloway, K. D., "Information processing streams in rodent barrel cortex: the differential functions of barrel and septal circuits," *Cerebral Cortex*, Vol. 18, no. 5, pp. 979–989, 2007.

11. Petersen, C. C. H., "The functional organization of the barrel cortex," *Neuron*, Vol. 56, no. 2, pp. 339–355, 2007.

12. Feldmeyer, D., M. Brecht, F. Helmchen, C. C. H. Petersen, J. F. A. Poulet, J. F. Staiger, H. J. Luhmann, and C. Schwarz, "Barrel cortex function," *Progress in Neurobiology*, Vol. 103, pp. 3–27, 2013.

13. Vincent, S. B., *The functions of the vibrissae in the behavior of the white rat...*, Vol. 1, University of Chicago, 1912.

14. Tahon, K., M. Wijnants, and E. De Schutter, "The RAT-ROTADRUM: A reaction time task depending on a continuous stream of tactile sensory information to the rat," *Journal of Neuroscience Methods*, Vol. 200, no. 2, pp. 153–163, 2011.

15. Harris, J. A., R. S. Petersen, and M. E. Diamond, "Distribution of tactile learning and its neural basis," *Proceedings of the National Academy of Sciences*, Vol. 96, pp. 7587 LP – 7591, jun 1999.

16. Prigg, T., D. Goldreich, G. E. Carvell, and D. J. Simons, "Texture discrimination and unit recordings in the rat whisker/barrel system," *Physiology & Behavior*, Vol. 77, no. 4, pp. 671–675, 2002.

17. Adibi, M., and E. Arabzadeh, "A Comparison of Neuronal and Behavioral Detection and Discrimination Performances in Rat Whisker System," *Journal of Neurophysiology*, Vol. 105, pp. 356–365, nov 2010.

18. Ghazanfar, A. A., C. R. Stambaugh, and M. A. L. Nicolelis, "Encoding of tactile stimulus location by somatosensory thalamocortical ensembles," *Journal of Neuroscience*, Vol. 20, no. 10, pp. 3761–3775, 2000.

19. Krupa, D. J., M. C. Wiest, M. G. Shuler, M. Laubach, and M. A. L. Nicolelis, "Layer-specific somatosensory cortical activation during active tactile discrimination," *Science*, Vol. 304, no. 5679, pp. 1989–1992, 2004.

20. Shuler, M. G., D. J. Krupa, and M. A. L. Nicolelis, "Bilateral integration of whisker information in the primary somatosensory cortex of rats," *Journal of Neuroscience*, Vol. 21, no. 14, pp. 5251–5261, 2001.

21. Shuler, M. G., D. J. Krupa, and M. A. L. Nicolelis, "Integration of bilateral whisker stimuli in rats: role of the whisker barrel cortices," *Cerebral Cortex*, Vol. 12, no. 1, pp. 86–97, 2002.

22. Tutunculer, B., G. Foffani, B. T. Himes, and K. A. Moxon, "Structure of the Excitatory Receptive Fields of Infragranular Forelimb Neurons in the Rat Primary Somatosensory Cortex Responding To Touch," *Cerebral Cortex*, Vol. 16, pp. 791–810, aug 2005.

23. Moxon, K. A., L. L. Hale, J. Aguilar, and G. Foffani, "Responses of infragranular neurons in the rat primary somatosensory cortex to forepaw and hindpaw tactile stimuli," *Neuroscience*, Vol. 156, no. 4, pp. 1083–1092, 2008.

24. Vardar, B., and B. Güçlü, "Non-NMDA receptor-mediated vibrotactile responses of neurons from the hindpaw representation in the rat SI cortex," *Somatosensory and Motor Research*, 2017.

25. Berger, H., "Über das Elektrenkephalogramm des Menschen," *Archiv für Psychiatrie und Nervenkrankheiten*, Vol. 87, pp. 527–570, dec 1929.

26. Schalk, G., and J. Mellinger, *Brain Sensors and Signals*, pp. 9–35. London: Springer London, 2010.

27. Schwartz, A. B., X. T. Cui, D. Weber, and D. W. Moran, "Brain-Controlled Interfaces: Movement Restoration with Neural Prosthetics," *Neuron*, Vol. 52, no. 1, pp. 205–220, 2006.

28. Quiroga, R. Q., and S. Panzeri, *Principles of Neural Coding*, CRC Press, 2013.

29. Elston, G. N., "4.13 - Specialization of the Neocortical Pyramidal Cell during Primate Evolution," pp. 191–242, Oxford: Academic Press, 2007.

30. Fabiani, M., G. Gratton, D. Karis, and E. Donchin, "Definition, identification, and reliability of measurement of the P300 component of the event-related brain potential," *Advances in Psychophysiology*, Vol. 2, no. S 1, p. 78, 1987.

31. Dal Seno, B., M. Matteucci, and L. Mainardi, "Online detection of P300 and error potentials in a BCI speller," *Computational Intelligence and Neuroscience*, Vol. 2010, p. 11, 2010.

32. De Vos, M., M. Kroesen, R. Emkes, and S. Debener, "P300 speller BCI with a mobile EEG system: comparison to a traditional amplifier," *Journal of Neural Engineering*, Vol. 11, no. 3, p. 36008, 2014.

33. Guan, C., M. Thulasidas, and J. Wu, "High performance P300 speller for brain-computer interface," in *IEEE International Workshop on Biomedical Circuits and Systems, 2004.*, pp. S3–5, IEEE, 2004.

34. Li, Y., J. Long, T. Yu, Z. Yu, C. Wang, H. Zhang, and C. Guan, "An EEG-based BCI system for 2-D cursor control by combining Mu/Beta rhythm and P300 potential," *IEEE Transactions on Biomedical Engineering*, Vol. 57, no. 10, pp. 2495–2505, 2010.

35. Mak, J. N., D. J. McFarland, T. M. Vaughan, L. M. McCane, P. Z. Tsui, D. J. Zeitlin, E. W. Sellers, and J. R. Wolpaw, "EEG correlates of P300-based brainâcomputer interface (BCI) performance in people with amyotrophic lateral sclerosis," *Journal of Neural Engineering*, Vol. 9, no. 2, p. 26014, 2012.

36. Pfurtscheller, G., C. Neuper, D. Flotzinger, and M. Pregenzer, "EEG-based discrimination between imagination of right and left hand movement," *Electroencephalography and Clinical Neurophysiology*, Vol. 103, no. 6, pp. 642–651, 1997.

37. Lauer, R. T., P. H. Peckham, and K. L. Kilgore, "EEG-based control of a hand grasp neuroprosthesis," *NeuroReport*, 1999.

38. Aurlien, H., I. O. Gjerde, J. H. Aarseth, G. Eldøen, B. Karlsen, H. Skeidsvoll, and N. E. Gilhus, "EEG background activity described by a large computerized database," *Clinical Neurophysiology*, Vol. 115, no. 3, pp. 665–673, 2004.

39. Almeida, A. N., V. Martinez, and W. Feindel, "The first case of invasive EEG monitoring for the surgical treatment of epilepsy: historical significance and context," *Epilepsia*, Vol. 46, no. 7, pp. 1082–1085, 2005.

40. Hill, N. J., T. N. Lal, M. Schroder, T. Hinterberger, B. Wilhelm, F. Nijboer, U. Mochty, G. Widman, C. Elger, and B. Scholkopf, "Classifying EEG and ECoG signals without subject training for fast BCI implementation: comparison of nonparalyzed and completely paralyzed subjects," *IEEE Transactions on Neural Systems and Rehabilitation Engineering*, Vol. 14, no. 2, pp. 183–186, 2006.

41. Leuthardt, E. C., G. Schalk, J. R. Wolpaw, J. G. Ojemann, and D. W. Moran, "A brainâcomputer interface using electrocorticographic signals in humans," *Journal of Neural Engineering*, Vol. 1, no. 2, pp. 63–71, 2004.

42. Wilson, J. A., E. A. Felton, P. C. Garell, G. Schalk, and J. C. Williams, "ECoG factors underlying multimodal control of a brain-computer interface," *IEEE Transactions on Neural Systems and Rehabilitation Engineering*, Vol. 14, no. 2, pp. 246–250, 2006.

43. Kamondi, A., L. Acsády, X.-J. Wang, and G. Buzsáki, "Theta oscillations in somata and dendrites of hippocampal pyramidal cells in vivo: Activity-dependent phase-precession of action potentials," *Hippocampus*, Vol. 8, pp. 244–261, jan 1998.

44. Buzsáki, G., "Theta Oscillations in the Hippocampus," *Neuron*, Vol. 33, no. 3, pp. 325–340, 2002.

45. Trevelyan, A. J., "The Direct Relationship between Inhibitory Currents and Local Field Potentials," *The Journal of Neuroscience*, Vol. 29, pp. 15299 LP – 15307, dec 2009.

46. Pesaran, B., J. S. Pezaris, M. Sahani, P. P. Mitra, and R. A. Andersen, "Temporal structure in neuronal activity during working memory in macaque parietal cortex," *Nature Neuroscience*, Vol. 5, no. 8, pp. 805–811, 2002.

47. Ray, S., and J. H. R. Maunsell, "Different Origins of Gamma Rhythm and High-Gamma Activity in Macaque Visual Cortex," *PLOS Biology*, Vol. 9, p. e1000610, apr 2011.

48. Fries, P., J. H. Reynolds, A. E. Rorie, and R. Desimone, "Modulation of Oscillatory Neuronal Synchronization by Selective Visual Attention," *Science*, Vol. 291, pp. 1560 LP – 1563, feb 2001.

49. Belitski, A., A. Gretton, C. Magri, Y. Murayama, M. A. Montemurro, N. K. Logothetis, and S. Panzeri, "Low-frequency local field potentials and spikes in primary visual cortex convey independent visual information," *Journal of Neuroscience*, Vol. 28, no. 22, pp. 5696–5709, 2008.

50. Ray, S., N. E. Crone, E. Niebur, P. J. Franaszczuk, and S. S. Hsiao, "Neural correlates of high-gamma oscillations (60-200 Hz) in macaque local field potentials and their potential implications in electrocorticography.," *The Journal of Neuroscience : The Official Journal of the Society for Neuroscience*, 2008.

51. Montemurro, M. A., M. J. Rasch, Y. Murayama, N. K. Logothetis, and S. Panzeri, "Phase-of-Firing Coding of Natural Visual Stimuli in Primary Visual Cortex," *Current Biology*, Vol. 18, no. 5, pp. 375–380, 2008.

52. Rickert, J., S. C. de Oliveira, E. Vaadia, A. Aertsen, S. Rotter, and C. Mehring, "Encoding of Movement Direction in Different Frequency Ranges of Motor Cortical Local Field Potentials," *The Journal of Neuroscience*, Vol. 25, pp. 8815 LP – 8824, sep 2005.

53. Ranade, G. V., K. Ganguly, and J. Carmena, "LFP beta power predicts cursor stationarity in BMI task," in *2009 4th International IEEE/EMBS Conference on Neural Engineering*, pp. 482–485, 2009.

54. Riehle, A., S. Wirtssohn, S. Gruen, and T. Brochier, "Mapping the spatio-temporal structure of motor cortical LFP and spiking activities during reach-to-grasp movements ," 2013.

55. Stavisky, S. D., J. C. Kao, P. Nuyujukian, S. I. Ryu, and K. V. Shenoy, "A high performing brainâmachine interface driven by low-frequency local field potentials alone and together with spikes," *Journal of Neural Engineering*, Vol. 12, no. 3, p. 36009, 2015.

56. Nardone, R., Y. Höller, S. Leis, P. Höller, N. Thon, A. Thomschewski, S. Golaszewski, F. Brigo, and E. Trinka, "Invasive and non-invasive brain stimulation for treatment of neuropathic pain in patients with spinal cord injury: a review," *The Journal of Spinal Cord Medicine*, Vol. 37, pp. 19–31, jan 2014.

57. Mayberg, H. S., A. M. Lozano, V. Voon, H. E. McNeely, D. Seminowicz, C. Hamani, J. M. Schwalb, and S. H. Kennedy, "Deep Brain Stimulation for Treatment-Resistant Depression," *Neuron*, Vol. 45, no. 5, pp. 651–660, 2005.

58. Machado, A., A. R. Rezai, B. H. Kopell, R. E. Gross, A. D. Sharan, and A. Benabid, "Deep brain stimulation for Parkinson's disease: surgical technique and perioperative management," *Movement Disorders: Official Journal of the Movement Disorder Society*, Vol. 21, no. S14, pp. S247–S258, 2006.

59. Clark, G., "Cochlear Implants BT - Speech Processing in the Auditory System," pp. 422–462, New York, NY: Springer New York, 2004.

60. Guenther, T., N. H. Lovell, and G. J. Suaning, "Bionic vision: system architectures â a review," *Expert Review of Medical Devices*, Vol. 9, pp. 33–48, jan 2012.

61. Dhillon, G. S., and K. W. Horch, "Direct neural sensory feedback and control of a prosthetic arm," *IEEE Transactions on Neural Systems and Rehabilitation Engineering*, Vol. 13, no. 4, pp. 468–472, 2005.

62. Vallbo, A. B., "Sensations evoked from the glabrous skin of the human hand by electrical stimulation of unitary mechanosensitive afferents," *Brain Res*, Vol. 215, no. 1-2, pp. 359–363, 1981.

63. Romo, R., A. Hernández, A. Zainos, and E. Salinas, "Somatosensory discrimination based on cortical microstimulation," *Nature*, Vol. 392, no. 6674, pp. 387–390, 1998.

64. Romo, R., A. Hernández, A. Zainos, C. D. Brody, and L. Lemus, "Sensing without Touching: Psychophysical Performance Based on Cortical Microstimulation," *Neuron*, Vol. 26, no. 1, pp. 273–278, 2000.

65. DevecioÄlu, Ä., and B. Güçlü, "A novel vibrotactile system for stimulating the glabrous skin of awake freely behaving rats during operant conditioning," *Journal of Neuroscience Methods*, Vol. 242, pp. 41–51, 2015.

66. DevecioÄlu, Ä., and B. Güçlü, "Psychophysical correspondence between vibrotactile intensity and intracortical microstimulation for tactile neuroprostheses in rats," *Journal of Neural Engineering*, Vol. 14, no. 1, p. 016010, 2017.

67. Ozturk, S., I. Devecioglu, M. Beygi, A. Atasoy, S. Mutlu, M. Ozkan, and B. Guclu, "Real-Time performance of a tactile neuroprosthesis on awake behaving rats," *IEEE Transactions on Neural Systems and Rehabilitation Engineering*, 2019.

68. Klaes, C., Y. Shi, S. Kellis, J. Minxha, B. Revechkis, and R. A. Andersen, "A cognitive neuroprosthetic that uses cortical stimulation for somatosensory feedback," *Journal of Neural Engineering*, Vol. 11, no. 5, p. 56024, 2014.

69. Strumwasser, F., "Long-Term Recording from Single Neurons in Brain of Unrestrained Mammals," *Science*, Vol. 127, pp. 469 LP – 470, feb 1958.

70. Kostarelos, K., M. Vincent, C. Hebert, and J. A. Garrido, "Graphene in the Design and Engineering of Next-Generation Neural Interfaces," 2017.

71. Novoselov, K. S., A. K. Geim, S. V. Morozov, D. Jiang, Y. Zhang, S. V. Dubonos, I. V. Grigorieva, and A. A. Firsov, "Electric field in atomically thin carbon films," *Science*, Vol. 306, no. 5696, pp. 666–669, 2004.

72. Kim, K. S., Y. Zhao, H. Jang, S. Y. Lee, J. M. Kim, K. S. Kim, J. H. Ahn, P. Kim, J. Y. Choi, and B. H. Hong, "Large-scale pattern growth of graphene films for stretchable transparent electrodes," *Nature*, Vol. 457, no. 7230, pp. 706–710, 2009.

73. Reina, A., X. Jia, J. Ho, D. Nezich, H. Son, V. Bulovic, M. S. Dresselhaus, and K. Jing, "Large area, few-layer graphene films on arbitrary substrates by chemical vapor deposition," *Nano Letters*, Vol. 9, no. 1, pp. 30–35, 2009.

74. Li, D., M. B. Müller, S. Gilje, R. B. Kaner, and G. G. Wallace, "Processable aqueous dispersions of graphene nanosheets," *Nature Nanotechnology*, Vol. 3, no. 2, pp. 101–105, 2008.

75. Schniepp, H. C., J. L. Li, M. J. McAllister, H. Sai, M. Herrera-Alonson, D. H. Adamson, R. K. Prud'homme, R. Car, D. A. Seville, and I. A. Aksay, "Functionalized single graphene sheets derived from splitting graphite oxide," *Journal of Physical Chemistry B*, Vol. 110, no. 17, pp. 8535–8539, 2006.

76. Stankovich, S., D. A. Dikin, R. D. Piner, K. A. Kohlhaas, A. Kleinhammes, Y. Jia, Y. Wu, S. B. T. Nguyen, and R. S. Ruoff, "Synthesis of graphene-based nanosheets via chemical reduction of exfoliated graphite oxide," *Carbon*, Vol. 45, no. 7, pp. 1558–1565, 2007.

77. Bonaccorso, F., A. Lombardo, T. Hasan, Z. Sun, L. Colombo, and A. C. Ferrari, "Production and processing of graphene and 2d crystals," *Materials Today*, Vol. 15, no. 12, pp. 564–589, 2012.

78. Wang, L., I. Meric, P. Y. Huang, Q. Gao, Y. Gao, H. Tran, T. Taniguchi, K. Watanabe, L. M. Campos, and D. A. Muller, "One-dimensional electrical contact to a two-dimensional material," *Science*, Vol. 342, no. 6158, pp. 614–617, 2013.

79. Hébert, C., E. MasvidalâCodina, A. SuarezâPerez, A. B. Calia, G. Piret, R. Garciaâ-Cortadella, X. Illa, E. Del Corro Garcia, J. M. De la Cruz Sanchez, and D. V. Casals, "Flexible graphene solutionâgated fieldâeffect transistors: efficient transducers for microâelectrocorticography," *Advanced Functional Materials*, Vol. 28, no. 12, p. 1703976, 2018.

80. Novoselov, K. S., V. I. Fal'ko, L. Colombo, P. R. Gellert, M. G. Schwab, and K. Kim, "A roadmap for graphene," *Nature*, Vol. 490, p. 192, oct 2012.

81. Paton, K. R., E. Varrla, C. Backes, R. J. Smith, U. Khan, A. O'Neill, C. Boland, M. Lotya, O. M. Istrate, P. King, T. Higgins, S. Barwich, P. May, P. Puczkarski, I. Ahmed, M. Moebius, H. Pettersson, E. Long, J. Coelho, S. E. O'Brien, E. K. McGuire, B. M. Sanchez, G. S. Duesberg, N. McEvoy, T. J. Pennycook, C. Downing, A. Crossley, V. Nicolosi, and J. N. Coleman, "Scalable production of large quantities of defect-free few-layer graphene by shear exfoliation in liquids," *Nature Materials*, Vol. 13, p. 624, apr 2014.

82. Bae, S., H. Kim, Y. Lee, X. Xu, J. S. Park, Y. Zheng, J. Balakrishnan, T. Lei, H. Ri Kim, Y. I. Song, Y. J. Kim, K. S. Kim, B. Özyilmaz, J. H. Ahn, B. H. Hong, and S. Iijima, "Roll-to-roll production of 30-inch graphene films for transparent electrodes," *Nature Nanotechnology*, Vol. 5, no. 8, pp. 574–578, 2010.

83. Lin, Y. M., A. Valdes-Garcia, S. J. Han, D. B. Farmer, I. Meric, Y. Sun, Y. Wu, C. Dimitrakopoulos, A. Grill, P. Avouris, and K. A. Jenkins, "Wafer-scale graphene integrated circuit," *Science*, Vol. 332, no. 6035, pp. 1294–1297, 2011.

84. Lee, C., X. Wei, J. W. Kysar, and J. Hone, "Measurement of the elastic properties and intrinsic strength of monolayer graphene," *Science*, Vol. 321, no. 5887, pp. 385–388, 2008.

85. Childres, I., L. A. Jauregui, W. Park, H. Caoa, and Y. P. Chena, "Raman spectroscopy of graphene and related materials," in *New Developments in Photon and Materials Research*, 2013.

86. Partoens, B., and F. M. Peeters, "From graphene to graphite: Electronic structure around the K point," *Physical Review B - Condensed Matter and Materials Physics*, Vol. 74, no. 7, 2006.

87. Geim, A. K., and K. S. Novoselov, "The rise of graphene," *Nature Materials*, Vol. 6, no. 3, pp. 183–191, 2007.

88. Geim, A. K., and A. H. MacDonald, "Graphene: Exploring carbon flatland," *Physics Today*, Vol. 60, no. 8, pp. 35–41, 2007.

89. Das Sarma, S., S. Adam, E. H. Hwang, and E. Rossi, "Electronic transport in two-dimensional graphene," *Reviews of Modern Physics*, Vol. 83, no. 2, pp. 407–470, 2011.

90. Tang, L., Y. Wang, Y. Li, H. Feng, J. Lu, and J. Li, "Preparation, structure, and electrochemical properties of reduced graphene sheet films," *Advanced Functional Materials*, Vol. 19, no. 17, pp. 2782–2789, 2009.

91. Lee, W. C., C. H. Y. X. Lim, H. Shi, L. A. L. Tang, Y. Wang, C. T. Lim, and K. P. Loh, "Origin of Enhanced Stem Cell Growth and Differentiation on Graphene and Graphene Oxide," *ACS Nano*, Vol. 5, no. 9, pp. 7334–7341, 2011.

92. Nayak, T. R., H. Andersen, V. S. Makam, C. Khaw, S. Bae, X. Xu, P.-L. R. Ee, J.-H. Ahn, B. H. Hong, G. Pastorin, and B. Özyilmaz, "Graphene for Controlled and Accelerated Osteogenic Differentiation of Human Mesenchymal Stem Cells," *ACS Nano*, Vol. 5, pp. 4670–4678, jun 2011.

93. Kim, T., Y. H. Kahng, T. Lee, K. Lee, and D. H. Kim, "Graphene films show stable cell attachment and biocompatibility with electrogenic primary cardiac cells," *Molecules and Cells*, Vol. 36, pp. 577–582, dec 2013.

94. Park, S. Y., J. Park, S. H. Sim, M. G. Sung, K. S. Kim, B. H. Hong, and S. Hong, "Enhanced Differentiation of Human Neural Stem Cells into Neurons on Graphene," *Advanced Materials*, Vol. 23, pp. H263–H267, sep 2011.

95. Kuzum, D., H. Takano, E. Shim, J. C. Reed, H. Juul, A. G. Richardson, J. De Vries, H. Bink, M. A. Dichter, T. H. Lucas, D. A. Coulter, E. Cubukcu, and B. Litt, "Transparent and flexible low noise graphene electrodes for simultaneous electrophysiology and neuroimaging," *Nature Communications*, Vol. 5, 2014.

96. Liu, Z., J. T. Robinson, X. Sun, and H. Dai, "PEGylated Nanographene Oxide for Delivery of Water-Insoluble Cancer Drugs," *Journal of the American Chemical Society*, Vol. 130, pp. 10876–10877, aug 2008.

97. Sun, X., Z. Liu, K. Welsher, J. T. Robinson, A. Goodwin, S. Zaric, and H. Dai, "Nano-Graphene Oxide for Cellular Imaging and Drug Delivery," *Nano Research*, Vol. 1, no. 3, pp. 203–212, 2008.

98. Markovic, Z. M., L. M. Harhaji-Trajkovic, B. M. Todorovic-Markovic, D. P. Kepić, K. M. Arsikin, S. P. Jovanović, A. C. Pantovic, M. D. Dramićanin, and V. S. Trajkovic, "In vitro comparison of the photothermal anticancer activity of graphene nanoparticles and carbon nanotubes," *Biomaterials*, Vol. 32, no. 4, pp. 1121–1129, 2011.

99. Fan, H., L. Wang, K. Zhao, N. Li, Z. Shi, Z. Ge, and Z. Jin, "Fabrication, Mechanical Properties, and Biocompatibility of Graphene-Reinforced Chitosan Composites," *Biomacromolecules*, Vol. 11, pp. 2345–2351, sep 2010.

100. Mohanty, N., and V. Berry, "Graphene-Based Single-Bacterium Resolution Biodevice and DNA Transistor: Interfacing Graphene Derivatives with Nanoscale and Microscale Biocomponents," *Nano Letters*, Vol. 8, pp. 4469–4476, dec 2008.

101. Zhou, M., Y. Zhai, and S. Dong, "Electrochemical Sensing and Biosensing Platform Based on Chemically Reduced Graphene Oxide," *Analytical Chemistry*, Vol. 81, pp. 5603–5613, jul 2009.

102. Lu, Y., H. Lyu, A. G. Richardson, T. H. Lucas, and D. Kuzum, "Flexible Neural Electrode Array Based-on Porous Graphene for Cortical Microstimulation and Sensing," *Scientific Reports*, Vol. 6, 2016.

103. Cohen-Karni, T., Q. Qing, Q. Li, Y. Fang, and C. M. Lieber, "Graphene and Nanowire Transistors for Cellular Interfaces and Electrical Recording," *Nano Letters*, Vol. 10, pp. 1098–1102, mar 2010.

104. Hess, L. H., M. Jansen, V. Maybeck, M. V. Hauf, M. Seifert, M. Stutzmann, I. D. Sharp, A. Offenhäusser, and J. A. Garrido, "Graphene transistor arrays for recording action potentials from electrogenic cells," *Advanced Materials*, Vol. 23, no. 43, pp. 5045–5049, 2011.

105. Blaschke, B. M., M. Lottner, S. Drieschner, A. B. Calia, K. Stoiber, L. Rousseau, G. Lissourges, and J. A. Garrido, "Flexible graphene transistors for recording cell action potentials," *2D Materials*, Vol. 3, no. 2, 2016.

106. Blaschke, B. M., N. Tort-Colet, A. Guimerà-Brunet, J. Weinert, L. Rousseau, A. Heimann, S. Drieschner, O. Kempski, R. Villa, M. V. Sanchez-Vives, and J. A. Garrido, "Mapping brain activity with flexible graphene micro-transistors," *2D Materials*, Vol. 4, no. 2, 2017.

107. Park, D. W., J. P. Ness, S. K. Brodnick, C. Esquibel, J. Novello, F. Atry, D. H. Baek, H. Kim, J. Bong, K. I. Swanson, A. J. Suminski, K. J. Otto, R. Pashaie, J. C. Williams, and Z. Ma, "Electrical Neural Stimulation and Simultaneous in Vivo Monitoring with Transparent Graphene Electrode Arrays Implanted in GCaMP6f Mice," 2018.

108. Masvidal-Codina, E., X. Illa, M. Dasilva, A. B. Calia, T. Dragojević, E. E. Vidal-Rosas, E. Prats-Alfonso, J. Martínez-Aguilar, J. M. De la Cruz, R. Garcia-Cortadella, P. Godignon, G. Rius, A. Camassa, E. Del Corro, J. Bousquet, C. Hébert, T. Durduran, R. Villa, M. V. Sanchez-Vives, J. A. Garrido, and A. Guimerà-Brunet, "High-resolution mapping of infraslow cortical brain activity enabled by graphene microtransistors," *Nature Materials*, Vol. 18, no. 3, pp. 280–288, 2019.

109. Cohen, J. C., J. C. Makous, and S. J. Bolanowski, "Under which conditions do the skin and probe decouple during sinusoidal vibrations?," *Experimental Brain Research*, Vol. 129, pp. 211–217, nov 1999.

110. Shannon, R. V., "A Model of Safe Levels for Electrical Stimulation," *IEEE Transactions on Biomedical Engineering*, Vol. 39, no. 4, pp. 424–426, 1992.

111. Cogan, S. F., K. A. Ludwig, C. G. Welle, and P. Takmakov, "Tissue damage thresholds during therapeutic electrical stimulation," *Journal of Neural Engineering*, Vol. 13, no. 2, p. 21001, 2016.

112. Mukamel, R., H. Gelbard, A. Arieli, U. Hasson, I. Fried, and R. Malach, "Coupling Between Neuronal Firing, Field Potentials, and fMRI in Human Auditory Cortex," *Science*, Vol. 309, pp. 951 LP – 954, aug 2005.

113. Ryun, S., J. S. Kim, H. Lee, and C. K. Chung, "Tactile frequency-specific high-gamma activities in human primary and secondary somatosensory cortices," *Scientific Reports*, Vol. 7, no. 1, p. 15442, 2017.

114. DevecioÄlu, Ä., and B. Güçlü, "Asymmetric response properties of rapidly adapting mechanoreceptive fibers in the rat glabrous skin," *Somatosensory & Motor Research*, Vol. 30, pp. 16–29, mar 2013.

115. Pinto, D. J., J. C. Brumberg, and D. J. Simons, "Circuit Dynamics and Coding Strategies in Rodent Somatosensory Cortex," *Journal of Neurophysiology*, Vol. 83, pp. 1158–1166, mar 2000.

116. Shoykhet, M., D. Doherty, and D. J. Simons, "Coding of deflection velocity and amplitude by whisker primary afferent neurons: Implications for higher level processing," *Somatosensory and Motor Research*, Vol. 17, no. 2, pp. 171–180, 2000.

117. Herreras, O., "Local Field Potentials: Myths and Misunderstandings," *Frontiers in Neural Circuits*, Vol. 10, p. 101, dec 2016.

118. Arabzadeh, E., R. S. Petersen, and M. E. Diamond, "Encoding of Whisker Vibration by Rat Barrel Cortex Neurons: Implications for Texture Discrimination," *The Journal of Neuroscience*, Vol. 23, pp. 9146 LP – 9154, oct 2003.

119. Ahissar, E., S. Haidarliu, and M. Zacksenhouse, "Decoding temporally encoded sensory input by cortical oscillations and thalamic phase comparators," *Proceedings of the National Academy of Sciences*, Vol. 94, pp. 11633 LP – 11638, oct 1997.

120. Whitsel, B. L., E. F. Kelly, M. Xu, M. Tommerdahl, and M. Quibrera, "Frequency-dependent response of SI RA-class neurons to vibrotactile stimulation of the receptive field," *Somatosensory and Motor Research*, Vol. 18, pp. 263–285, jan 2001.

121. Rose, J. E., J. F. Brugge, D. J. Anderson, and J. E. Hind, "Phase-locked response to low-frequency tones in single auditory nerve fibers of the squirrel monkey.," *Journal of Neurophysiology*, Vol. 30, no. 4, pp. 769–793, 1967.

122. Lavine, R. A., "Phase-locking in response of single neurons in cochlear nucler complex of the cat to low-frequency tonal stimuli.," *Journal of Neurophysiology*, Vol. 34, pp. 467–483, may 1971.

123. Johnson, L. A., J. D. Wander, D. Sarma, D. K. Su, E. E. Fetz, and J. G. Ojemann, "Direct electrical stimulation of the somatosensory cortex in humans using electrocorticography electrodes: a qualitative and quantitative report," *Journal of Neural Engineering*, Vol. 10, no. 3, p. 36021, 2013.

124. Cronin, J. A., J. Wu, K. L. Collins, D. Sarma, R. P. N. Rao, J. G. Ojemann, and J. D. Olson, "Task-Specific Somatosensory Feedback via Cortical Stimulation in Humans," *IEEE Transactions on Haptics*, Vol. 9, no. 4, pp. 515–522, 2016.

125. Hiremath, S. V., E. C. Tyler-Kabara, J. J. Wheeler, D. W. Moran, R. A. Gaunt, J. L. Collinger, S. T. Foldes, D. J. Weber, W. Chen, M. L. Boninger, and W. Wang, "Human perception of electrical stimulation on the surface of somatosensory cortex," *PloS One*, Vol. 12, pp. e0176020–e0176020, may 2017.

126. Kirin, S. C., T. Yanagisawa, S. Oshino, K. Edakawa, M. Tanaka, H. Kishima, and Y. Nishimura, "Somatosensation Evoked by Cortical Surface Stimulation of the Human Primary Somatosensory Cortex ," 2019.

127. Barrese, J. C., N. Rao, K. Paroo, C. Triebwasser, C. Vargas-Irwin, L. Franquemont, and J. P. Donoghue, "Failure mode analysis of silicon-based intracortical microelectrode arrays in non-human primates," *Journal of Neural Engineering*, Vol. 10, no. 6, p. 66014, 2013.

128. Barrese, J. C., J. Aceros, and J. P. Donoghue, "Scanning electron microscopy of chronically implanted intracortical microelectrode arrays in non-human primates," *Journal of Neural Engineering*, Vol. 13, no. 2, p. 26003, 2016.

129. Campbell, A., and C. Wu, "Chronically Implanted Intracranial Electrodes: Tissue Reaction and Electrical Changes," *Micromachines*, Vol. 9, p. 430, aug 2018.

130. de la Oliva, N., X. Navarro, and J. del Valle, "Time course study of long-term biocompatibility and foreign body reaction to intraneural polyimide-based implants," *Journal of Biomedical Materials Research Part A*, Vol. 106, pp. 746–757, mar 2018.

131. Churchland, M. M., J. P. Cunningham, M. T. Kaufman, J. D. Foster, P. Nuyujukian, S. I. Ryu, and K. V. Shenoy, "Neural population dynamics during reaching," *Nature*, Vol. 487, no. 7405, pp. 51–56, 2012.